



REU PROGRAM IN INTERDISCIPLINARY MATERIALS RESEARCH

Research Reports by Students Supported by
the REU Site: Interdisciplinary Materials
Research for Undergraduates
(NSF REU Site Program, DMR-1757420)

This REU Program for Interdisciplinary Materials Research is co-organized and co-supported by the REU Site for Interdisciplinary Materials Science (NSF REU Site Program, DMR-1757420) and the Cornell Center for Materials Research (NSF MRSEC program, DMR-1719875). This document contains the reports by all students that were funded by the REU Site. The photo shows the cohort of the whole REU program.

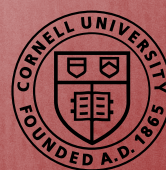


TABLE OF CONTENTS

Student

- 02 Natalie Cummings
- 08 Rebecca Davis
- 15 Jamie Holber
- 21 Saman Khorasi
- 27 Joshua Reyes Morales
- 29 Malia Okamura
- 37 Marcos R. Rodriguez
- 39 Mathias Rodriguez
- 59 Whitney Tso
- 66 Deidra Ward

Faculty Advisor

- Prof. Gennady Shvets
- Prof. Katja Nowack
- Prof. Gregory Fuchs
- Prof. Tobias Hanrath
- Prof. Héctor Abruña
- Prof. Andrej Singer
- Prof. Lawrence Bonassar
- Prof. Christopher Alabi
- Prof. Richard Robinson
- Prof. Julie Goddard

Novel Transfer Technique for Metasurfaces to the Tip of an Optical Fiber

Natalie Cummings¹, Gennady Shvets², Steven He Huang², and Shourya Dutta Gupta³

¹Department of Materials Science and Engineering, The Pennsylvania State University, State College, PA 16802

²Department of Applied and Engineering Physics, Cornell University, Ithaca, NY 14850

³Department of Materials Science and Metallurgical Engineering,
Indian Institute of Technology Hyderabad, Telangana 502285, India

We use a sacrificial copper layer to separate gold and PMMA from its substrate. Then, using a new take on transfer printing, we transfer the surface to PDMS, from which the surface can be applied to the tip of the optical fiber. The process eliminates the need for specialized equipment and excessive processing time while producing a comparable end result. Most of the work was performed with a bulk gold film, but some preliminary tests were performed with a metasurface.

I. INTRODUCTION

Metasurfaces, which are comprised of metal features designed to manipulate the movement and behavior of light, hold the key to the next generation of biosensors. These surfaces can be tuned to very spectrally narrow wavelengths of light [1]. This means that these surfaces can be used to identify the resonance peaks of proteins or other molecules, even in trace amounts. Although other similar technologies exist, they are incompatible with the current gold standard biosensors. Another potential advantage is the possibility for remote sensing. With the aid of the optical fiber, substances can be analyzed from a reasonable distance. By combining metasurfaces with optical fibers, we can create a remote sensing platform that would be compatible with existing biomedical devices.

The problem with this grand idea is the adhesion of the metasurface to the tip of the optical fiber. There have been a wide variety of proposed solutions, but each has their own drawbacks. FIB can be used to machine the pattern directly onto the fiber, but its small size is a challenge, and the surface can become inadvertently doped with gallium ions [2]. These inconsistencies can interfere with the carefully tailored plasmonic effects of the metasurface. In addition, this method is neither time- nor cost-effective. Other proposed solutions are the decal transfer, [3] nanoskiving, [4] and "transfer printing" [5] techniques. These improve upon direct machining of the optical fiber by producing the metal features on a sacrificial substrate, and then transferring the metasurface onto the fibers tip.

The solution we seek to provide is one that combines aspects of "decal transfer", "nanoskiving", and "transfer printing", and which can be completed quickly and efficiently.

Nanoskiving requires highly specialized equipment. The desired metasurface is created in epoxy, coated in the desired metal, encased in more epoxy, and then sliced into thin sheets using an ultramicrotome. After all those steps, the thickness of slices often varies, and some slices become unusable. Especially due to the low availability of ultramicrotomes, this process can become exceedingly

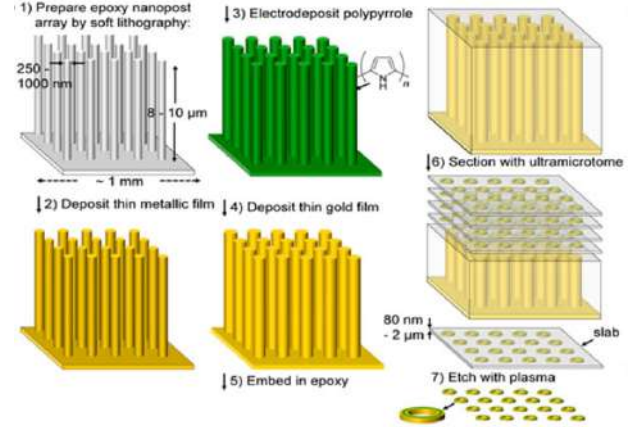


FIG. 1. Diagram showing the nanoskiving process.[4] The ultramicrotome, not pictured, is a highly specialized piece of equipment which is still subject to frequent error.

difficult. Despite its problems, its idea of a film holding together the metasurface was one we wanted to incorporate into our process.

The current decal transfer process is complicated and lengthy. A specialized thiol-ene film must be produced and cured, and then many steps lead to the final transfer of the metasurface to the tip of the fiber. Some of these steps require specialized equipment, such as a stereoscope. The film itself must be produced in-lab from its constituent chemicals, leaving a lot of room for human error. In addition, many parts of the process involve separating one layer from another, and require lengthy waiting times as those sections separate. Even so, the idea of a material which would be sticky enough to pick up the metasurface, but not so sticky to interfere with the final transfer was a great one.

Transfer printing uses some flexible substrate to aid in the transfer of features. There are three kinds of transfer printing; "additive transfer", "subtractive transfer", and "deterministic assembly". [5] Classic PDMS stamps fall under the realms of additive and subtractive transfers. A medium which can selectively pick up certain features is the goal of deterministic assembly. These techniques can be relatively quick and easy, and so we seek to modify

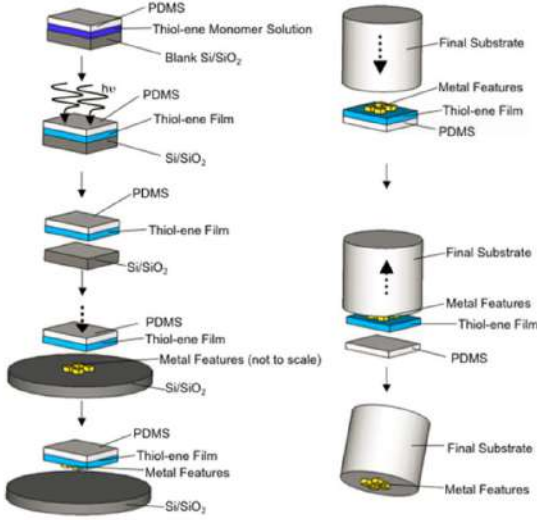


FIG. 2. Diagram showing the Thiol-Ene Decal Transfer process.[3] In addition to the need to synthesize the thiol-ene film, this process has numerous steps and requires a substantial amount of time.

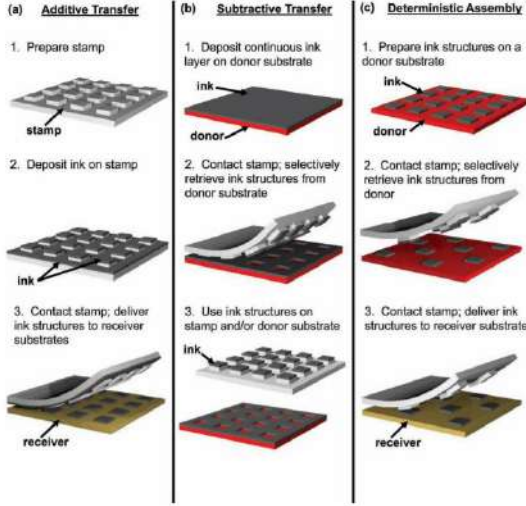


FIG. 3. Diagram showing the three different types of transfer printing.[5] There are strong similarities between these techniques, but each performs the transfer in a slightly different manner. The method most similar to our new approach is Deterministic Assembly. However, our PDMS "stamp" cannot choose features selectively, but rather must pick up all features.

one of these methods to simplify it even further.

Our new process seeks to reduce the difficulty and length of these processes, as well as maintaining or improving their results. By using common, easily available chemicals and tools, we seek to create a practical method for the transfer of metasurfaces to the tip of an optical fiber, which requires neither unreasonable equipment nor

unreasonable amounts of time.

A biological sensor which can identify and observe molecules is a big step forward, but it will likely never see the light of day if its manufacturing cannot be simplified into a commercially feasible process. The advances we have made pave the way for further simplification of our process.

II. METHODS

In order to optimize our process, we began the process with multimode, glass-clad silica fiber (Thor Labs FG200LEA). This fiber has a core of $\sim 200 \mu\text{m}$, a cladding of $\sim 220 \mu\text{m}$, and an acrylate coating of $\sim 320 \mu\text{m}$.

We adapted the thiol-ene "decal transfer" procedure detailed in "A Technique to Transfer Metallic Nanoscale Patterns to Small and Non-Planar Surfaces". Briefly, this procedure uses a chemically reproducible thiol-ene film to adhere to the metal features. Later, this film is removed via oxygen plasma. This leaves the surface on the tip of the optical fiber. The synthesis of the thiol-ene film adds a significant amount of time and steps to an already complicated process, though.

To shorten the process, we sought to eliminate the need for the thiol-ene film altogether, instead subbing in a different, more ubiquitous polymer (495 PMMA A4) in a more efficient manner. Our process begins with the fabrication of the surface. We evaporate a thin (200 nm) layer of copper, then a 10 nm chromium adhesion layer onto a CaF₂ substrate. Next, a gold layer (70 nm) is evaporated onto the chromium layer. Beneath the copper layer is a thicker calcium fluoride substrate for support. After the surface is finished, it is spin-coated with one layer of PMMA. This holds the surface together in later steps, but is not overly attracted to the gold (both important characteristics). To cure the PMMA, we bake it at 90 C for 3 minutes, then at 170 C for 19 minutes, and at 90 C again for another 7 minutes.

Next, we scratch the PMMA film in two places on the substrate, so that the etchant will be able to seep under the PMMA and remove all of the sacrificial copper layer. We place small, "L" shaped scratches on opposite corners of the sample. With the scratches complete, we place the sample in copper etchant (CE-200), which separates the surface and PMMA from the copper and silicon. This process takes 2.5 hours, after which the copper has been completely etched away. The PMMA and surface will not delaminate after this step, though. The sample should be gently rinsed and dried before the next step. If the scratches are placed poorly, or the rinsing and drying is too intense, the film can wrinkle or fold, in some cases destroying the surface.

After the etch is complete, we clean a piece of cured Sylgard 184 Silicone Elastomer PDMS to prepare it for transfer. We apply pressure to the PDMS, and when we remove it, it takes the gold surface with it. Although pressure is important to ensure that the surface transfers

to the PDMS, excessive pressure will crack the calcium fluoride substrate, so caution must be taken. Then, we simply turn over the PDMS, readying it for contact with the fiber.



FIG. 4. An image of the PDMS after the surface has been transferred. Small, circular defects can be observed around the surface. These are a result of the transfer to the fiber. The "L" shaped defect in the bottom left hand corner is from the scratch in the PMMA. The other scratch was in the top right hand corner, and part of it can still be observed in the sample.

In preparation for the transfer, fiber samples are cleaved and stripped, with a maximum angle of 2.0 degrees.

To transfer the surface, we press the tip of the fiber onto the PDMS at a 90 degree angle, allowing them to connect and applying gentle pressure for ten seconds. This orientation and pressure are essential to the connection of the fiber and the surface. Care must also be taken not to wiggle the fiber too much during the connection, as this tends to move some of the surface from the tip of the fiber to its sides. Also important to take into consideration is the potential of the fibers to break. If the pressure applied is too great or the application is done at an improper angle, the fiber tends to snap.

After the surface has been successfully transferred to the fiber, oxygen plasma removes the PMMA layer from the original fabrication. An Anatech oxygen plasma etcher was used for this process, at the descum setting. We used a power of 300 W for 40 minutes, with 220 oxygen and 20 nitrogen. After removing the PMMA film, we noticed that the fibers seemed to have retained their previous level of coverage.

III. RESULTS AND DISCUSSION

Our process took several iterations to reach this level of success. We began with samples of gold evaporated onto

a chromium layer on a glass substrate. A slow etchant rate and a tendency for the PMMA to remain adhered to the substrate ruled out this method. We moved next to similar samples, but with copper on the glass substrate, and an adhesion layer of chromium between the copper and gold.

After this setup provided quicker etching times but still had problems with delamination, we moved to a new solution. Using Kapton tape, we were able to remove clear sections of the gold and PMMA. While effective for removing the features, this method did not facilitate the transfer, even when defects such as small holes were added to aid in the process. The tape was simply too sticky, and the gold wasn't attracted enough to the tip of the fiber to retain its adhesion during periods of mechanical stress. In addition, the Kapton proves very difficult to separate from the surface, even before contact with the fiber. Acetone will remove some of the adhesive, but the tape still fails to separate from the gold and PMMA.

Our PDMS solution managed to solve this problem because it serves as a less sticky transfer medium. It adheres to the gold and PMMA well enough to remove it from the substrate, but is not so attracted that the fiber cannot remove the surface. We faced some issues initially when determining the ideal manner in which to transfer from the PDMS to the tip of the fiber. Many different methods of application result in very patchy covering of the fiber's tip, especially around the edges or excluding the middle. Clearly, these types of results don't ensure full coverage of the fiber's core, and as such would not be usable as sensing devices.

The ability to use PDMS in this capacity is important mainly for two reasons. Firstly, it works consistently and easily; after a bit of practice the process of transferring the surface to the fiber's tip becomes simple. Secondly, PDMS is a readily available, easy to use polymer. We used a very standard recipe, which is simple to produce. This is vast improvement from the thiol-ene film which not only obscures multiple separate chemicals, but also for the user to mix them in the right proportions to successfully synthesize the film.

In order to view the tips of the fibers after the transfers and removal of the PMMA film, we utilized the Thermo Scientific Nicolet Continuum Infrared Microscope, with the 10x objective lens. We needed to ensure that the fiber was angled directly toward the lens, so we devised a technique to keep the fiber upright and in place on the microscope slide. First, another piece of PDMS is needed. The shape is not important, but it must not be so small that it can fall through the hole in the center of the microscope's slide. Next, we used a small biopsy punch to create a small hole through the piece. The fiber (non-coated end first) can be threaded through the PDMS, and both can be positioned on top of the slide. To ensure a lack of movement, we secured the PDMS in place with double sided tape.

We observed that this method resulted in the nearly complete coverage of the tip of the optical fiber. In ad-



FIG. 5. An image of the setup for microscopy. The PDMS supports the fiber, keeping it at a favorable angle for imaging with the microscope. The double-sided tape ensures that, as the stage moves, the fiber and PDMS do not move with it.

dition, even after the removal of the PMMA film with the oxygen plasma, the features remained solidly on the fiber's tip. Although the vast bulk of our results relied

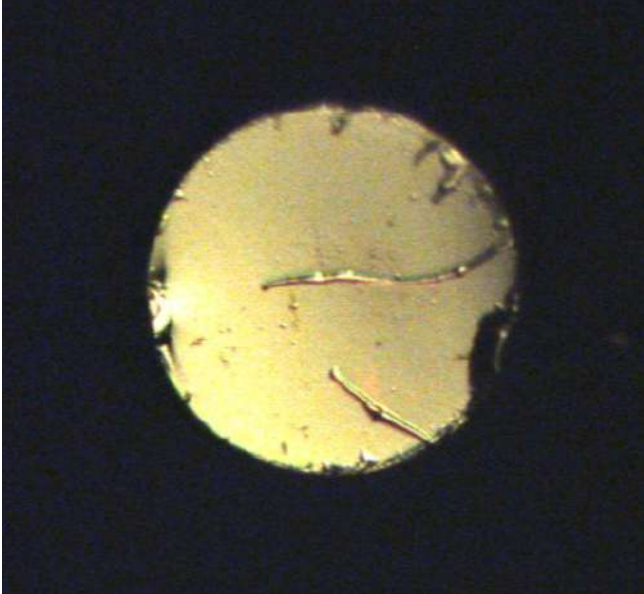


FIG. 6. An image of the fiber's tip after oxygen plasma. It can be seen that nearly the entire tip of the fiber is covered in gold.

on the transfer of bulk gold surfaces, at the end of the research session we were able to transfer one metasurface to PDMS, with good results. Transferring the metasurface to the fiber proved more difficult, but was possible, however a lack of time prevented the perfection of the technique. In the following image, the metasurface (although poorly aligned) can be seen on the fiber's tip.

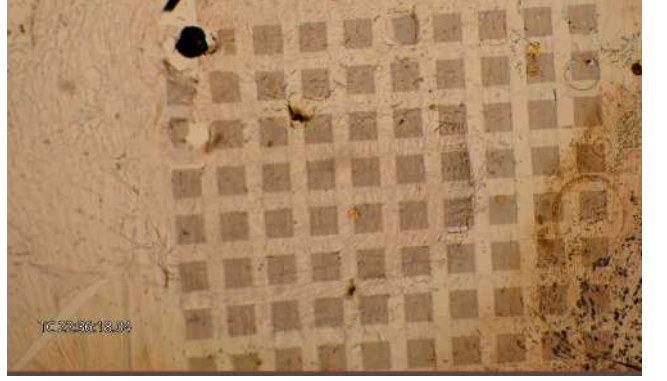


FIG. 7. An image of the PDMS after the transfer of the metasurface. Each square is a 50x50 array of gold nanofeatures. The chromium adhesion layer and the PMMA are still present. It was imaged through the PDMS using an inverted optical microscope.



FIG. 8. An image of the fiber tip after the transfer of the metasurface. The poorly aligned metasurface can be seen on the lower half of the fiber's tip. This may not be an exemplary transfer, but it points to the potential of the method.

IV. CONCLUSION

Our experiments have shown that our new copper-based process has the potential to be an effective transfer method. Time constraints meant that a final metasurface-to-fiber transfer process could not be perfected, but what we have learned can be extrapolated toward this conclusion.

We know that the copper etchant is much more efficient than the chromium etchant, etching away the sacrificial layer in around 2 to 2.5 hours. We also know that, although the PMMA layer does not delaminate as we had anticipated, we can use the PDMS to remove

unbesmirched sections of gold and polymer. If the fiber is connected at the correct angle and pressure, we notice that the rate of transfer is very high and expect that these results would carry through to a gold metasurface in place of a solid golden surface.

This same principle of utilizing PDMS doesn't need to change as the process iterates toward the final product; the final chalcogenide fiber will be of a similar size to the fiber we tested, and thus should behave in a similar way when picking up the metasurface.

This process can decrease the time and effort needed to transfer metasurfaces to the tips of optical fibers. The current available methods, thiol-ene film transfer and nanoskiving, have numerous steps requiring specialized equipment, but our method, after fabrication, is much simpler. With a spinner, a chemical hood, and some PDMS, our method can be executed. In addition, once this process has been established, any metasurface could be transferred. Whether we are using an array specialized for proteins or one tuned to an entirely different wavelength, they all ought to be able to be placed onto the tip of a fiber using our method.

Additionally, one transfer to PDMS can result in many transfers to fiber tips. Since the PDMS removes large sections of the surface and the tips only remove small pieces, this method is quite efficient. One round of fabrication can provide for numerous samples, while probably taking a similar amount of time to machining the surface directly onto the tip of one fiber. This principle, in general, speaks to the efficacy of our method. The techniques are not so revolutionary, the process does not take pages to explain. Instead, the simplicity improves the process, leading to better efficiency and an easier process.

A. Future Work

As this process continues to develop, there are multiple steps which can be taken to improve it. First and foremost is the perfection of the transfer technique. For our preliminary tests with metasurfaces, we used a micrometer stage, an inverted microscope, a fiber holder, and a lot of double-sided tape to create a makeshift device which would regulate the connection of the fiber and the metasurface. With more practice, we will learn exactly how the sample should be aligned, as well as the distance the fiber needs to press down in order to optimally connect with the metasurface.

Also important is the improvement of the adhesion of the gold metasurface (and the chromium adhesion layer) to the tip of the fiber. As of now we are unsure whether or not the fiber would survive a submersion in water. Some ideas to improve the adhesion include annealing the fiber or evaporating a thin layer of silicon onto the surface.

Next, the metasurface we transferred was scaled up, and we used a silica fiber. For its final application, a smaller metasurface and a chalcogenide fiber should be used. Although we don't anticipate significant deviation in results when making these changes, it is still important to consider how they may affect the process. A smaller metasurface means that the transfer process will need to be even more precise, and the chalcogenide fiber may behave differently when picking up the metasurface from the PDMS.

Once the process for the final metasurface and fiber has been streamlined, we will test the fiber for its intended usage: biological sensing. Whether or not the device can successfully identify spectral identities of proteins will determine whether or not further changes to the process need to be made.

Although we may not have reached the final stages of this project, we are confident that our work has laid a solid foundation for a more cost- and time-effective method for transferring metasurfaces to the tip of an optical fiber. With some more work along this vein, we are confident that this method has the potential to simplify the transfer process, opening the doors for minimally invasive yet precise biosensors and countless other applications.

V. ACKNOWLEDGEMENTS

The author would like to thank Gennady Shvets, Steven He Huang, and Shourya Dutta Gupta. Thank also to the CNF and its staff (especially Aaron Windsor and Jerry Drumheller). This work was performed in part at the Cornell NanoScale Facility, a member of the National Nanotechnology Coordinated Infrastructure (NNCI), which is supported by the National Science Foundation (Grant ECCS-1542081). Of course, a huge thank you to the CCMR REU program, especially Rebecca Broome and Nevjinder Singhota. The CCMR REU program is supported by the NSF MRSEC program (DMR-1719875) and the REU Site program (DMR-1063059).

-
- [1] Wu, Chihhui, Alexander B. Khanikaev, Ronen Adato, Nihal Arju, Ahmet Ali Yanik, Hatice Altug, and Gennady Shvets. "Fano-resonant Asymmetric Metamaterials for Ultrasensitive Spectroscopy and Identification Of molecular Monolayers." *Nature Materials* 11, no. 1, **69-75** (2011).
 - [2] Yu, Nanfang, and Federico Capasso. ["Optical Metasurfaces and Prospect of Their Applications Including Fiber Optics."] *Journal of Lightwave Technology* 33, no. 12, **2344-358** (2015).
 - [3] Smythe, Elizabeth J., Michael D. Dickey, George M. Whitesides, and Federico Capasso. ["A Technique to Transfer Metallic Nanoscale Patterns to Small and Non-

- Planar Surfaces.*"] ACS Nano 3, no. 1, **59-65** (2009).
- [4] Lipomi, Darren J., Ramses V. Martinez, Mikhail A. Kats, Sung H. Kang, Philseok Kim, Joanna Aizenberg, Federico Capasso, and George M. Whitesides. ["*Patterning the Tips of Optical Fibers with Metallic Nanostructures Using Nanoskiving.*"] Nano Letters 11, no. 2, **632-36** (2010).
- [5] Carlson, Andrew, Audrey M. Bowen, Yonggang Huang, Ralph G. Nuzzo, and John A. Rogers. ["*Transfer Printing Techniques for Materials Assembly and Micro/Nanodevice Fabrication.*"] Advanced Materials 24, no. 39 **5284-318** (2012).

Characterization of Scanning Superconducting Quantum Interference Devices (SQUIDs)

Rebecca Davis¹, Rachel Resnick², David Low², Professor Katja Nowack²

¹Department of Physics and Engineering, West Virginia Wesleyan College, Buckhannon, WV 26201

²LASSP, Cornell University, Ithaca, NY 14853

Abstract- Detecting small magnetic fields is crucial to various fields, including submarine detection, brain signal scanning, and fundamental science research. Superconducting Quantum Interference Devices (SQUIDs) are highly sensitive magnetic field detectors. However, to detect the lowest fields possible, it is desirable to reduce noise in the SQUID. Here we characterize the noise of SQUIDs specifically designed for scanning. We implement a procedure to tune the SQUIDs to have optimal noise performance. We further study the effect of a damping resistor added to a SQUID circuit and find that it impacts the hysteretic properties and resonances of the SQUIDs.

I. Introduction

SQUID designs have been described in many places in the literature [1]. SQUID magnetometers allow for the measurement of small magnetic fields. This makes them suitable for applications such as neuroscience, military defense, and fundamental science. SQUIDs have been used both to measure the magnetic field activity of the brain and to detect the magnetic field signals emitted by submarines. Fundamentally, these devices function by outputting a measurable voltage signal in response to an input magnetic flux. The resultant voltage signal allows for classification of material properties such as superconductivity; for example, the superconducting transition could be identified using this method.

The SQUIDs used in our lab have several components including a field coil, modulation (mod) coil, pickup loops, shunt resistors and Josephson junctions. An input current is sent through the mod coil. This

generates magnetic flux in the superconducting loop, thus changing the output voltage. The output voltage can then be displayed on current-voltage (IV) curves for analysis. Josephson junctions are the core of these devices. They are comprised of two superconducting layers with a thin insulating layer in between. Here, we use Niobium (Nb) as a superconductor with an insulating aluminum oxide layer. Junctions interrupt the superconducting loop to modulate the input signal in response to magnetic flux. Temperatures as low as $\sim 9\text{K}$ are needed for Nb to superconduct and we perform our measurements at $\sim 4\text{K}$. Superconductivity can be observed through voltage measurements of the SQUID. Figure 1 shows a diagram of our SQUIDs.

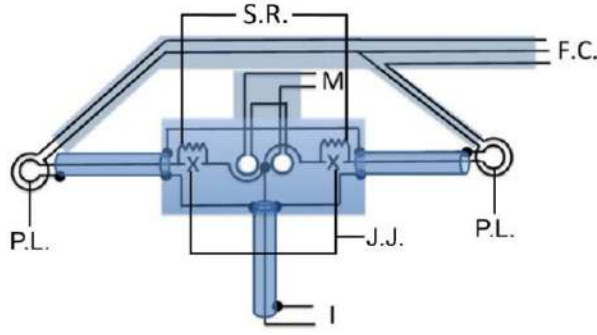


Figure 1. A schematic of our SQUIDs including the field coil (F.C.), modulation coil (M), Josephson Junctions (J.J.), shunt resistor (S.R.) and pickup loop (P.L). [4]

An important component are the resistors (R) that shunt the Josephson junction as visible in Figure 1 and Figure 2a. These determine whether or not the SQUID is hysteretic through the quantity defined by Eq. (1).

$$\beta_c = \frac{2\pi}{\phi_0} (I_c R^2 C) \quad (1)$$

I_c denotes the critical current

R^2 denotes Shunt Resistance

C denotes capacitance

ϕ_0 denotes the magnetic flux quantum

When $\beta_c < 1$, hysteresis will not occur. When $\beta_c \geq 1$, the SQUIDs begin to exhibit hysteretic properties [3]. For our application, hysteretic SQUIDs are not desirable because they switch randomly between two different states. From Eq. (1), it is apparent that higher shunt resistor values result in higher β_c values. Considering this, selection of the resistor values allow for control over the hysteretic properties of the SQUIDs.

Another less controlled component of the SQUID is parasitic capacitance, which is present due to our specific design as shown in Figure 1. The parasitic capacitance causes

resonances in the SQUID [2]. It has been theorized that adding a damping resistor (See Figure 2b), in addition to the shunt resistors, can alter these resonances [5] and through that, can improve the noise performance. We therefore tested SQUIDs with and without damping resistors, as seen in Figure 2a and Figure 2b.

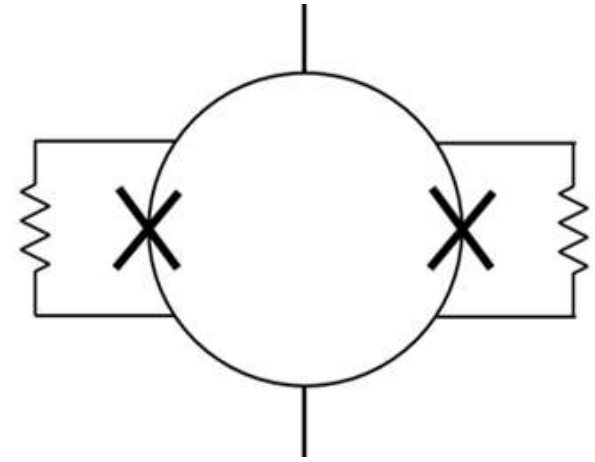


Figure 2a. SQUID with shunt resistors and without a damping resistor.

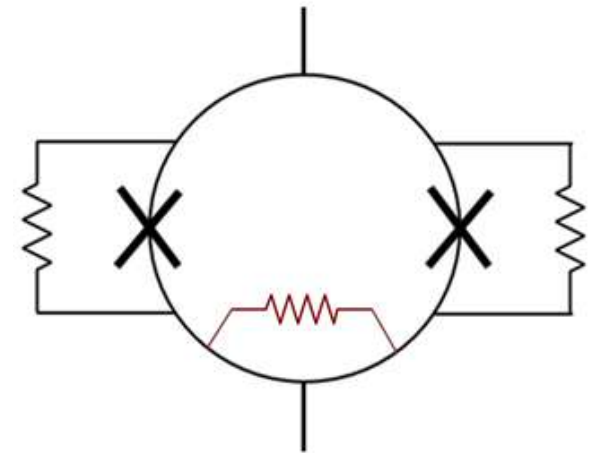


Figure 2b. SQUID with shunt resistors and a damping resistor

II. Methods

A. Process of IV Measurement

To take IV measurements, a current must run through the SQUID. Figure 3 shows the general setup for IV testing. The red dashed line signifies the helium Dewar in which our SQUIDs are placed during testing to cool to 4.2 K. Current is sent through the mod coil which then generates a magnetic field that threads magnetic flux into the SQUID, seen by the red arrow.

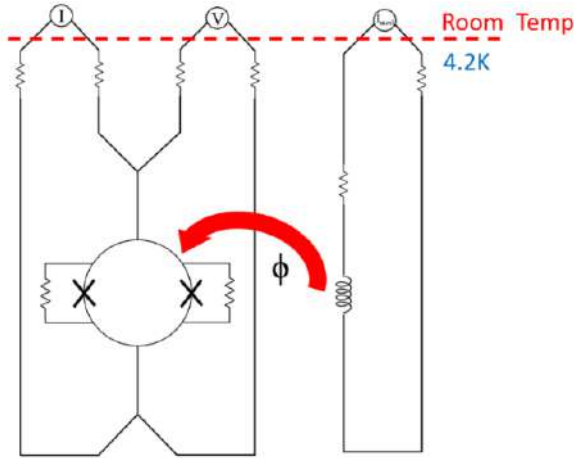


Figure 3. Diagram of 4 point IV system. Current is sent through the SQUID to generate a voltage. Current is sent through the mod coil which generates magnetic field. This magnetic field then threads into the superconducting loop of the SQUID to create magnetic flux.

Using Python, the lab can remotely control the current and read the resulting voltage across the SQUID to record IV characteristics of the SQUID. This IV process allows us to observe crucial characteristics of the SQUID, such as when it superconducts below the critical current and the hysteretic properties.

Hypres scanning SQUIDs with 8 ohm shunt resistors (R8 SQUIDs) were used to compare properties of the SQUID. These SQUIDs were expected to be hysteretic given their high resistor values. Multiple sets of damped and non-damped R8 SQUIDs were tested and we observed that the addition of a damping resistor decreased the hysteretic properties. Figure 4a shows the IV measurements for a SQUID that is not damped. The portions of the graph in which the orange and blue traces do not coincide clearly show the hysteretic characteristic of the SQUID. The blue line is measured with current increasing from low to high [UP] and the orange line is measured with current decreasing from high to low [DOWN]. Meanwhile, Figure 4b shows the IV measurements for a different SQUID containing a 4 ohm damping resistor in addition to the 8 ohm shunt resistors. This SQUID is not hysteretic.

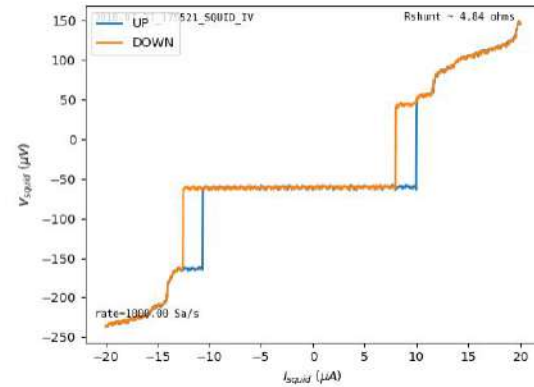


Figure 4a. IV measurement of non-damped SQUID with 8 ohm resistor.

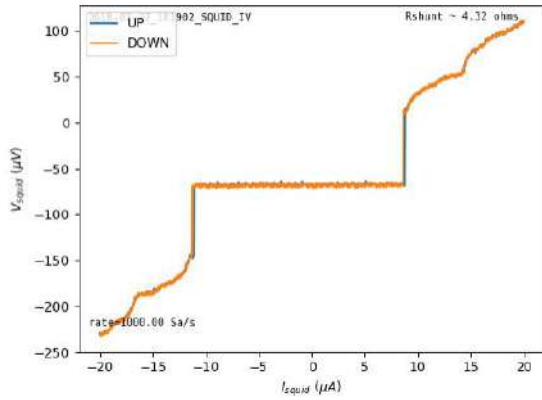
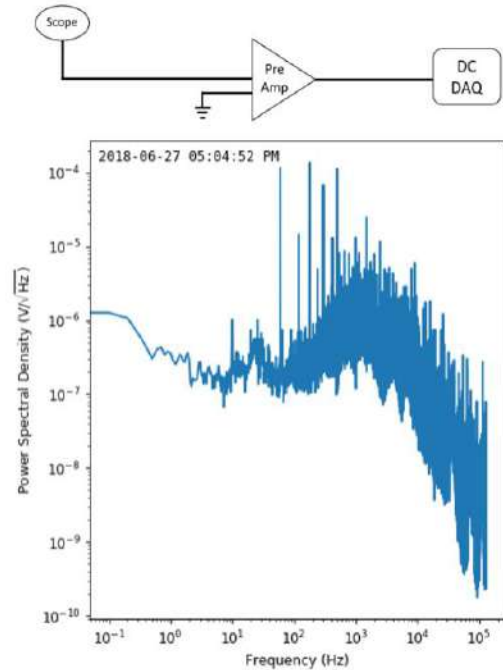
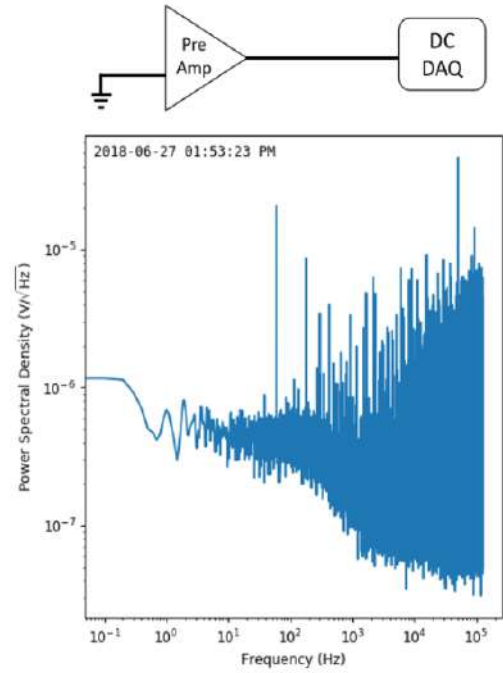


Figure 4b. IV measurement of damped SQUID with 8 ohm resistor and 4 ohm damping resistor.

B. Noise Background Measurements

For this project we needed to measure the noise of our SQUIDs. It is important to first check the background noise produced by our experimental setup including an oscilloscope, a data acquisition card (DAQ) and a preamplifier. To check the system, a series of tests were conducted to determine where the majority of the noise signal was originating. The diagrams for the tests are shown in Figure 5.



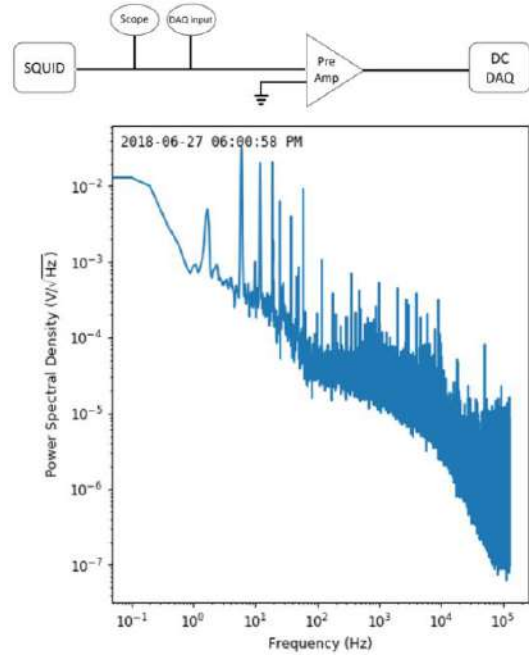
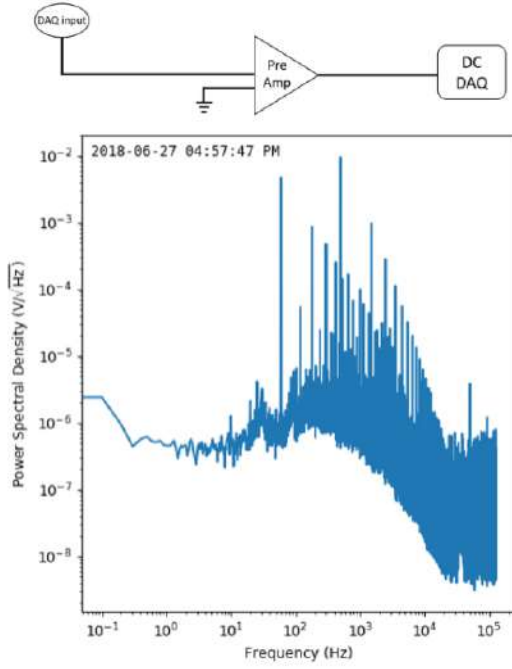
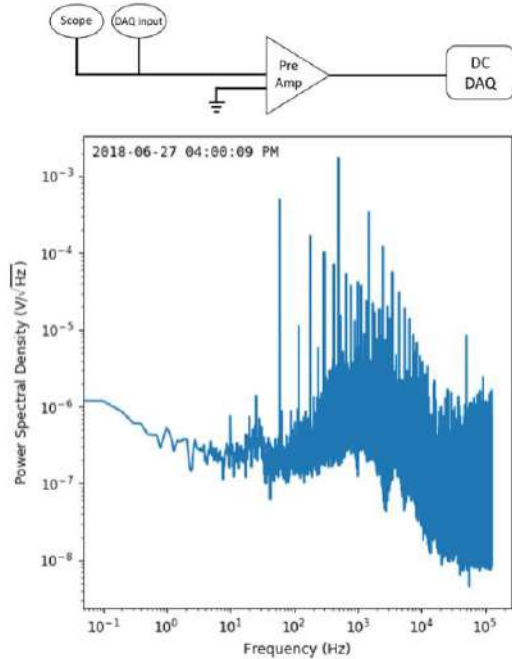


Figure 5. Diagrams of system location and corresponding noise measurements.

These diagrams allow us to follow the source of the noise. We can see that the noise remains at approximately $10^{-6} \frac{V}{\sqrt{Hz}}$ at the relevant frequencies for DC SQUIDS. Once the SQUID is connected, the noise increases by two orders of magnitude to $10^{-4} \frac{V}{\sqrt{Hz}}$. This confirms that the noise signal we are reading is due to the SQUID and not our external systems.

C. Noise Measurements

A SQUID array amplifier is used to amplify the intrinsic noise from the SQUID. The array is composed of a series of SQUIDS. Variations in the current passing through the SQUID are amplified by the array. The current through the SQUID changes due to intrinsic noise and due to changes in magnetic flux through the



SQUID. The amplifier is important for our experiments since our SQUIDs generally have noise on order of $\mu\phi_o$ which must be amplified in the cold in order to be detected at room temperature. Figure 6 shows the components of the experimental set-up. The entire system is an amplifier for the SQUID shown in Figure 6.

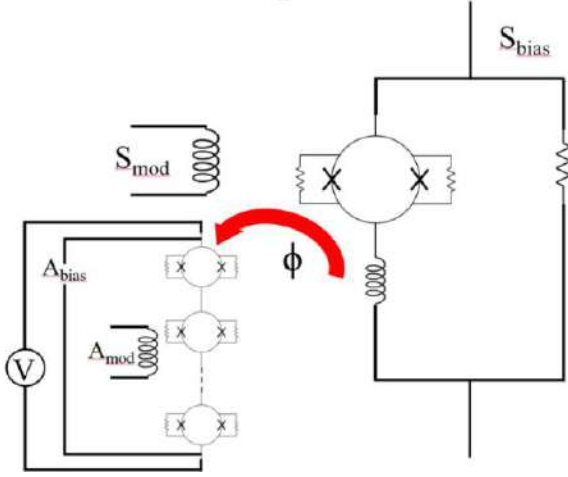


Figure 6. Diagram of array system. The array consists of 30 SQUIDs in series, inside of a magnetic shield. The array has a bias current as well as a voltage readout. The SQUID also is measured through a bias current and voltage readout. An array amplifies the noise signal of the SQUID.

We find that the noise performance of the SQUID depends on the available tuning parameters: the current applied to the circuit (S_{bias}) and a flux offset (S_{mod}). We have implemented a procedure in which we measure the noise as a function of these tuning parameters and then sort through all of the collected data to find the optimum tuning parameter for the SQUID. This gives us the lowest possible noise signal for a given SQUID. An example of an optimal noise spectrum is shown in Figure 7.

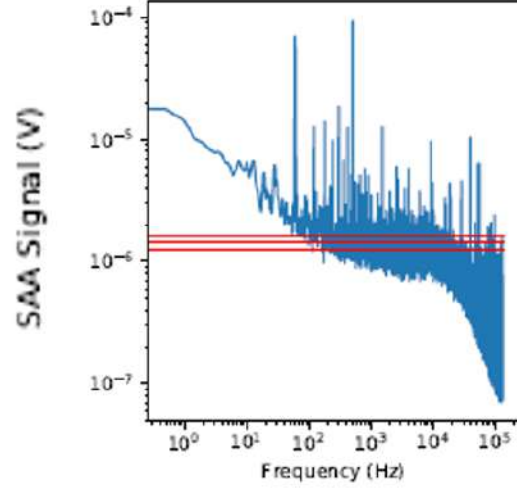


Figure 7. R8 non-damped SQUID noise measurement graph. The noise measured in this graph is $1.44 \frac{\mu\phi}{\sqrt{Hz}}$.

A noise generally around $1 \frac{\mu\phi}{\sqrt{Hz}}$ can be classified as a good SQUID that will be able to take accurate magnetic field measurements of a sample. It is crucial to carry out these tests to find the best signal-to-noise ratio of SQUIDs to use for scanning samples.

III. Results and Discussion

The focus of the study included IV and noise measurements of 8 ohm shunt resistor SQUIDs. We found that damped SQUIDs exhibit significantly less hysteresis and that resonances in the SQUID changed. We further have implemented a procedure to find the optimum noise performance for a given SQUID. Future work will investigate the impact of the damping resistors on the noise performance.

Moving forward, we plan to repeat testing to obtain more data points for both damped and non-damped SQUIDs. A greater number of data points will allow us to determine whether a correlation exists between resistance values and noise performance. If it is found that the addition of a damping resistor also decreases the noise present

within a SQUID, researchers would be encouraged to use damped SQUIDs to obtain more accurate measurements.

[6] SQUIDs & SQIFs. (2011, July 06). Retrieved from <https://www.hypres.com/squids-sqifs/>

V. Acknowledgements

I would like to thank the CCMR program at Cornell University for allowing me to conduct research this summer. I would also like to thank the NSF for funding me and allowing me to be immersed in academia.

More specifically, I would like to thank Dr. Katja Nowack, David Low, Rachel Resnick and the rest of the Nowack lab for their expertise throughout these ten weeks and for allowing me to use their equipment.

References

- [1] Clarke, J., & Braginski, A. I. (2004). *The SQUID handbook*(Vol. 1, Fundamentals and Technology of SQUIDs and SQUID Systems). Weinheim: Wiley-VCH.
- [2] Hilbert, C., & Clarke, J. (1985). Measurements of the dynamic input impedance of a dc SQUID. *Journal of Low Temperature Physics*, 61(3-4),37-262.
- [3] Huber, M. E., Koshnick, N. C., Bluhm, H., Archuleta, L. J., Azua, T., Björnsson, P. G., Moler, K. A. (2008). Gradiometric micro-SQUID susceptometer for scanning measurements of mesoscopic samples. *Review of Scientific Instruments*,79(5), 053704.
- [4] Kirtley, J. R., Paulius, L., Rosenberg, A. J., Palmstrom, J. C., Holland, C. M., Spanton, E. M., . . . Moler, K. A. (2016). Scanning SQUID susceptometers with sub-micron spatial resolution. *Review of Scientific Instruments*,87(9), 093702.
- [5] Knuutila, J., Ahonen, A., & Tesche, C. (1987). Effects on DC SQUID characteristics of damping of input coil resonances. *Journal of Low Temperature Physics*, 68(3-4), 269-284.

A differential current cutoff method for the electrochemical fabrication of gold tips for magneto-thermal microscopy

Jamie Holber,¹ Chi Zhang,² and Gregory Fuchs²

¹*Department of Physics, Brown University, Providence, RI 02912*

²*Department of Applied and Engineering Physics, Cornell University, Ithaca, NY 14853*

The magnetic imaging of a ferromagnet is important to the development of spintronics. Magneto-thermal microscopy is one such method of magnetic imaging. The resolution of the microscopy is dependent on the size of the heat source used in the microscopy. A very sharp gold plasmonic antenna could provide a solution to high resolution imaging. The sharpness of the tip is essential to high quality microscopy. In this report we study a new method to produce a sharp gold tip using electromagnetic etching.

I. INTRODUCTION

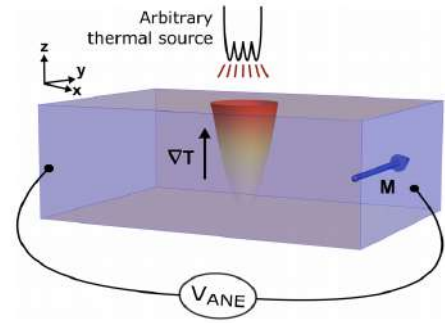
Recently there has been increasing interest in the field of spin-based devices, or spintronics. Spintronics relies on precise control of the magnetic moment throughout the entirety of a material⁷. Finding ways to control the magnetic moments relies on microscopy that can observe magnetic phenomenon at the nanoscale. One method of measuring the magnetic moment is by applying a thermal source in the Z direction to the ferromagnetic material and measuring the voltage across the material in the Y direction as in Figure 1a. The thermal source causes a heat gradient through the Z direction of the sample, which interacts with the magnetization in the Y direction to produce a voltage, $V_{ANE} \propto |\nabla T \times M|$. Given the thermal source and by measuring the voltage, we can calculate the magnetization at each position in the Y axis. The resolution of magnetization across the Y axis is roughly equal to the diameter of the thermal source at the point of contact with the ferromagnet.

Traditionally, a laser has been used as the thermal source. However, using light limits the resolution to a few hundred nanometers, due to the diffraction-limited focal resolution⁷. Our group simulated a new technique using a gold plasmonic antenna of sub-100 nm diameter. A light is shined on the conical antenna exciting the surface plasmon polaritons, as shown in Figure 1b. When the apex of the antenna is within a few nm of the surface of the ferromagnet there is electromagnetic loss in the sample creating a heat gradient. The FWHM of the electromagnetic loss grows with apex radius at 0.95 nm/nm for apex radii below 30 nm, and grows with apex radius at 3.73 nm/nm for apex radii above 30 nm⁷. The tip radius is therefore crucial to the resolution of the magneto-thermal microscope.

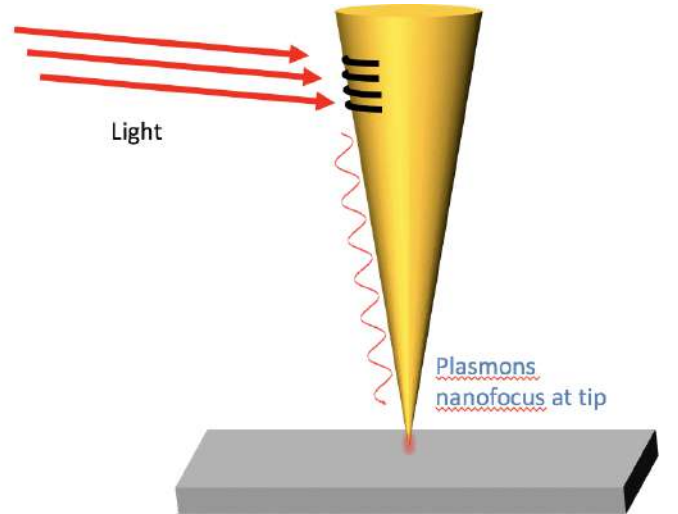
There have been at least 10 different techniques used to produce metallic tips for use such fields as electron microscopy, field ion microscopy, scanning tunneling microscopy⁴, and Raman spectroscopy. However, reliable and cost effective methods are still being explored. Some explored techniques are mechanical cutting^{2,5}, ion milling⁵, grinding⁸, beam deposition⁸, and using a field ion microscope in a vacuum²,

One of the most practical and reliable methods for tip

production is electrochemical etching^{1–5}. A fast control method is imperative in order to create a sharp tip. This project compares two control methods for stopping the current: a homemade differential cutoff loop, and a preset cutoff current.



(a) The thermal gradient, ∇T , produced by a thermal source interacts with the magnetization of the ferromagnet to produce a voltage⁷.



(b) Magneto-thermal microscopy with a gold tip as a heat source

FIG. 1: Magneto-thermal microscopy

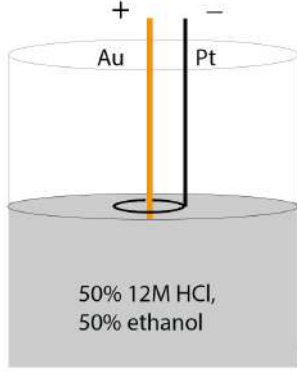


FIG. 2: Diagram of the setup for preparing the gold tip.

II. EXPERIMENT

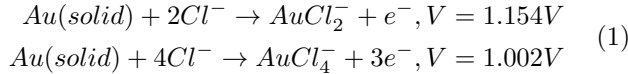
A. Preparation of Tips

A gold wire of 0.05 mm is used to create the tips. The wire is cut into pieces approximately 1 inch in length. These pieces are then annealed at 800 C for 8-10 hours. They are then cooled at 0.5 C/min to 300 C, then cooled at 40 C/min to 50 C, before being allowed to naturally cool to room temperature.

B. Electrochemical Etching

The gold tips are etched in a solution of 50% 12M HCl, and 50% ethanol. There are other possible solutions, but the advantage of HCl is that it is non-toxic and has a low etching voltage²(~2 V). The setup used is shown in Figure 2. The gold wire is immersed several millimeters in the solution and a 500 μ m platinum wire is placed on the surface of the solution with the voltage applied across them.

The electrochemical etching is governed by several redox reactions, shown below with their potential thresholds³. The gold atoms at the surface are dissolved, the rate being determined by the voltage applied. The gold atoms are dissolved more quickly at the surface because there is a higher concentration of Cl^- .



In this project, the tip is formed in two steps. A threshold voltage is found based on the minimum in the IV curve. Etching below the threshold voltage creates a smooth tip, but not very sharp. Etching above the threshold yields a very sharp tip, but is not as smooth. The first step is with a voltage about 0.1 V below the threshold, and the second step is with a voltage about 0.1 V above the threshold. By using the lower voltage

we create a longer smooth tip, then applying the high voltage creates a sharp tip at the end.

This project relies on the 'drop-off' method. When the diameter of the wire at the interface is sufficiently small, the weight of the immersed wire exceeds the tensile strength of the necked region and the lower part of the wire will break and fall⁴. At the point of falling, the current applied to the wire drops significantly, and the tip is at its sharpest point. If a voltage continues to be applied then the wire will continue to be etched and will start to become more dull. An important part of the method is to stop the voltage through the wire as quickly as possible (ideally in the range of several hundred nanoseconds). There are two main approaches. One approach is setting a cutoff current, and if the current drops below this point, the power supply will be shut off. The other approach is monitoring the current, and shutting off the system when the differential current decreases.

C. Preset Current Cutoff

The current method used in our lab to etch relies on a Keithley, which both supplies voltage to the gold wire, and measures the current across the wire. Labview controls the Keithley, dictating the voltage output and monitoring the current input. When the current drops to the preset cutoff (0.005 A), labview will shutoff the Keithley's output and etching will cease. The problem with this method is that between the current dropping, the Keithley has to measure the current, relay the information to the computer, which sends information back to the Keithley, before the power is shut off. This delay is likely several ms and means the tips are not as sharp as they could be.

D. Differential Current Cutoff

A second method for shutting off the current is to use a homemade differential current cutoff circuit shown in Figure 3a based off of the circuit described by Anwei et al⁴. When the lower part of the wire drops, the current through the wire will drop as well. We then expect to see a large drop in the dI/dt curve, as shown in Figure 4. We can utilize this spike to shut off the system.

The circuit consists of a current to voltage converter, a differentiator, a comparator, and a D type flip flop(latch). The current to voltage converter is an op-amp circuit, shown in Figure 3b, while the passive differentiator is shown in Figure 3c. We decided to use an op-amp as a comparator instead of an actual comparator, because the op amp was more reliable. The latch is a D type positive edge triggered flip flop where the output of the comparator goes to the clock input of the flip flop.

First the current is converted to voltage, as shown in Figure 3b, where $V_{out} = -RI_{in}$. Then the differentiator takes the derivative of the input voltage, so

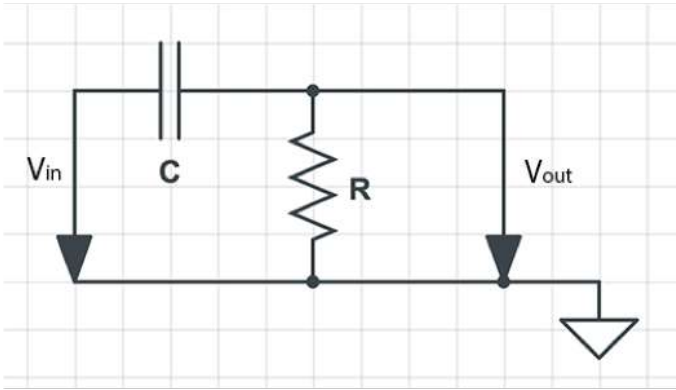
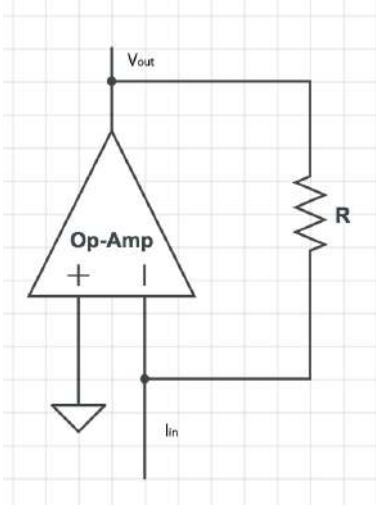
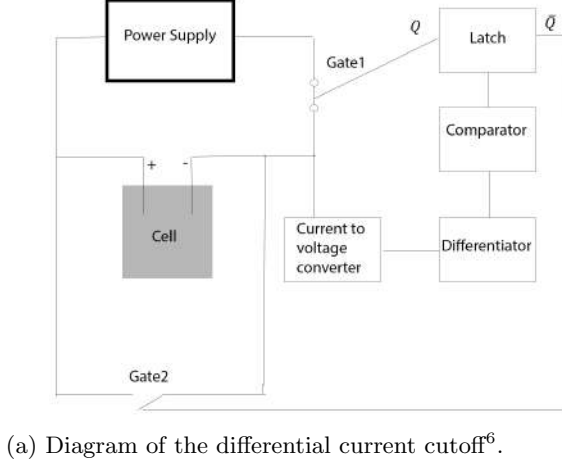


FIG. 3: The differential cutoff circuit

$V_{out} = RC \frac{dV_{in}}{dt}$. V_{out} of the differentiator is approximately equal to zero except when the lower part of the wire drops, when $V_{out} \approx -0.2$ V. The two inputs to the comparator are V_{out} and ground. When V_{out} is larger than

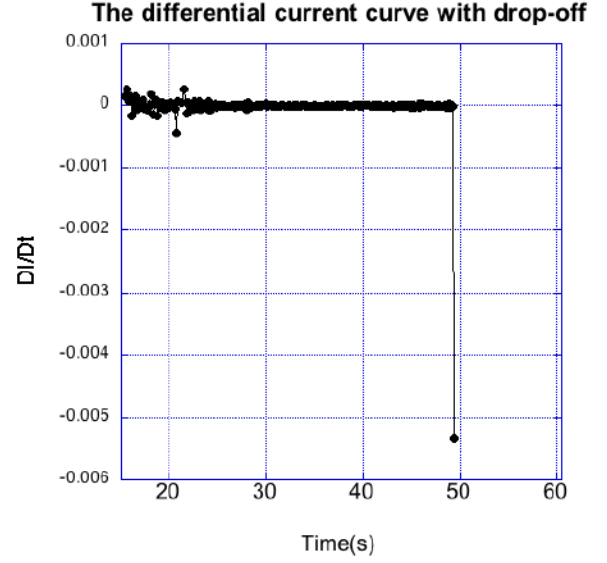


FIG. 4: Plot of the derivative of current with respect to time for a sample tip

ground the comparator's output is low (~ 0.030). When V_{out} is smaller than ground the comparator outputs a high voltage (~ 3.9) and triggers the flip flop so that Q becomes high and \bar{Q} becomes low. The flip flop output is ~ 0.135 for low outputs and ~ 4.5 for high outputs. The Q and \bar{Q} are applied to the base of PNP transistors. For PNP transistors, if the base input is < 0.7 then the transistor operates as a closed gate, otherwise the transistor operates as an open gate.

Before the current drops Gate 1 is closed and Gate 2 is open. Once the current drops, Gate 1 opens and Gate 2 closes. The opening of Gate 1 causes current to stop flowing through the system. Any residual current should go through Gate 2, instead of the cell, because gate 2 is closed and will have a much lower resistance. The time delay of the circuit is determined by the two op-amps (< 100 ns), the flip flop (40 ns) and the transistor (75 ns). The circuit is expected to have a delay time of less than 500 ns and be much faster than using an ammeter and computer, and therefore would be expected to make sharper tips.

E. Imaging

We used a Focused Ion Beam (FIB) to image the tips we etched. We first had to remove the tip from the cell, from Figure 3a, with tweezers. We then had to glue the tip to a sapphire substrate slide. We next transferred the slides to a SEM sample holder. Copper was then glued on top of the tips for grounding during imaging. The slides could then be imaged. This process is very tricky

and often tips are broken during one of the steps.

III. RESULTS

A. Testing

Once setting up the circuit we first tested to make sure that when there was a drop in current, the circuit responded and the current was cut off. To test this we replaced the cell portion of the setup, Figure 3a with a resistor of a similar resistance to model the stage of etching before the drop off point. We then dropped the voltage, which in turn decreases the current across the circuit, which approximates what would happen at the drop off point. Even though the voltage does not actually drop in the real etching, the voltage across the cell would increase in proportion to the rest of the circuit because of the increase in resistance in the cell.

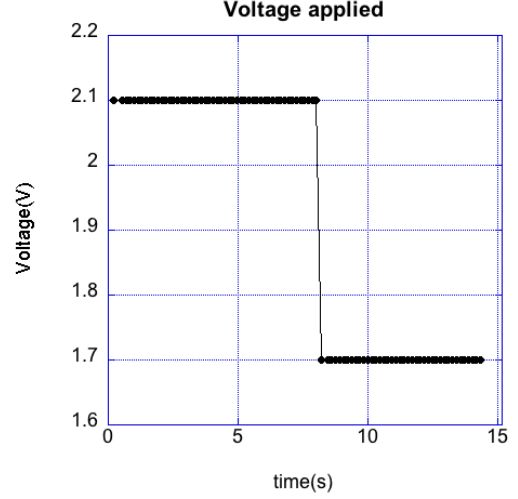
We used the computer to apply a voltage across the resistor and circuit and had the voltage switch from 2.1 V to 1.7 V after a few seconds, shown in Figure 5a. We then used the circuit in the off position as the control to compare against the circuit in the determine if the circuit works. With the circuit off, the current decreases from ~ 0.006 to ~ 0.004 A as shown in Figure 5b. When the circuit is on, the circuit decrease from ~ 0.006 to ~ 0 A, shown in Figure 5c. The decrease in current due to the voltage decreasing as shown in Figure 5b leads to the circuit opening gate 1 and closing gate 2. The current does not completely reach 0, but drops to $\sim 10^{-11}$ A. We used a normal switch, but a high quality more expensive switch would likely cause the current to be completely cut off.

This testing shows that the circuit is capable of cutting off the current to near-zero and given the parts used could be significantly faster than the computer at responding to a change in current.

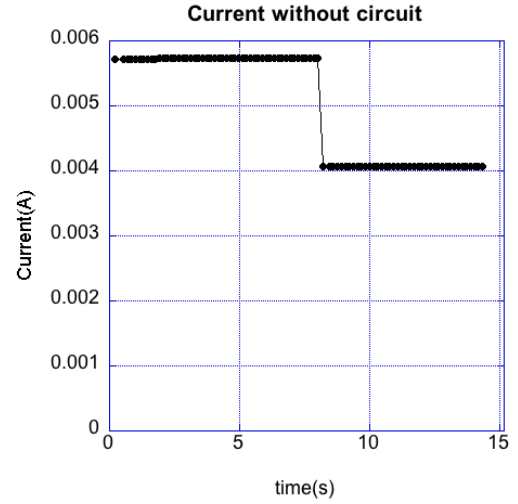
B. Etching

We etched gold wires using both the preset current method, with a computer monitoring the current and controlling the power supply, and the differential current cutoff method. The best tip produced with the preset current method is shown in Figures 6a and 6b and is about 75 nm across. The smallest gold tips in the literature are about 10 nm, and many are below 50 nm⁴. In the past we have produced smaller tips, but most are 50 nm or larger.

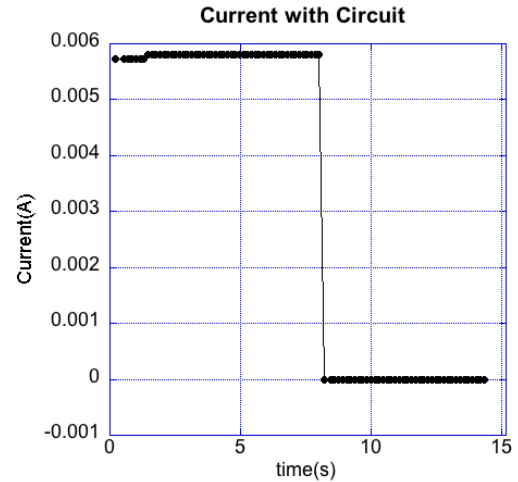
We also etched using the circuit in addition to the computer method. We still used the preset cutoff so that when the current was cutoff the power supply was shut off automatically. We found that the current measured changed significantly when the circuit was introduced to the system. In addition the current increased when the voltage increased with the circuit but decreased when the



(a) The voltage applied to the system to test the circuit

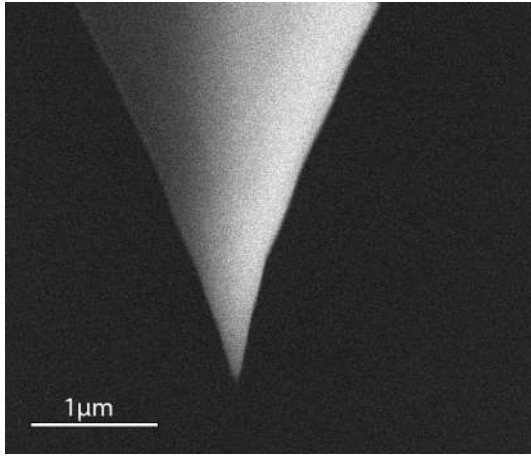


(b) How the current responds to the change in voltage without the circuit

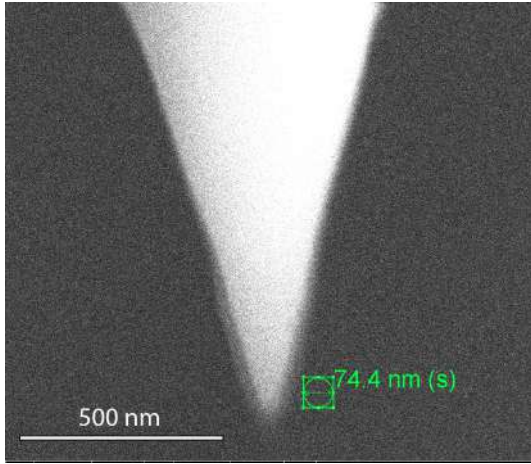


(c) How the current responds to the change in voltage with the circuit

FIG. 5: The results from testing the circuit

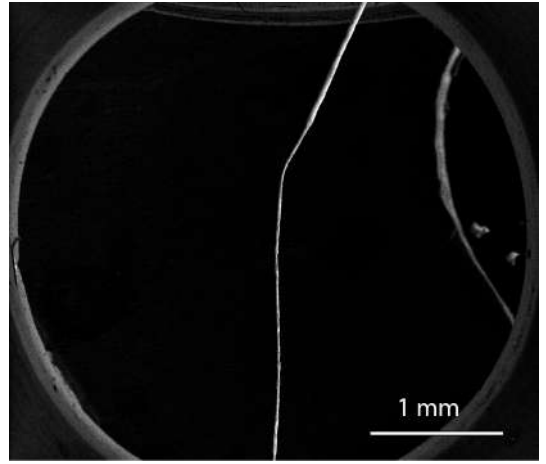


(a)

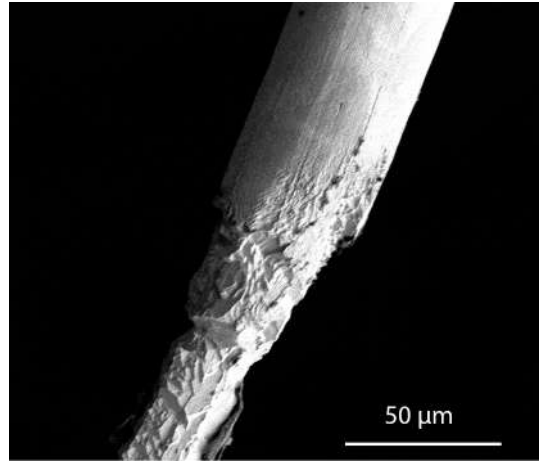


(b)

FIG. 6: Tip produced using preset current cutoff method



(a)



(b)

FIG. 7: Tip produced using differential current cutoff method

voltage increased for the computer method. The decrease in the current is due to the increased resistance throughout the system. We found that the closed gate and the path through it had a lot higher resistance than what was assumed. The change in the relationship of current and voltage is assumed to be due to the fact that the wire was being etched in the preset current cutoff method, and the wire was hardly etched in the differential current cutoff method.

The gold tip for the differential current cutoff is shown in Figures 7a and 7b. In Figure 7a you can see that there is a thinner part of the wire and a thicker part. The thinner part of the wire was in the acid and the thicker part was in the air. This implies that the drop-off point did not happen when the circuit cutoff the current. Instead, there was probably a smaller decrease in current that was enough to trigger the flip-flop. The circuit ended up being too sensitive to small changes in current.

To correct for the sensitivity there could be a change in the resistors for the current to voltage converter and the

differentiator. An increase in the resistor for the current to voltage converter, and a decrease in the resistor for the differentiator would both make the circuit less sensitive. In addition, ground was used as the other input for the comparator because the output of the differentiator must be significantly below zero for the comparator to output the high voltage. Instead, an additional power supply could be used to compare, which could also solve the problem.

In addition to the over-sensitivity, the wire does not etch much with the voltages we have been using. In Figure 7b, it is clear even after etching for about 66 s, the wire near the interface between the air and water is barely etched, due to the addition of the circuit. There will need to be further testing to determine if there is a different optimal voltage, or if the wire will need to be etched for much longer.

IV. CONCLUSION

From the testing it is clear that with better switches, the differential circuit cutoff method is a viable method to cutoff the current more quickly than using a computer to monitor the current. However, we need to solve the problem of oversensitivity and to find the optimal voltages to apply to the gold wire. With a faster cutoff time we could make gold tips that are less than 25 nm⁴ creat-

ing a much more accurate magneto-thermal probe.

V. ACKNOWLEDGEMENTS

I would like to thank the entire Fuchs group, especially Professor Gregory Fuchs and Chi Zhang for their mentorship. This work was supported by the Cornell Center for Materials Research with funding from the NSF MRSEC program (DMR-1719875) and the REU Site program (DMR-1063059).

-
- [1] M. Lopes, T. Toury, M. L. De La Chapelle, F. Bonaccorso, and P. G. Gucciardi, *Rev. Sci. Instrum.* 84, 073702 (2013).
 - [2] B Ren, G Picardi, and B Pettinger. *Review of Scientific Instruments* 75, 837 (2004); doi: 10.1063/1.1688442
 - [3] J. J. Lingane, *Journal of Electroanalytical Chemistry* (1959), vol. 4, no. 6, pp. 332-342, 1962.
 - [4] Boyle MG, Feng L, Dawson P. Safe fabrication of sharp gold tips for light emission in scanning tunneling microscopy. *Ultramicroscopy* 2008;108:558-66.
 - [5] L Anwei, H Xiaotang, L Wenhui, J Guijun. *Review of Scientific Instruments* 68, 3811 (1997); doi: 10.1063/1.1148032
 - [6] Simpson, R. E. (1987). *Introductory electronics for scientists and engineers*. Boston: Allyn and Bacon. pp. 133, 428
 - [7] J Karsch, J Bartell, and G Fuchs. *APL Photonics* 2, 086103 (2017); <https://doi.org/10.1063/1.4998757>
 - [8] Y. Khan, H. Al-Falih, Y. Zhang, T. K. Ng, and B. S. Ooi, *Rev. Sci. Instrum.* 83, 063708 (2012).

3D Printing Porous Monoliths in Microfluidic Device to be Used in Protein Separation

Saman Khorasi¹, Jen-Yu Huang², Tobias Hanrath³

Abstract: Protein separation in a microfluidic device is a relatively novel idea. The ability to confine the separation process to a micrometer scale allows for fewer resources to be used and almost instantaneous results which would be useful in clinical settings where small samples need to be tested. In this study, we use a microfluidic device composed of a body polydimethylsiloxane (PDMS) rested upon a transparent microscope glass slide. Ultraviolet light (UV) patterns provided by a digital light processing printer are shined into a microfluidic channel that is filled with a zirconia-based ink. The reaction of the ink and UV light produces a highly porous monolith. The high surface area means more active sites can be created for the separation process. Through analyzing many results, we were able to determine the optimal size of the images being projected and the ideal concentration of zirconia in the ink to produce the highest resolution images possible. Future work involves redesigning the microfluidic chip with a UV transparent backing and figuring out a mechanism to print even smaller images to allow for a finer separation process. Nonetheless, the methods development discussed in this paper shows promising results for the field of small-scale protein separation.

Introduction:

Previously, various methods of protein separation have allowed us to analyze the functions of proteins and their applications in various fields. This multi-step process, although effective, requires a high volume of resources and is time consuming [1]. The most common approach of protein separation, column chromatography, requires a tedious column preparation and when applied to the micro scale, it is not as efficient [2]. By scaling down the process using a microfluidic device, we are able to confine the separation and use a fraction of the reagents and energy. An alternative method of protein separation uses stationary phases such as monoliths, [2] which can be successfully scaled down to the micro level.

These monoliths have a higher surface area, yielding more active sites for separation to take place. Previous studies have used silica beads, whose surfaces have been tagged with binding agents to separate proteins [1]. However, it can be difficult to control the precise location of these beads within the channel due to the high pressure of the liquid passing through the device. Furthermore, the beads have a limited surface area, which restricts the number of active sites that would be used for protein separation. These silica beads have been held in place using a gel to prevent them from moving during the flowing process, but this gel can restrict the flow of the protein solution due to its low surface area [1]. By having a stationary porous monolith inside a microfluidic channel, one would be able to efficiently and

¹ Georgia Institute of Technology, School of Material Science and Engineering, Atlanta, Georgia

² Cornell University, Department of Chemical and Biomolecular Engineering, Ithaca, New York

³ Cornell University, Department of Chemical and Biomolecular Engineering, Ithaca, New York

effectively separate proteins in comparison to previous methods.

In this work, we use a 3D printer to control where we want to print images in the microfluidic channels that would be used in protein separation. We tested multiple types of shapes and sizes before finding the optimal arrangement that was to be used. By using a resin based with a high porous material and confining it in a channel, we are able to increase the number of active sites, thus increasing the efficiency of protein separation and minimizing the number of resources to do so.

Experimental section:

The microfluidic device that we used contains parallel, micrometer sized channels. The channel design is etched onto a wafer using photolithography.

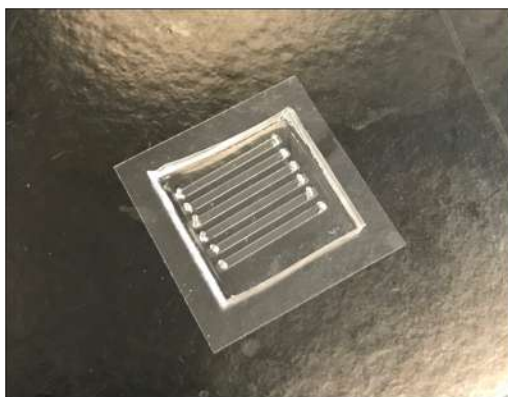


Figure 1: Microfluidic device that was used throughout the experimental procedure

Polydimethylsiloxane (PDMS) is poured on top of this design and allowed to cure. This polymer layer is then bonded to a glass slide or any other sturdy, clear platform. Small holes are punctured at the opening and closing of each channel and small tubes are

attached to these holes to allow for the liquid to flow through.

After the device was made, we formulated the ink that would be used in the printing process. Zirconia crystal was combined with a small amount of photo initiator (PI) and a solvent. This solution was sonicated for 5 minutes and then purged with nitrogen for 3 minutes to remove any oxygen that would inhibit the reaction. Prior to printing, the images were designed in PowerPoint. The slide that would be projected had a black background with the images being white.

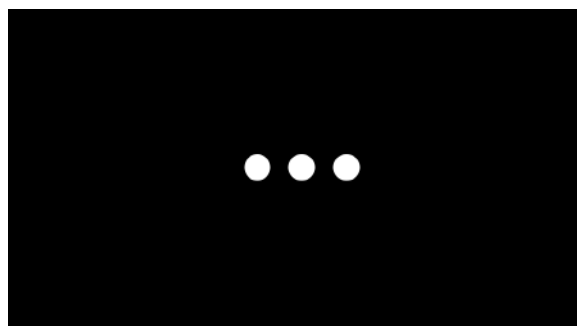


Figure 2: Example of what the projected slide looked like.

In order to print, a device was hooked up to the DLP printer that would contain the slides that were to be projected. The printer was turned on and the image was allowed to project onto the platform. The microfluidic device was then lined up with the image, making sure that the image was projecting into one channel.

The ink was loaded into the channels and reacted with the UV light for 10-15 minutes. After the reaction was completed, the remaining ink was pushed out of the channel with a syringe. The channel was then rinsed with toluene to remove any existing ink. Methanol was then added to prevent the images inside from drying or cracking.

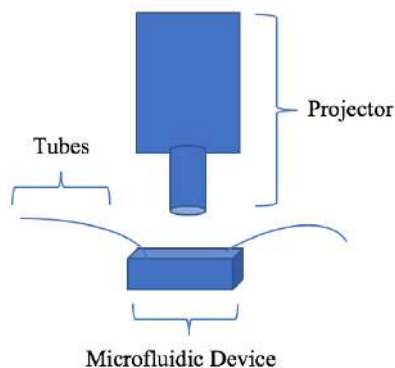


Figure 3: Set up of the microfluidic device and projector during the experiments.

Results:

After the samples were covered in methanol, they were taken to a high-power microscope to get measurements. For every 1 centimeter that was drawn on the computer, 2.5 millimeters was projected. From this conversion, an image size was estimated. The actual image, when examined, was actually smaller than what was estimated.

Size on the Computer	Theoretical Size (um)	Actual Size Printed (um)
4.3 mm	1075	843
3.5 mm	875	668
3.8 mm	950	716
1.5 mm	375	311
1.25 mm	312.5	285
1.0 mm	250	190

Figure 4: Table of the predicted sizes of the samples versus the actual size that was printed out.

The resolution of the images was also not as clear and defined as we had predicted it to be. When using commercial resin to test which

shapes would print the best in the channels, we found that shapes that had minimal edges such as circles or triangles were more successful in holding to their true shape than shapes with more edges such as stars.



Figure 5: Sample of a microfluidic channel. The image with fewer edges (triangle) printed better than the images with more edges (stars).

Nonetheless, even those images were not as defined as we expected them to be. Furthermore, for the channels that contained small images of only 1-2 millimeters, the reaction took place very slowly or the ink did not react at all.

Discussion:

Since the resolution of the images was not up to par with what was expected, we changed our approach for printing. The channels were closer to the glass slide than they were to the surface of the PDMS so we decided to shine the UV light through the glass slide.

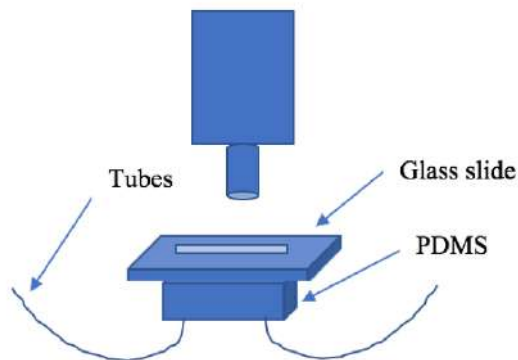


Figure 6: Proposed bottom to top printing method to achieve better resolution.

However, when this theory was tested out, it was not successful. We found that although the glass slide was very thin, it had a lower transmittance for UV light than the PDMS did. We reverted back to the old method of printing from the top down, through the layer of the PDMS. We tried reducing the thickness of the layer of PDMS as well so that the projected light was as close to the channels as possible. But, the needles that attached the tubes to the device would not stay connected to the channels and as a result, it was very difficult to flow liquid through them. Nevertheless, the resolution of the images can still be improved. In the next step of this experiment, the glass slide will be replaced with either quartz or TPX RT 18, both of which have a higher transmittance than PDMS. Doing so could yield higher resolution images and a shorter reaction period.

Another solution that was proposed to produce better images was to increase the concentration of zirconia in the ink. It was noted that each subsequent time the ink from the same batch was used, the reaction would take longer to complete. We hypothesized that by increasing the concentration of zirconia, there would be more ligands to connect and create a stable network, which would create a more defined image. In the formulation of this new ink, we noticed that the same amount of solvent that was used previously was not sufficient enough to completely dissolve the increased amount of zirconia crystals. Rather than increase the amount of solvent and lower the concentration of the overall ink, the solvent was changed to toluene. Toluene was better able to dissolve all the zirconia crystals and did not lower the concentration of the ink. As a result, we were able to use the same sample of ink multiple times and get consistent results.



Figure 7a: Image with initial zirconia concentration.

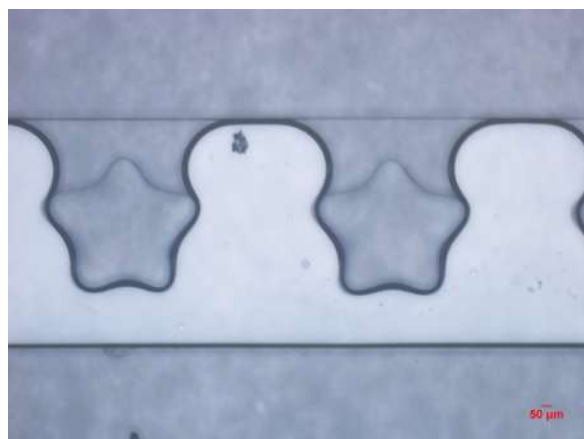


Figure 7b: Image after doubling the concentration of zirconia

Now that a printing method and ink formula had been finalized, the next step was figuring out which pattern of images would be best for the protein separation process. We knew from our test with the commercial resin that images with minimal edges printed the best. As a result, we decided to create an array of circles. Since the zirconia ink has a high surface area, we wanted to have as many circles in the array as possible so that more proteins could be separated in one experiment. Each circle was 1 millimeter in diameter and the columns of circles were

separated by 2.75 millimeters. We discovered earlier that small images took a long time to react or did not react at all. To solve this, we placed a larger image next to the array of circles that would initiate the reaction. This image still had room on all sides for the liquid to pass through so that the separation process could occur

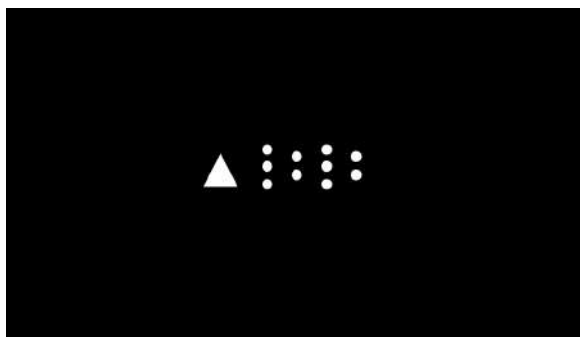


Figure 8: Proposed array design that is to be used in protein separation

The circles printed almost true to size with an expected size of 250 nanometers and an actual size of 220 nanometers.

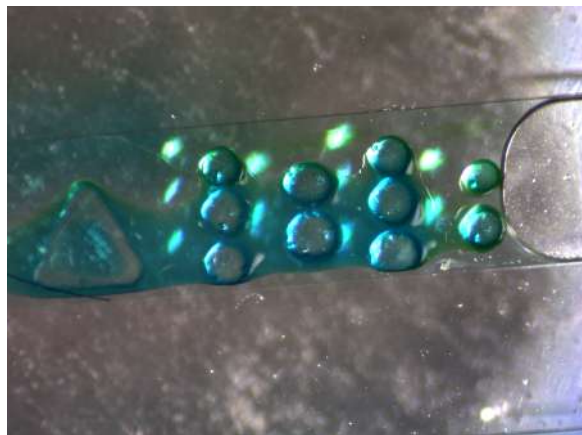


Figure 9: The actual array that was printed in the microfluidic channel. The blue methanol dye proves that liquid is able to get in between the crevices of the array and into the pores of the actual material.

Conclusions:

In summary, the most efficient printing method that we discovered involved using the top down printing approach and doubling the zirconia concentration in the ink. Furthermore, if small images were to be printed in the channel, a larger image should be placed inside the same channel to initiate the reaction. This method that we developed is the next step in small scale protein separation. The ability to pattern any device with a highly porous monolith means that the method can be implemented in various applications.

The next step in this project is to test the array in actually separating proteins. After the array is finished printing and rinsed with toluene, a solution will be flowed through to create active separation sites in the pores of the monolith. Following this, a protein solution will be inserted into the channel to be separated.

Acknowledgements:

This work was supported in part by the Cornell Center for Materials Research with funding from the Research Experience for Undergraduates program. I would also like to thank the Hanrath Lab for hosting me and Jen-Yu Huang for being my mentor this summer.

References:

- [1] Sarkar, A., Hou, H. W., Mahan, A. E., Han, J., & Alter, G. (2016). Multiplexed Affinity-Based Separation of Proteins and Cells Using Inertial Microfluidics. *Scientific Reports*, 6(1). doi:10.1038/srep23589
- [2] Rodríguez-Ruiz, I., Babenko, V., Martínez-Rodríguez, S., & Gavira, J. A. (2018). Protein separation under a

microfluidic regime. *The Analyst*, 143(3),
606-619. doi:10.1039/c7an01568b

Organic molecule as a cathode material for Li-ion batteries

Joshua Reyes Morales¹, Cara Gannett¹, Héctor Abruña²

Cornell University, Abruñas Electrochemistry Laboratory

Abstract: Modern society has begun to utilize more energy sources to meet our growing energy needs. One of the most used sources are the batteries where the majority are from Lithium. Some of the problems with these batteries include that the synthesis of inorganic materials leads to the production of toxic substances for the environment and these materials are expensive. Due to this, the use of organic materials has been considered as they are mostly non-toxic, low cost and their structure can be modified to change the properties of these materials to obtain a better performance of the batteries. In this work, this approach was carried out in a molecule derived from phenothiazine since it is known that its structure can be modified through synthetic means to obtain different properties that can be turned to optimize the performance of these batteries. Several molecules were characterized to identify the redox peaks of the polymer so that the stability of the active material could then be studied. Cyclic voltammetry studies of the polymer revealed a degradation process which could be slowed using different solvent systems and cycling through only the first two redox couples. From these studies, it appears that the third oxidation state is largely the cause of the degradation in the polymer.

1. Introduction

The rapid rise of technology in the modern world has led to an increased demand for energy and a need for more sources to provide it. This energy is used to power technology like cars, cellphones, and computers. One energy source used most is batteries, that most of them are made of Li-ion batteries. Batteries are not an energy source, they are a form of energy storage. Most commercial Li-ion batteries utilize inorganic materials, which store energy through a change of oxidation state of the metal [1]. The best inorganic material for Li-ion battery is LiFePO₄ because has high cyclability and non-toxic nature. However, this material works at low potential of 3.4 V [2]. Additionally, the material is expensive and its synthesis tends to release toxic metals into the environment [1]. Because of these problems, scientists are pursuing other materials to be used in Li-ion batteries.

There is an interest on organic materials because are low cost, benign to environment and the synthesis of these materials can be modified to tune chemical structure which in turn will change properties like solubility, capacity, energy density

and others. The ideal battery would have a long lifetime, low cost, and be benign to the environment. Typical capacities for commercial batteries are around 150 mAhg⁻¹.

Capacity is the maximum amount of charge that a material can hold per gram. If the material it's dissolved in the solution of the battery, is going to be troublesome because if there is a miss of the material, the battery is going to lose capacity. There is a relationship that is:

$$C_{\text{theor}} = \frac{nF}{(3.6)(MW)}$$

where n is the number of electron transferred, F is the Faraday constant, and MW is the molecular weight of the active material. Ideally, an organic material would be capable of multiple electron transfer and would possess a low molecular weight to obtain a high capacity.

The material studied here is a derivative of phenothiazine. Phenothiazine has been used for pharmaceutical purposes. One of the most known derivatives of this molecule is methylene blue. In recent research there is been an interest in using

derivatives of phenothiazine as an active material for Li-ion batteries. Some phenothiazine derivatives exhibit an oxidation potential of 3.9 V vs Li/Li⁺, which is 500 mV higher than that of LiFePO₄ [2]. Its chemical structure has been previously modified for pharmaceutical purposes, providing an existing knowledge base for modifying the structure for use as a battery material. For these reasons, a phenothiazine derivative is promising for a new cathode electrode material that exhibits high capacity, high redox potential and high cyclability [2].

2. Methodology

2.1. Sample preparation

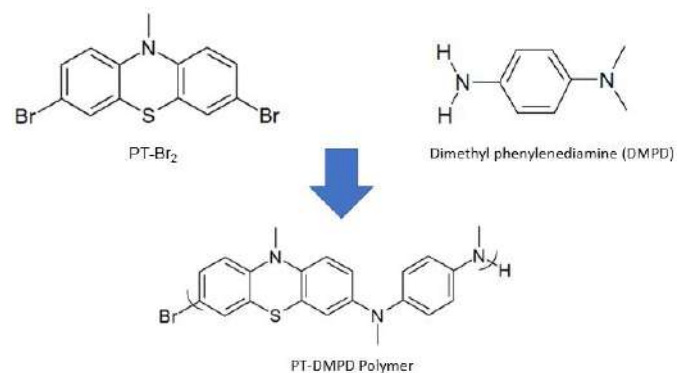
The polymer and other phenothiazine derivatives were previously synthesized by collaborators in the Fors group. The synthesis involved Buchwald-Hartwig cross-coupling of 3,7-dibromo-*N*-methylphenothiazine with dimethyl phenylenediamine, and is outlined in Scheme 1.

For electrochemical tests, the phenothiazine small molecules were prepared by dissolution into solution of 0.1M tetrabutylammonium perchlorate (TBAP) in acetonitrile (MeCN) at a 1 mM concentration. The polymer is insoluble and was prepared for electrochemical testing as a slurry. The slurry was prepared with a ratio of 3:6:1 of active material: Super P: polyvinylidene difluoride binder dissolved in 1.0 mL of *N*-Methyl-2-pyrrolidone (NMP). 2 μ L of the slurry were then drop cast onto the surface of a polished glassy carbon working electrode with a diameter of 3 mm and dried under a heat lamp to evaporate the NMP.

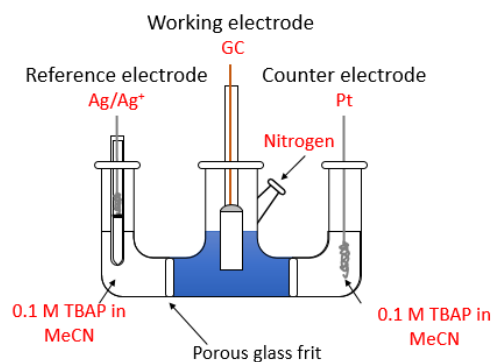
2.2. Characterization

To understand the chemical behavior of this polymer a series of small molecules were studied to compare the electrochemical chemical response using cyclic voltammetry. To identify the different peaks of the polymer the peak shifts of the phenothiazine small molecule derivatives were used to deduce which heteroatom gave rise to which response. The degradation process of the polymer was studied in different solvents two different solvents, nitrobenzene (NB) and propylene carbonate (PC). Electrochemical characterization was carried out by cyclic voltammetry. The working electrode was a glassy carbon with a diameter of 3mm,

reference electrode of Ag/Ag⁺ and a counter electrode of platinum. The electrochemical cell is depicted in Scheme 2. The solutions were purged with nitrogen to remove oxygen from the solvent. The scan rate used was 20 mV/s, unless otherwise noted.



Scheme 1. PT-DMPD polymer



Scheme 2. Electrochemical Cell

3. Results and Discussion

3.1. Characterization

To understand the response in the cyclic voltammetry experiments of the polymer, the CV response from different phenothiazine derivatives were compared to observe the redox potential shift relative to one another. In figure 1, the voltammogram of phenothiazine is shown. The first peak is the oxidation of the nitrogen group and the third is due to the sulfur group. In an attempt to obtain results which better match those seen in literature, where the second peak is not observed, the molecule was tested in an argon glove box (Figure 2). In an inert atmosphere, the second peak disappeared, which it is attributed to likely being due to the use of the MeCN which is kept in the glovebox and likely has fewer impurities.



Phase Transitions in Sodium Ion Batteries Upon Charging and Discharging

Malia Okamura¹, Daniel Weinstock², Andrej Singer²

¹Department of Materials Science and Engineering, Carnegie Mellon University,
Pittsburgh, PA 15289

²Department of Materials Science and Engineering, Cornell University, Ithaca, NY 14853

ABSTRACT: Lithium Ion Batteries (LIB's) are commonly utilized in technology and energy storage, however, Sodium is much more abundant than Lithium, and can potentially offer improved battery function and faster kinetics [1]. Analysis of Synchrotron X-ray diffraction scans of a charging and discharging Sodium Ion Battery (NIB) gives information about the particles in the battery and how they behave during charging and discharging. From the results, it is concluded that there is a phase transformation upon charging and discharging. More interestingly, some of the particles in the battery are proven to exhibit two phases in a single particle.

I. MOTIVATION

Cell phones, electric vehicles, and most rechargeable devices are popular nowadays, and there is a high demand for electric energy storage. Lithium ion batteries (LIB's) are utilized in all these devices [1]. The battery is very successful and researchers are constantly studying how to improve this battery [1]. Despite the success of the LIB, it is not practical to limit research to lithium. It is not considered an abundant element, and is unevenly distributed throughout the earth [1]. Because of this fact, it is moderately expensive and not easy to obtain.

Sodium on the other hand, is considered one of the most abundant elements in the earth's crust, as shown in Figure 1 [1]. It is found in the ocean and in many known minerals [1]. In addition, it is easy to synthesize and it is a low cost

element [2]. Sodium is also the most similar to lithium of the alkali metals in mass and in size [1].

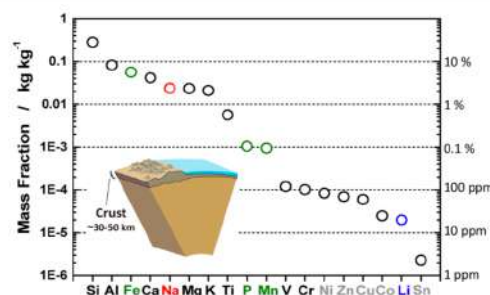


Figure 1: Elemental abundance in the Earth's crust.
Figure from [1]

In addition, the structures, components, and systems are similar [1]. Due to these findings, NIB's are an ideal replacement for LIB's. The bigger ionic radius of sodium allows for an increase in the flexibility of the

material design, which is an advantage over LIB's [1]. NIB's can also potentially offer faster kinetics because of its smaller diffusion activation energy [1]. In addition, sodium's higher ionic conductivity leads to increased battery performance [1]. These are some of the many reasons why NIB research is important.

II. INTRODUCTION

The material the Singer Lab utilizes in the NIB is called layered P2- $\text{Na}_x[\text{Ni}_{1/3}\text{Mn}_{2/3}]\text{O}_2$ where x is a number between zero and $1/3$ depending on its charged state [2]. As the battery becomes charged, the sodium ions are removed. This material is potentially a good low-cost NIB cathode [2]. The structure of the different materials can be of P2 or O3 type [2]. The letter (P or O) refers to the site that the ion occupies (prismatic or octahedral (see Figure 2)) and the following number refers to the number of ion layers in the repeat unit of the structure [1].

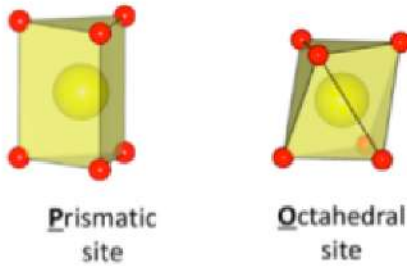


Figure 2: Image of Prismatic and Octahedral sites
Figure from [1]

These different structure types have different stacking sequences as seen in Figure 3 [2].

As sodium ions are removed upon charging, the structure increases its volume due to repulsions [1]. Because of the volume increase, phase transitions occur. This particular material shows a P2 to O2 phase transition seen in Figure 3 upon charging above 4.2 volts (V) [2]. Once the concentration of sodium reaches $1/3$, the O2 phase becomes more stable [2]. This phase transition was also shown to be reversible

upon discharging [2]. A voltage versus time graph shows three plateaus, which indicates that there is three phase transitions and therefore there are two more stable intermediate phases apart from P2 and O2 [2]. However, phase transitions are not wanted as they cause slow nucleation and defect formation [4].

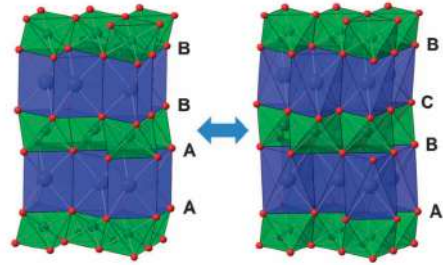


Figure 3: P2 structure (left) and O2 structure (right)
Figure from [2]

III. EXPERIMENTAL

To prepare the battery sample, a small opening was created in the center of the coin cell, and then sealed with Kapton film to allow the x-rays to penetrate the battery material [4]. The Kapton that is used to seal the opening does not affect the electrochemical performance of anything [4]. The sample was then mounted, and the detector was set to a specific 2θ value and a certain distance d away from the detector [4]. The sample was irradiated with 15-kilo electron volts (keV) photon energy while rocking the sample back and forth (see Figure 4).

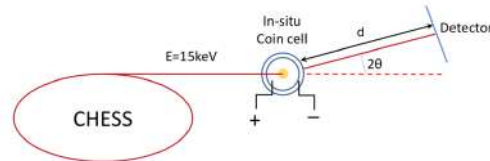


Figure 4: Schematic setup of the experiment
Figure from [6]

The rocking of θ (back and forth) allows for a full 2D image of the Bragg peak. Portions of the Debye-Scherrer rings for different planes are recorded on a charge-coupled

device (CCD) [4]. We expect to see the 002 (highest intensity), the 004, and maybe the 100 planes diffract [2]. Once these images are obtained, Matlab was used to extract information from the 4D data set. There are many “cubes” of data according to the number of scans. The dimensions are 2θ , θ , and χ illustrated in Figure 5. By stacking and extracting data, we are able to see the many peaks, and observe their movement and behavior.

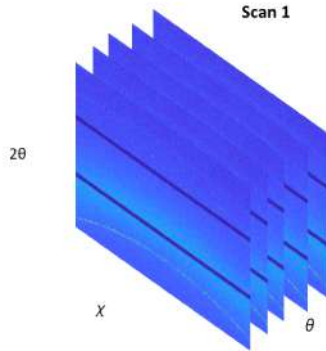


Figure 5: 4D Data set

There were four sets of data used in data analysis as seen in Table 2, each sample run with a different 2θ values, and with different charging rates. From the resulting data, Matlab was used to extract useful information about the Bragg peaks of the 002 ring.

Table 1: Recorded data

Sample	Charging Rate	2θ
B2_S7 charging	C/10	11.29
B2_S7 discharging	C/10	11.29
B2_S9 full scan	C/3	11.79
B3_S10 full scan	C/10	11.79

IV. RESULTS

First, looking at the average images of the 002 Debye-Scherrer ring portion scan after scan, a phase transition is clearly visible. There is first only a presence of one

ring, and then it splits into two, indicating a phase transition upon charging.

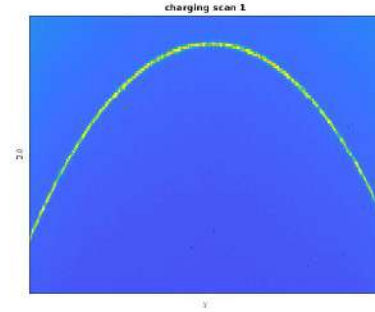


Figure 6: 002 ring in scan one. One phase present

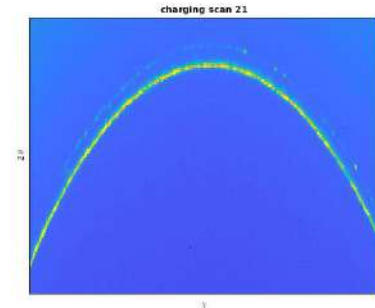


Figure 7: 002 ring in scan 21. Two phases present

After retrieving these images, the rings were flattened, and averaged over χ to create a line scan. As seen in Figure 8, it is easier to see the phase transition and when it occurs.

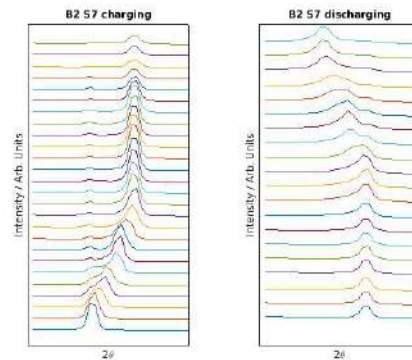


Figure 8: Line scan of flattened rings showing the phase transition upon charging and discharging.

In order to obtain information about the peaks and to determine if the two phases exist in a single particle or two separate particles, the 2D Bragg peak is needed. All images from one scan that were rocked in theta were stacked, and the portion of the block that both rings are present was extracted and averaged into one 2D image. This process was done over all the scans.

Now, looking at specific peaks gave information about each particle. Using a peak finding program, and creating a line scan of each peak along 2θ showed if there was two phases present in a single particle. If there were two phases present, there should be two intensity peaks at the same 2θ values as the two flattened rings. If only one phase is present, there would only be one peak, and the 2θ value it is at corresponds to that phase.

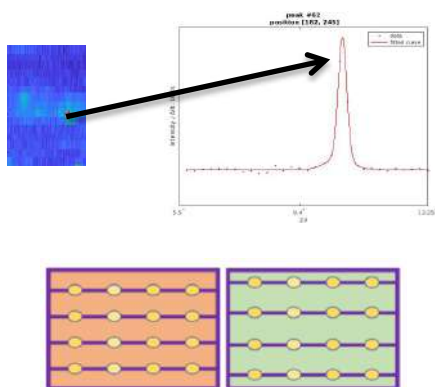


Figure 9: Peak coming from a particle with one phase present

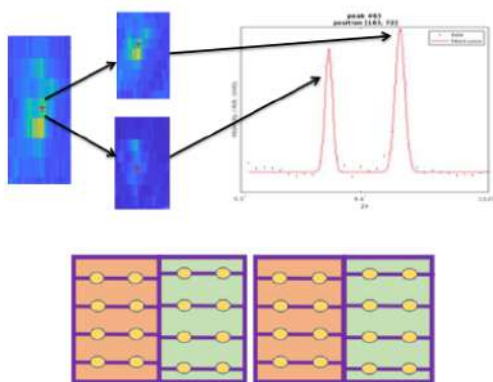


Figure 10: peak coming from a particle with two phases present

To prove that these peaks come from the same particle and it's not just a coincidence that they overlap, the relationship of θ and 2θ comes in handy. Due to the d spacing of each phase and assuming the planes of the two different phases are parallel, the relationship between θ and 2θ is half. In other words, the shift in θ should equal half the shift in 2θ .

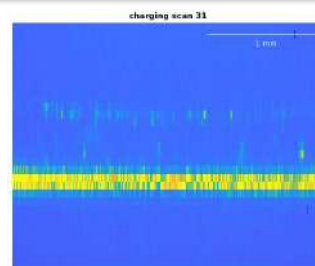


Figure 11: Flattened rings showing shift in 2θ

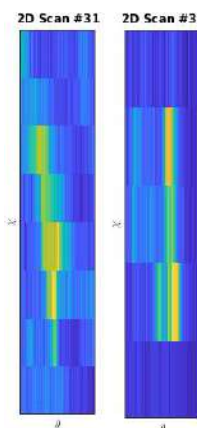


Figure 12: Peaks found on the two rings at the same location

The shift in 2θ was calculated by use of geometry. The distance between the two rings is known as well as the distance between the sample and the detector. This allowed for calculation of the shift in 2θ . To determine the theta value of each peak, the peak image was averaged over χ , and the highest intensity position was considered the theta value of the peak. Comparing the values, for the peaks in Figure 11, the shift in the 2θ value was $.21^\circ$ and the shift in the theta values was $.1^\circ$. The ratio of these values is 2.1, which is close to double. Some other peaks exhibited this ratio but they are all slightly off. This is because there is some

error to take into consideration. There is still some lingering background noise, and the peak shapes are funky, so the determination of the theta value of the peak is a bit off. Nonetheless, this ratio proves that the two peaks come from the same particle, and it is not a coincidence that these two peaks happen to be in the same position. This proves that there are two phases present within this single particle.

V. CONCLUSION

In Conclusion, a phase transition is observed upon charging and discharging for this sodium ion battery as shown by the ring splitting in Figures 6 and 7. There are some particles that show peaks in both phases meaning that some single particles contain two stable phases.

ACKNOWLEDGEMENTS

This research was supported by the Cornell Center for Materials Research and the National Science Foundation. Special thanks to the Singer Lab, my mentor Daniel Weinstock, and my Professor Andrej Singer for a great research experience.

REFERENCES

- [1]. Naoaki Yabuuchi, Kei Kubota, Mouad Dahbi, Shinichi Komaba, "Research Development on Sodium-Ion Batteries", Chemical Reviews, November 2014, pg. 11636-11682
- [2]. DaeHoe Lee, Jing Xu, Ying Shirley Meng, "An advanced cathode for Na-ion batteries with high rate and excellent structural stability", Phys. Chem. Chem. Phys., 2013,15, 3304-3312
- [3]. Barnes, Paul, et al. "Powder Diffraction." Structure Refinement III: Rietveld in Practice, pd.chem.ucl.ac.uk/pdnn/diff2/kine mat2.htm.
- [4]. Singer, et al. "Nonequilibrium Structural Dynamics of Nanoparticles in $\text{LiNi}_{1/2}\text{Mn}_{3/2}\text{O}_4$ Cathode Under Operando Conditions", Nano Lett. 2014, 14, 5295-5300
- [5]. Feng Lin, et al. "Synchrotron X-ray Analytical Techniques for Studying Materials Electrochemistry in Rechargeable Batteries", Chem. Rev. 2017
- [6]. R. Kumar, H.Hirsh, R.Buock, M.Zhang, D.Weinstock, O.Gorobstov, J.Ruff, Y.S.Meng, A.Singer, Phase Transformations in Sodium Ion-Batteries: in-situ X-ray Diffraction

To understand better the polymer behavior, the potential of the oxidation peak from the nitrogen of the phenothiazine was compared with the one of the PT-Br₂ (Figure 3). The redox potential was observed to shift to higher potentials with the attached bromines and methyl group. Bromine groups have an effect on the electrochemical behavior of a molecule due to an their electro withdrawing. The bromine atoms withdraw electronic density from the nucleus of the molecule and make it more difficult to oxidize the nitrogen group, shifting the peaks to higher potentials [3].

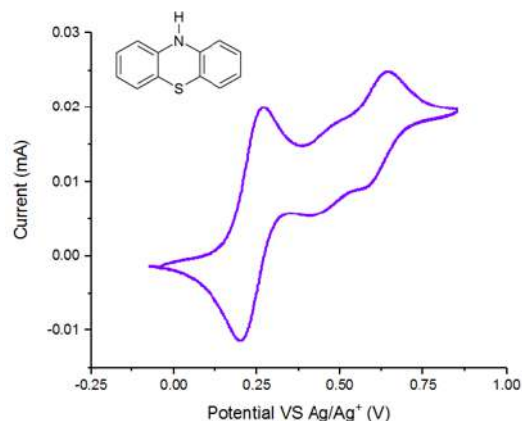


Figure 1. Phenothiazine Cyclic Voltammetry

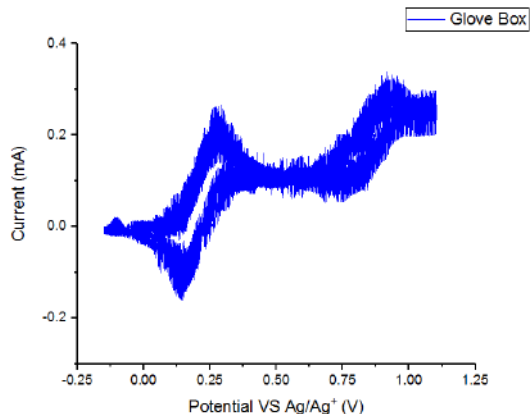


Figure 2. Phenothiazine characterization, glove box

After the characterization of PT and PT-Br₂, two more phenothiazine derivatives were characterized. Figure 3a and 3b show the cyclic voltammograms (CV's) of PT-(Ani)₂ and PT-N(Me)₂. The CV's show similar behavior, but with a shift in the oxidation potential. All of the peaks of the PT-N(Me)₂ have been shifted to more negative potential. The explanation for this is because methyl groups are more electro-donating than the benzene groups, so its going to be easier to oxidize the nitrogen with the methyl groups. To know which redox peak corresponds to which heteroatoms in the

molecules, we compared the magnitude of the shift of each of the peaks in these two CV's. It was observed that the first peak and the third peak shifted by about 150 mV, while the second peak only shifted around 50 mV. The most affected group by the electro-donating effect of the methyl groups will be the atoms that are directly linked to the methyl or benzene group. From this logic, we can infer that the nitrogen in the center of the molecule, will be less effected by the electron donating effect of the methyl groups, and its redox peak will shift the least. From this, we correlated this nitrogen giving rise to the second peak in the CV response. The first and the third peak then arise from the nitrogen atoms with the attached methyl/benzene groups. Although the two nitrogen's originally start out equivalent in the neutral molecule, once one is oxidize, the chemical environment of the other becomes different and more difficult to oxidize, as described by percolation theory. One will be oxidized first and the second will then be oxidized at a higher potential.

When obtaining the voltammograms of the different molecules, the characterization of the polymer was obtained by comparing the data. Figure 3d shows the cyclic voltammogram of the polymer. It has three main peaks that are labeled. The results of determining which peaks correspond to which heteroatom from the small molecule studies have been extended to the polymer response. We assume that the peaks in the polymer arise from the same heteroatoms which they were correlated to in the small molecules. The small peaks between peak two and peak three is related to one of the main peaks. It is known that polymers are chains of monomers with n monomer units. The monomers near the start of the polymer chain will feel an effect from the bromine atom which begins the polymer chain. As observed with the small molecule, the electron withdrawing effect will shift the redox potential of a group to more positive potentials. These small peaks then arise from the phenothiazine units at the beginning of the polymer chain, which are shifted anodically from this electron withdrawing effect. We do not observe a peak from the sulfur atom like we did in the phenothiazine molecule. A possible reason why the redox peaks of the sulfur group was not observed is because it appears at a high potentials where the electrolyte solution is unstable.

3.2. Degradation Process Study

To know if a material can be used for batteries

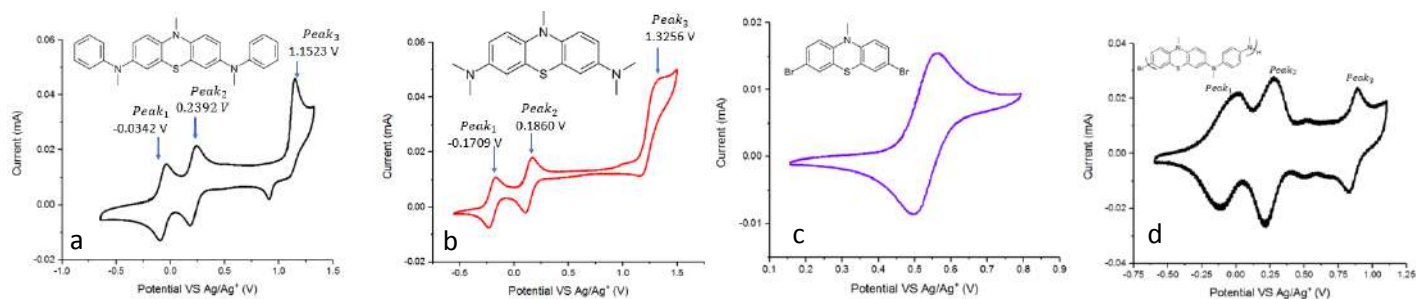


Figure 3. (a) PT-N(Me)₂, (b) PT-(Ani)₂, (c) PT-(Br)₂ and (d) PT-DMPD Polymer

the stability of it must be studied. The stability of the sample was studied by cycling the polymer through all three of its redox peaks ten times (Figure 4a). It was found that the first and third peak of the polymer started to decay rapidly, but the second one decreased more slowly, although a small shift in its potential also occurred. Isopotential points were observed in the cycling which indicates that there is some form of a conversion occurring in the polymer. A possible explanation to this problem may be due to the nucleophilic activity of the solvents. The same process was repeated using different solvents with less nucleophilic activity like NB (Figure 4b) and PC (Figure 4c). In these two cases the peaks all started to decrease uniformly, unlike what was observed in the MeCN. The sample run in the PC had the fastest decrease in its peaks. The sample in NB was observed as the most stable and least nucleophilic in this case. The normalized peak current was plotted versus the number of cycles for each of the samples to fairly compare the results in all three solvents (Figure 4d).

This stability test in the different solvents was repeated, but with cycling the polymer only through the first two redox couples. This was done to observe if the +3 oxidation state of the polymer was making the active material unstable. Figure 5 shows the stability of the polymer in the different solvents. Comparing the results with those performed when cycling through all three states, it can be clearly observed that the polymer is much more stable. With this, it is considered that the third oxidation state is linked to the degradation process of the polymer. These results show that this material would be suitable as a battery material if the potential range is limited to the second oxidation state.

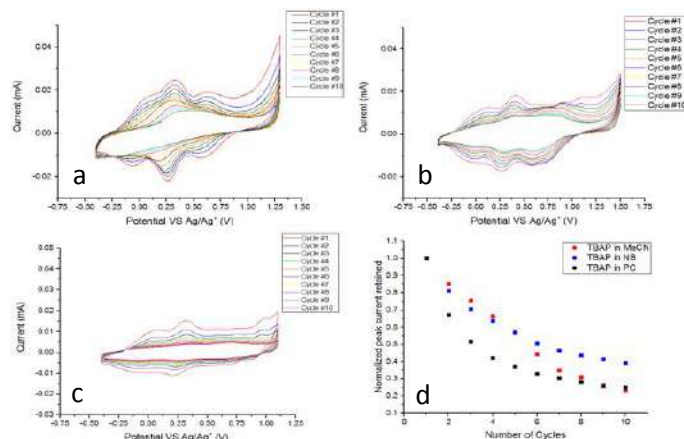


Figure 4. Degradation process test in different solvents like (a) MeCN, (b) NB and (c) PC. The graph (d) is the comparison of the first current peak of each of the first three graphs.

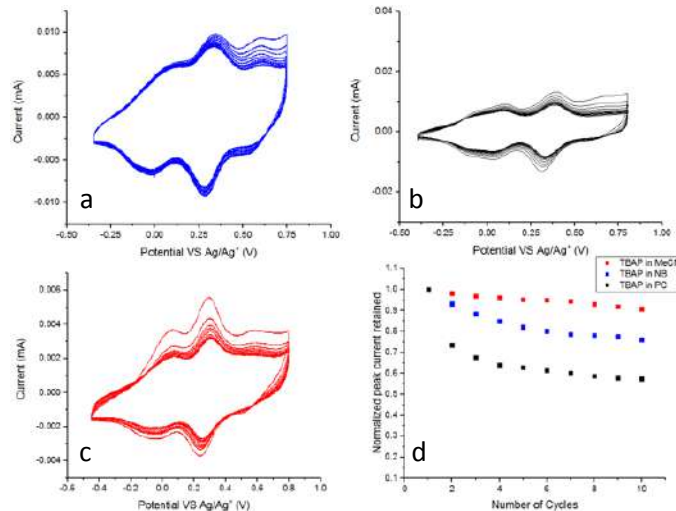


Figure 5. Degradation process test in different solvents only going through the first two peaks. The solutions were (a) MeCN, (b) NB and (c) PC. The graph (d) is the comparison of the first current peak of each of the first three graphs.

Conclusions

Organic materials are promising for electrochemical storage. The most stable performance was observed when cycling only the first two peaks in all solvents. In the case of the two peaks the most stable solvent used was the acetonitrile. Further experiments will be testing the

solubility of the material in different solvents and studying a related polymer featuring a protecting group in hopes of preventing degradation and enabling all three oxidation states to be stably accessed.

Acknowledgments

This project is supported by the Cornell Center for Material Research REU Program. Thanks to this program for the opportunity to be at Cornell University doing research. Thanks to Brian for Fors group in Cornell for the synthesis of the active material and the small molecule. Special thanks to Cara Gannet who has been the person with whom have worked during the summer. Another person who is thanked is Dr. Abruña for allowing to work in his research laboratory with his group.

References

[1] Schon TB, McAllister BT, Li P and Seferos DS. 2016. The rise of organic electrode materials for energy storage. *Chem. Soc. Rev.* 45: 6345-6404.

[2] Godet-Bar T, Lepretre JC, Le Bacq O, Sanchez JY, Deronzier A and Pasturel A. 2015. Electrochemical and ab initio investigations to design a new phenothiazine based organic redox polymeric material for metal-ion battery cathodes. *Phys. Chem. Chem. Phys.* 17: 25283-25296.

[3] Bejan A, Shova S, Damaceanu MD, Simionescu BC, and Marin L. 2016. Structure-Directed Functional Properties of Phenothiazine Brominated Dyes: Morphology and Photophysical and Electrochemical Properties. *Cryst. Growth Des.* 16: 3716–3730.

[4] Elgrishi N, Rountree KJ, McCarthy BD, Rountree ES, Eisenhart T and Dempse JL. 2018. A Practical Beginner's Guide to Cyclic Voltammetry. *J. Chem. Educ.* 95: 197–206.

[5] Nitta N, Wu F, Lee JT and Yushin G. 2015. Li-ion battery materials: present and future. Elsevier Ltd. 18: 1369-7021.

Effect of Glycation Time on Rheological Properties of Collagen Gels for Extrusion Bioprinting

Marcos R. Rodríguez¹, Nicole Diamantides², Lawrence J. Bonassar²

¹Department of Chemical Engineering, University of Puerto Rico – Mayagüez

²Meinig School of Biomedical Engineering, Cornell University

Abstract: Collagen is a promising bioink for extrusion bioprinting due to its inherent biocompatibility and temperature-dependent gelation. The rheological properties of collagen solutions before, during and after gelation dictate their printability and utility however, some collagen gel crosslinking methods introduce cytotoxicity. Previous studies demonstrated that crosslinking through non-enzymatic glycation enhances collagen gel mechanics while maintaining the viability of encapsulated cells. The goal of this study is to determine the effect of glycation time on rheological properties of collagen gels. Results showed that glycation time was non-linear and improved post-gelation storage modulus and gelation rate. Optimal results were seen after 5-7 days of glycation while additional glycation time delayed gelation and decreased mechanical performance.

1. Introduction:

Extrusion bioprinting is the process by which a material (usually a gel) is extruded in a layer by layer method to build 3D constructs. These gels serve as tissue constructs and have a certain degree of geometric complexity. Collagen is a promising bioink for extrusion bioprinting because collagen has a gelation process which develops a branched fiber network, forms the main structural component of the extra-cellular matrix, and has inherent biocompatibility. The rheological properties (i.e., storage modulus, gelation rate, and crossover time) of collagen bioinks before, during and after gelation dictate their printability [3] and utility. Crosslinking methods have been employed to improve the rheological properties of collagen gels however, some of these methods introduce cytotoxicity [3]. Based on previous studies, the non-enzymatic glycation of collagen with ribose enhances collagen gel mechanics while maintaining the viability of encapsulated cells [2]. This is likely due to the formation of advanced glycation end products (AGEs) [2] which crosslink collagen fibers during gelation. We propose the use of this technique to enhance the mechanical properties of collagen bioinks while maintaining cell viability. The goal of this study is to determine the effect of glycation time on the key rheological properties of collagen gels used in bioprinting, including the storage modulus before and after gelation, crossover time and gelation rate of the collagen gels with the purpose of identifying an optimal glycation period.

2. Materials and Methods:

2.1 Collagen Bioink Formulation

Type I collagen was extracted from rat tails and solubilized in 0.1 % acetic acid at 150 mL/g [3]. The collagen solution was then centrifuged at 9000 rpm for 90 minutes at 4 °C [3]. The supernatant was collected, frozen overnight at -80 °C and lyophilized for 5 days.

Lyophilized collagen was reconstituted in 0.1 % acetic acid at 15 mg/mL. Stock collagen was mixed with a 250 mM ribose solution to induce glycation and stored at 4 °C for 5, 7, 9, 14 or 21 days.

2.2 Rheological Characterization

The solution was tested with a TA Instruments DHR3 rheometer using a 25 mm parallel plate geometry. For this process the collagen-ribose solution was neutralized with a working solution containing 1X PBS, 10X PBS and NaOH [1], transferred to the base of the plates, and examined in oscillatory mode at 0.1 Hz with a 0.5 % strain and 1 mm gap for 5 minutes at 4 °C followed by 30 minutes at 37 °C wherein gelation occurs [2]. Glass coverslips previously treated with polyethylenimine (PEI) and glutaraldehyde were attached to the rheometer's plates to prevent the gels from slipping during testing [3]. The mean storage modulus at 4 °C (before gelation) and 37 °C (after gelation), the gelation rate and the crossover time were acquired.

3. Results:

Glycation with ribose lowered pre-gelation storage modulus (Figure 1A) and delayed gelation time (Figure 1D) when compared to control runs (no-ribose) which exhibited 1.3 ± 0.2 Pa and 1.9 ± 0.1 minutes respectively. The 7 day glycation gels showed the largest pre-gelation storage modulus of the glycation periods with 1.1 ± 0.2 Pa (Figure 1A) and the shortest crossover time with 3.2 ± 0.4 minutes (Figure 1D). The 7 day glycation period along with the 5 day exhibited the largest post-gelation storage modulus (Figure 1B) with 3668.0 ± 317.2 Pa and 3713.0 Pa, respectively. The 7 day samples also resulted with the highest gelation rate (Figure 1C) with 27.9 ± 1.4 Pa/s. Glycation time after 9, 14 and 21 days decreased storage modulus before and after gelation. These glycation

periods also reported the slowest gelation rate and crossover time.

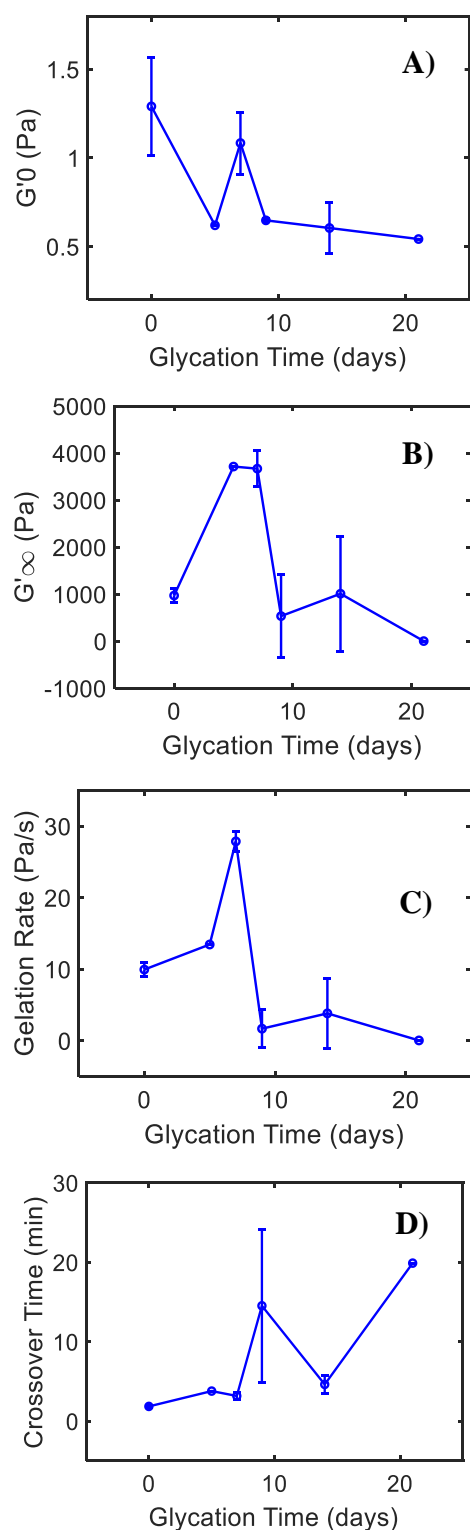


Figure 1. Rheology tests results showing rheological properties of collagen solutions such as a) pre-gelation storage modulus, b) post-gelation storage modulus, c) gelation rate and d) crossover time as a function of glycation time. Results represent averages

and standard deviation (error bars) of the tests within each glycation time.

4. Discussion:

The effect of glycation time was non-linear, with optimal results seen after 5-7 days, while additional glycation time delayed gelation and decreased mechanical performance. Glycation introduces two competing factors into the collagen gel, the intermediaries formed during the glycation process (i.e., ribose, Schiff base, Amadori product, etc.) and AGEs. The intermediaries likely increase the solubility of the collagen which lowers the viscosity and hinders gelation. This is a deterrent for the gelation phenomena and is most likely responsible for delayed gelation and worsening pre-gelation storage modulus. Meanwhile, the AGEs aid the crosslinking of the collagen during gelation and is most likely responsible for the increase in post-gelation storage modulus and gelation rate for 5 and 7 day glycation times in comparison to the control runs.

5. Conclusions:

Glycation improved the post-gelation storage modulus and gelation rate due to formation of AGEs and subsequent crosslinking. The effect of glycation time was non-linear, with optimal results seen after 5-7 days, while additional glycation time delayed gelation and decreased mechanical performance.

6. Acknowledgements:

This work was supported by CCMR with funding by the NSF MRSEC program (DMR-1719875) and REU Site program (DMR-1063059).

7. References:

- [1] Rhee, S., ACS Biomater. Sci. Eng., 2016, 2, 1800-1805
- [2] Roy, R., J. Orthop. Res., 2008, 26, 1434-1439.
- [3] Diamantides, N., Biofabrication, 2017, 9, 03410

Synthesis and Purification of Antimicrobial Oligothioetheramides

Mathias Rodriguez

Abstract – *As resistance to traditional antibiotics becomes a growing concern, new antibiotics will need to be developed that offer alternative treatment methods and routes.*

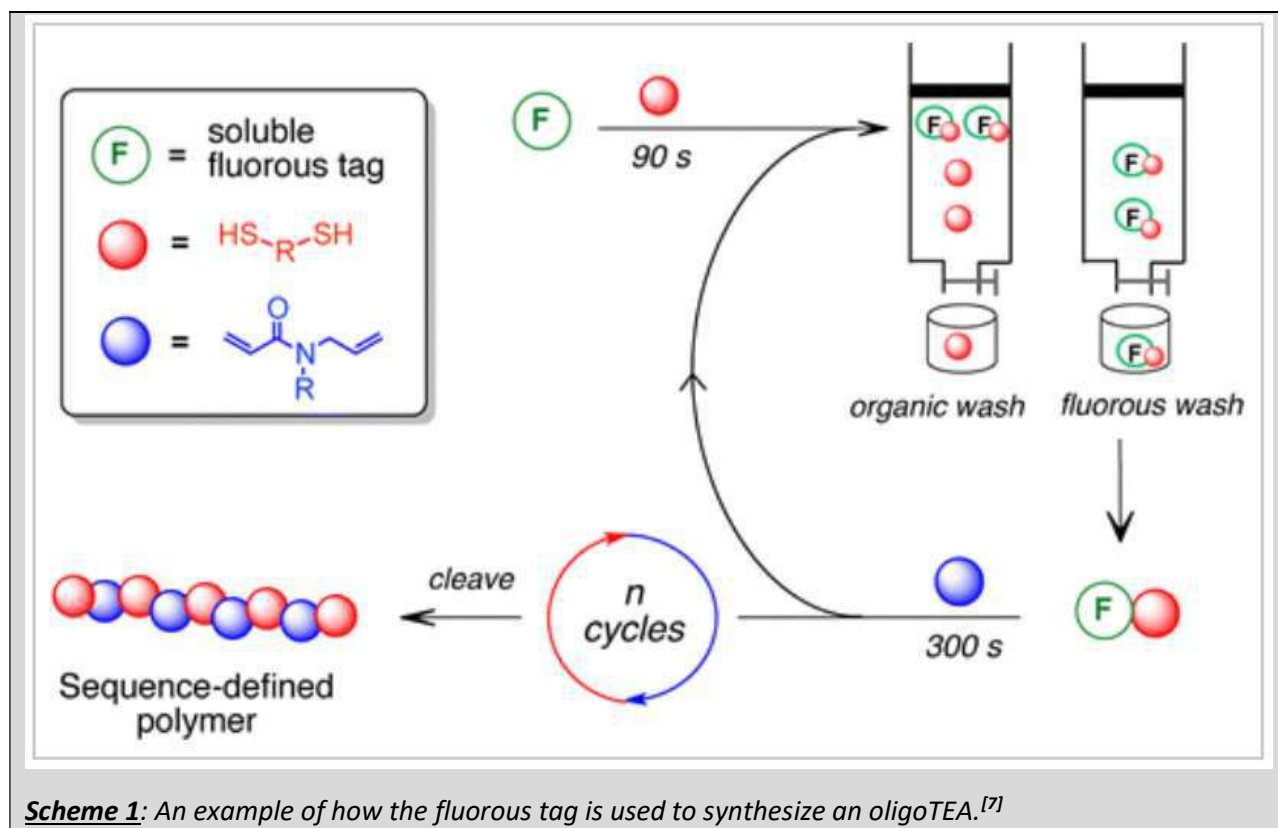
Oligothioetheramides (oligoTEAs) are a new class of oligomers that can be modified to mimic the antibiotic characteristics of antimicrobial peptides. In the synthesis of these oligoTEAs, there are several side products that are generated, which negatively impact the yield of the intended product. Traditionally, purification was performed using fluorous solid phase extraction (FSPE). However, this purification process would decrease the effective yield of oligoTEA synthesis with each successive coupling step – quite notably on the last step. To improve synthesis yield and scalability, a different purification protocol was developed. This new purification protocol utilized sodium hydroxide as the aqueous layer, and dichloromethane (DCM) as the organic layer. Excess 1,3-propanedithiol was deprotonated with NaOH, and successfully removed from the organic layer after a thiol-ene reaction. Excess guanidine monomer was reacted with 3-mercaptopropionic acid (MPA) to form a polar, hydrophilic molecule that would theoretically migrate into the aqueous layer. While the MPA reacted with guanidine monomer, the solution formed an emulsion that could not be removed with brine or sodium bicarbonate. The extraction after the Michael addition will need to be repeated to determine whether the protocol will need to be altered.

Introduction

Over the past several decades, there have been troubling developments in antibiotic resistance as the lifespan of antibiotic medications are being shortened due to bacteria rapidly evolving to resist such treatments. These challenges are due to several factors, such as insufficient drug discovery by the pharmaceutical industry^[1], mismanagement of prescriptions^[2], and regulatory concerns^[3].

Research into antimicrobial peptides (AMPs) has been one method developed to address antibiotic resistance. AMPs are molecules that are naturally produced by the immune system to combat foreign bacteria^[4]. While there has been success with AMPs as a new class of antibiotics, there are concerns with regards to proteolytic degradation, serum binding protein sequestration, and cell toxicity^[5]. However, some such concerns can be addressed by new classes of sequence-defined AMP mimetics such as oligothioetheramides (oligoTEAs).

A critical component of oligoTEA synthesis is a soluble fluorous support (fluorous tag) that is found at the beginning of the peptide. The fluorous tag is a perfluorocarbon alkyl chain that is soluble in many organic solvents, but can be attached to a fluorous solid phase silica column.^[6] The purpose of the fluorous tag is to be able to separate the synthesized oligomer with a fluorous tag from the excess reactants and catalysts during an extraction.



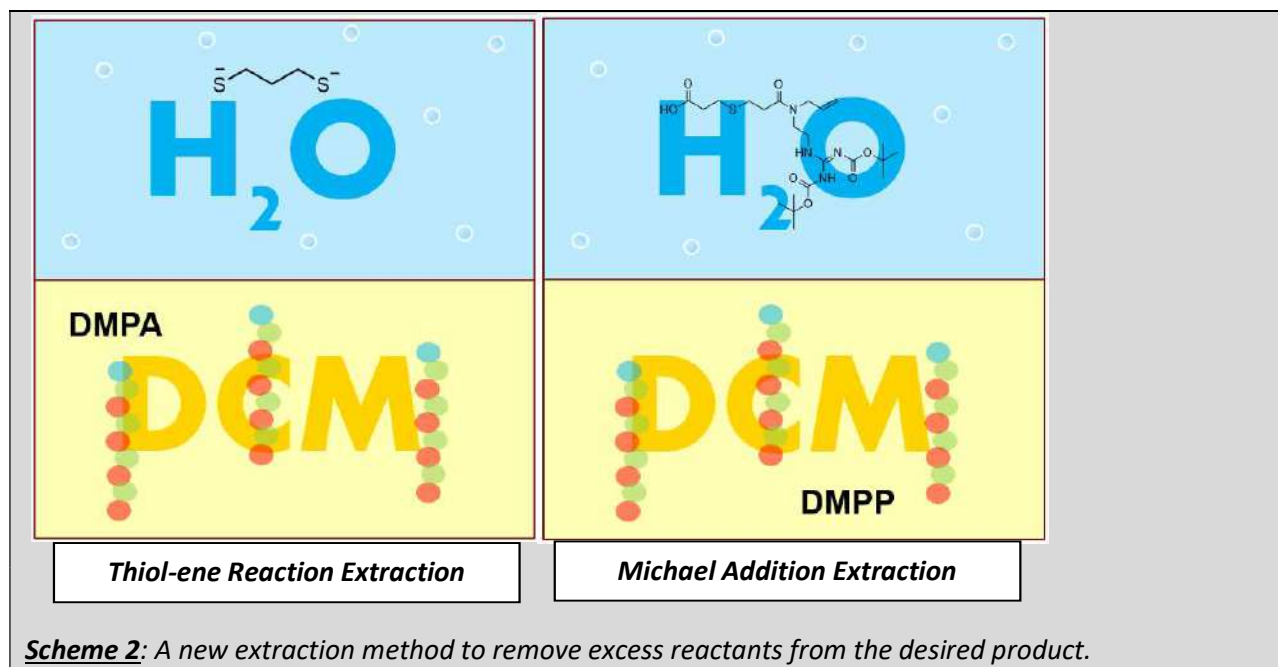
Scheme 1: An example of how the fluororous tag is used to synthesize an oligoTEA.^[7]

The oligomer with a fluororous tag will remain attached to the fluororous solid phase silica column on the fluororous stationary phase while everything else will be washed away during the purification process. The oligomer with a fluororous tag can then be removed from the fluororous silica stationary phase with a different eluent protocol after all undesired organic materials are washed away. The key advantages of performing FSPE involve “homogenous reaction conditions, fast solution phase kinetics, and reaction monitoring via common spectroscopic techniques”.^[6]

While there are benefits of using a fluororous tag support to demonstrate a proof-of-concept design for oligoTEAs, its advantages do not lend well when attempting to scale up synthesis. Common issues include low yields over multiple purification steps, long purification times per step, lack of scalability beyond the size of the column, and time spent removing water and methanol from the product (water is known to interfere with the coupling of dithiol monomers). Additionally, there would significant cost savings due to no longer needing to use a fluororous tag, which is priced at \$80 per 2 g.

An alternative solution to using a fluororous tag support is performing liquid-liquid phase extractions. This addresses the limitations of solid fluororous phase extraction by shortening the duration of each purification step, increasing the scalability, and reducing the time to remove solvents after purification. While the oligomer would remain in the DCM organic layer, the excess reactants would be separated into the aqueous layer. Using a basic aqueous solution such as NaOH would deprotonate the dithiol used in the thiol-ene reaction, allowing it to move into the aqueous layer. After the Michael addition, the excess guanidine monomer would be

recreated with a highly polar thiol, forming a molecule that would migrate into the aqueous layer as well.



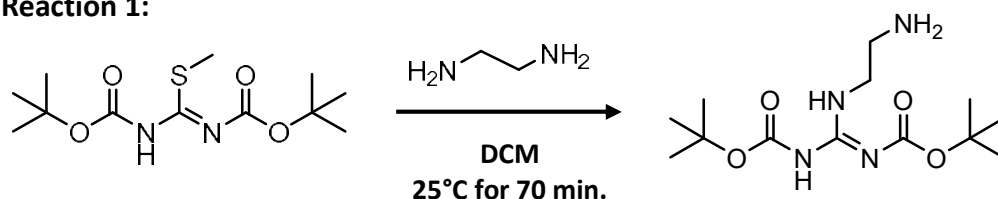
Methods

Synthesis of the Fluorous BOC-Protected Allyl Amine

One equivalency of fluorous BOC-ON (with a perfluorocarbon alkyl chain of C₈F₁₇), 1.6 equivalents of allyl amine, and 2.5 equivalents of triethylamine were combined in 10 mL of tetrahydrofuran (THF). The solution was stirred at room temperature overnight. Solvent was removed at reduced pressure. The product was dissolved in methanol, purified using fluorous solid phase extraction, and then verified using nuclear magnetic resonance (NMR)

Synthesis of Guanidine Monomer

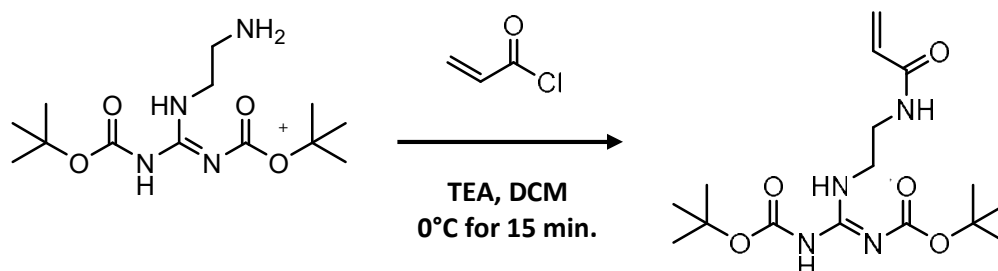
Reaction 1:



One equivalency of 1,3-Di-boc-2-methylisothiourea was combined with 2.5 equivalents of ethylenediamine in DCM to form a concentration of 250 mM for 1,3-Di-boc-2-methylisothiourea. This solution was stirred at 25°C for 70 minutes. The organic solution was purified using liquid-liquid phase extraction – it was washed 3x with water, 1x with brine, and

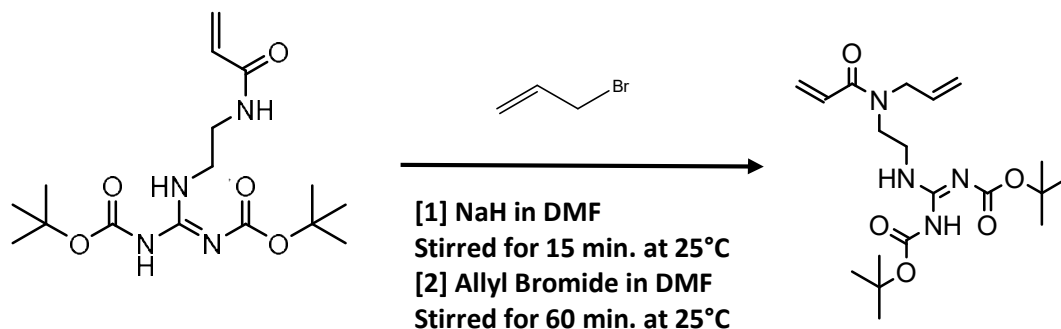
excess water was removed with anhydrous sodium sulfate. DCM was removed using a rotary evaporator.

Reaction 2:



The product from **Reaction 1** was solubilized with DCM to create a reaction concentration of 150 mM, and 1.5 equivalents of triethylamine (“TEA”) was added. The reaction was stirred at 0°C for 15 minutes, and then 1.5 equivalents of acryloyl chloride solubilized in 3 mL DCM was added dropwise into the reaction at 0°C for 20 minutes. The reaction was stirred at 0°C for 60 minutes, and then stirred at 25°C for 60 minutes. The reaction was then quenched with water. The solution was purified using liquid-liquid phase extraction – it was extracted 3x with DCM, and the combined organic layers were washed 1x with brine and dried with anhydrous sodium sulfate. The remaining DCM in the organic layer was removed by rotary evaporator to yield the desired product.

Reaction 3:



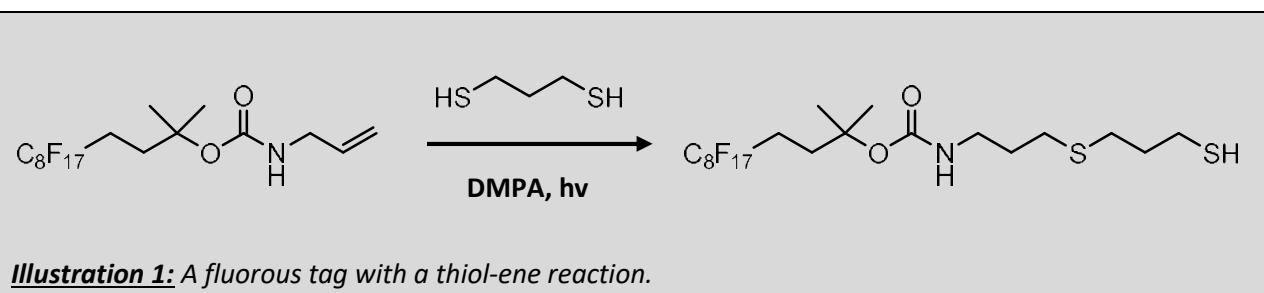
The product from **Reaction 2** was weighed to determine how much dry dimethylformamide (“DMF”) would be needed to create a reaction concentration of 200 mM. One-third of the required DMF was used to solubilize 4 equivalents of sodium hydride (“NaH”). Another one-third of the required DMF was used to solubilize the product from **Reaction 2**. The solubilized NaH was added to the solubilized product from **Reaction 2** and stirred at 25°C for 15 minutes. The remaining one-third of required DMF was used to solubilize 2.5 equivalents of allyl bromide, which was added dropwise at 25°C for 10 minutes. The reaction mixture was stirred at 25°C for 60 minutes, and then quenched with water. The solution was purified using liquid-liquid phase extraction – it was extracted 3x with diethyl ether, and the combined ether layers

were washed 1x with brine and dried with anhydrous sodium sulfate. The remaining diethyl ether in the organic layer was removed by rotary evaporator. The final product, guanidine monomer, was purified using silica column flash chromatography on a gradient of 0-100% ethyl acetate in hexanes.

Synthesis and Purification of OligoTEAs

The synthesis of oligoTEAs was performed by subsequent thiol-ene reactions and Michael additions on a fluororous tag. The product was purified by extraction after each reaction. The synthesis of oligoTEAs was performed on a 10 – 30 mg scale of fluororous tag.

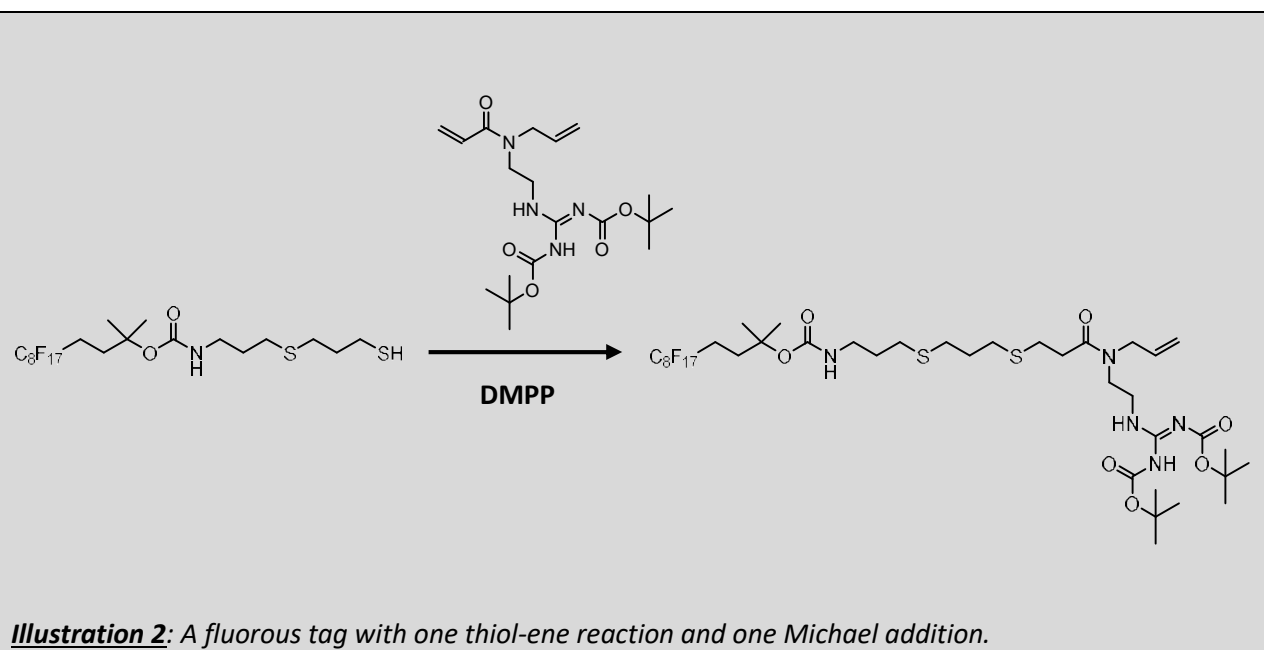
Thiol-ene Reaction: One equivalency of fluororous tag was solubilized in methanol (“MeOH”) so that the reaction concentration would be 150 mM. Then, 5 equivalents of 1,3-propanedithiol (“PDT”) and 0.25 equivalents of 2,2-dimethoxy-2-phenylacetophenone (“DMPA”) were added. The reaction was then exposed to three 90-second intervals of ultraviolet light. This created a fluororous tag with a dithiol attached (“FT-T1”).



Purification After Thiol-ene Reaction: The FT-T1 product was dried down to remove MeOH, and it was resolubilized in 1 mL DCM. The excess PDT would need to be deprotonated by a base so that the negatively charged excess PDT would move into the aqueous layer. Based upon troubleshooting, the ideal extraction would involve a 1:1 equivalency of 100 mM NaOH to DCM. Thin layer chromatography (“TLC”) was utilized to readily identify whether was a significant amount of PDT remaining in the organic layer. The mobile phase was 100% MeOH, and potassium permanganate was used as the staining agent. Given the relative polarity of the fluororous tag and guanidine monomer as compared to PDT, identification of each component on a stained TLC plate using 100% MeOH were the best parameters (**Figure 4[A]**). Solvents such as hexane, ethyl acetate, and DCM kept the comparison of fluororous tag, PDT, and product dots close together with not enough separation to discern whether the product contained PDT (**Figure 4[B]**).

Michael Addition Reaction: The thiol-ene reaction was assumed to yield 100% of the theoretical product – This became the new basis for equivalency. Two equivalents of guanidine

monomer and 0.1 equivalents of dimethylphenylphosphine (DMPP) were added to the thiol-ene reaction product and solubilized in methanol to have a reaction concentration of 100 mM. The reaction was stirred at 40°C for one hour. The completion of the Michael addition reaction was confirmed via a 2,2'-dithiodipyridine (DTDP) assay. The DTDP assay measures the extent to which there are primary thiols in a sample. The DTDP assay was performed using 150 μL of 0.1% TEA in dimethyl sulfoxide, 2.5 μL of 12 mM 2,2'-Dithiodipyridine in DMSO, and 1 μL of the sample or blank was combined and mixed for 5 minutes. The blank was MeOH. Next, 5 μL of glacial acetic acid was added to both the sample and blank, and mixed for 5 minutes. Finally, a DTDP assay was performed. The resulting product was a fluororous tag with both one thiol-ene reaction and one Michael Addition reaction ("FT-T1M1").



Purification after Michael Addition Reaction: The Michael Addition reaction was dried down to remove MeOH and resolubilized in 1 mL DCM. To remove the excess guanidine monomer, the solution was reacted with 3-mercaptopropionic acid ("MPA") so that the combined product MPA and guanidine monomer ("MPA-GM") would be a hydrophilic molecule that would move into the aqueous phase. Since there was still DMPP catalyst in the product solution, the MPA and guanidine monomer would undergo a Michael Addition reaction as well.

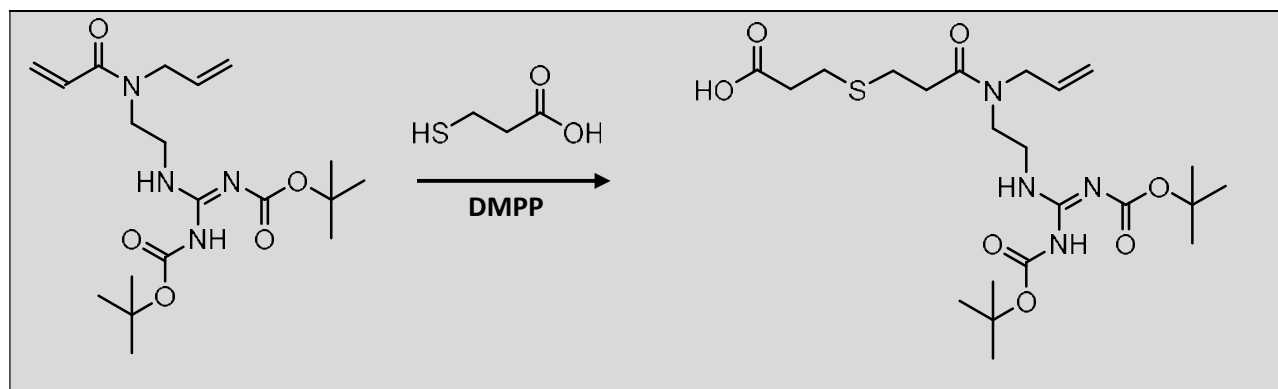


Illustration 3: Reacting guanidine monomer with MPA to form a hydrophilic molecule.

Results / Discussion

Reactant and OligoTEA Synthesis

The fluorous tag was synthesized and verified via nuclear magnetic resonance (NMR) (**Figure 1**). Guanidine monomer was synthesized and verified using NMR (**Figure 2**) and Liquid Chromatography - Mass Spectrometry ("LCMS") (**Figure 3**). A thiol-ene reaction and Michael addition were performed, respectively, to a fluorous tag. The completion of the Michael addition was verified using a DTDP assay (**Figure 4**).

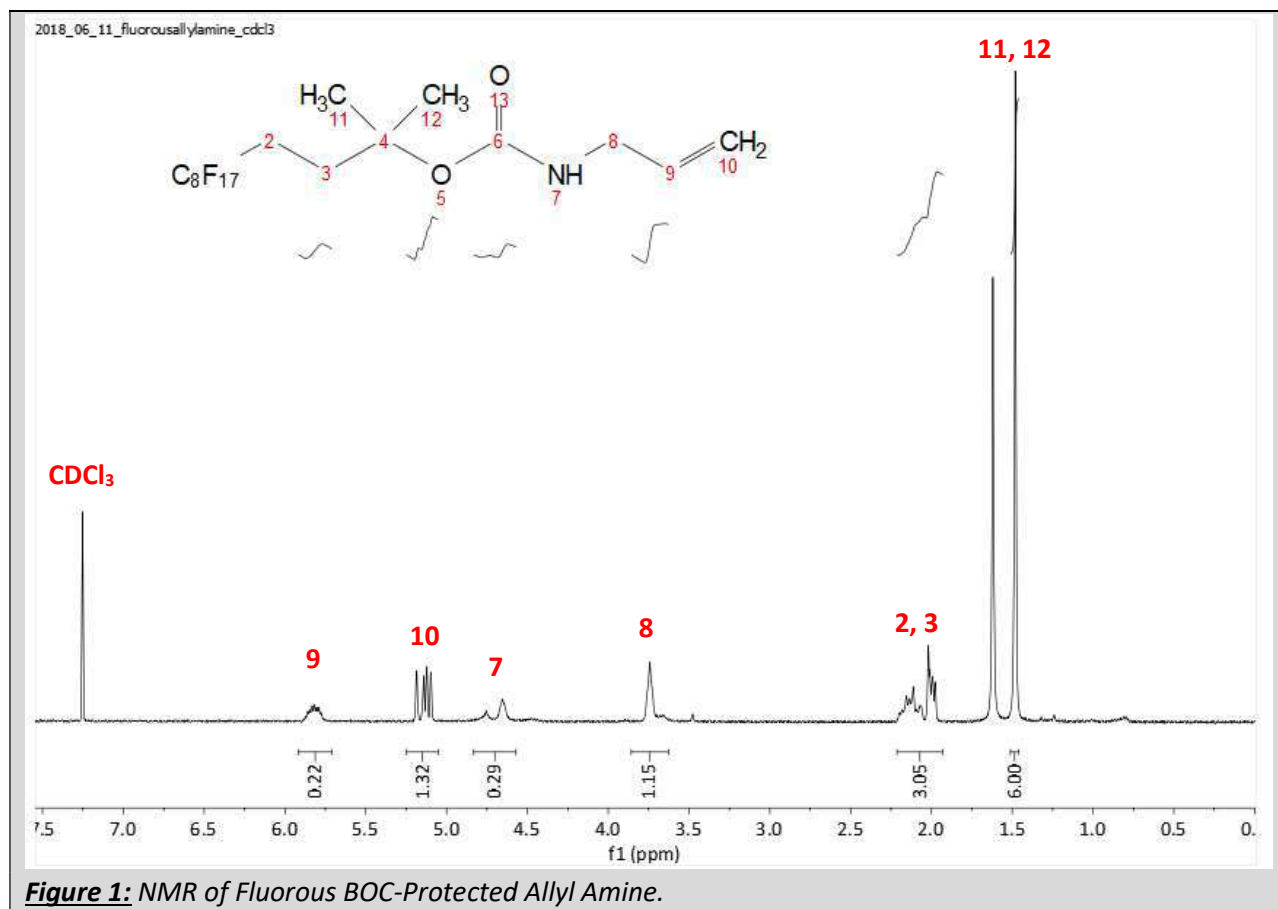
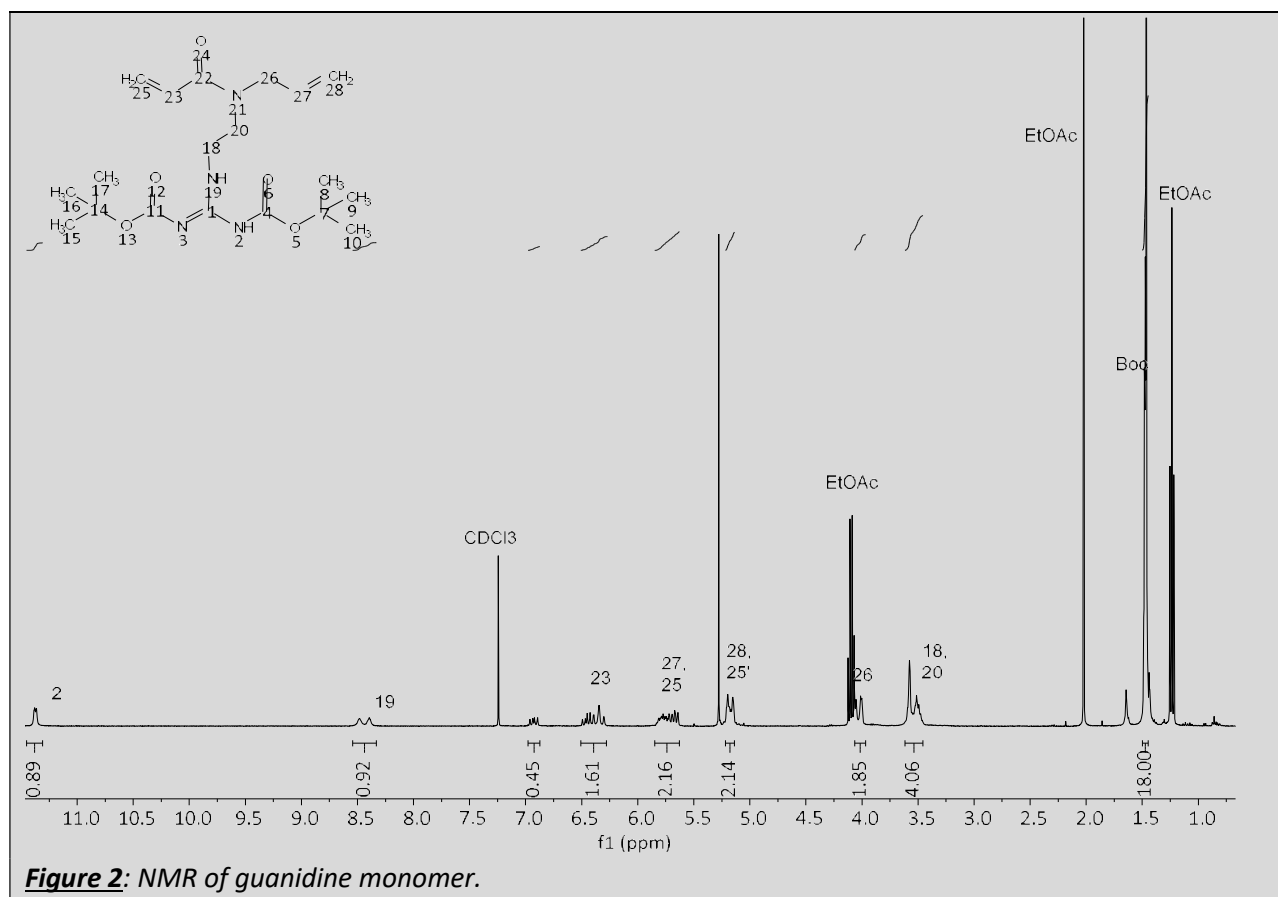
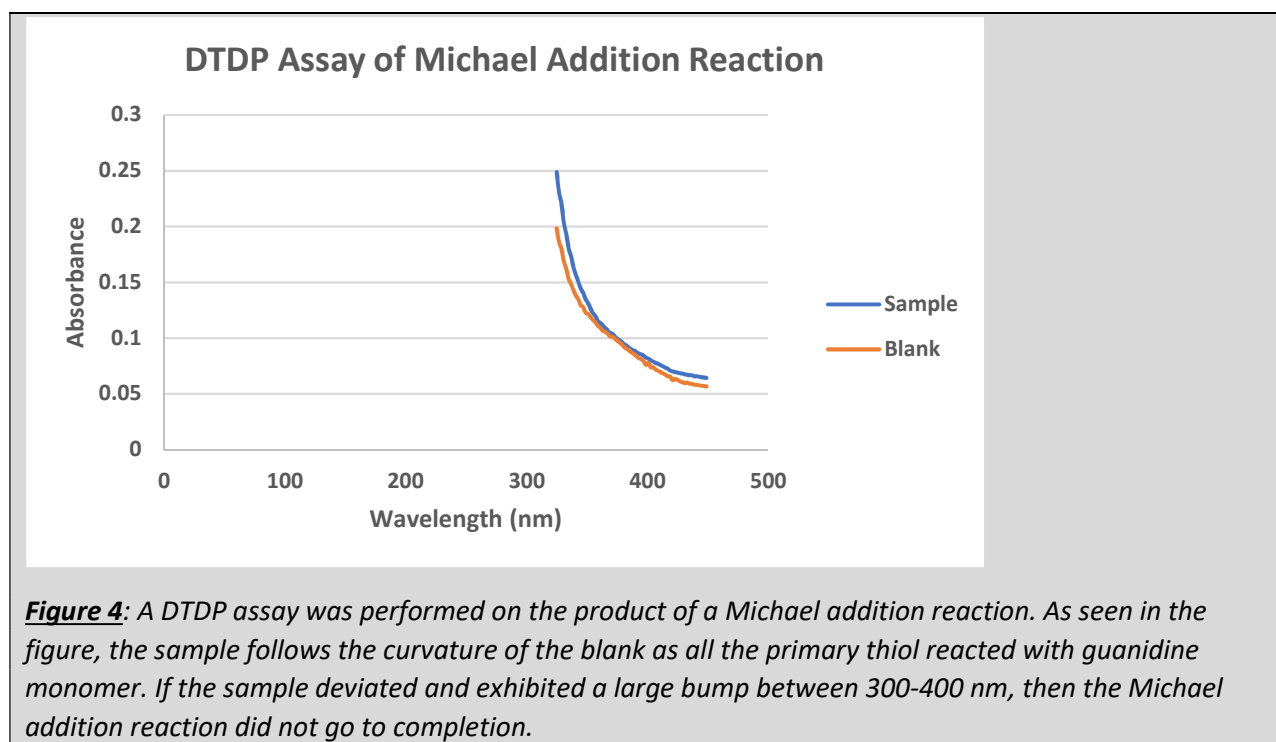
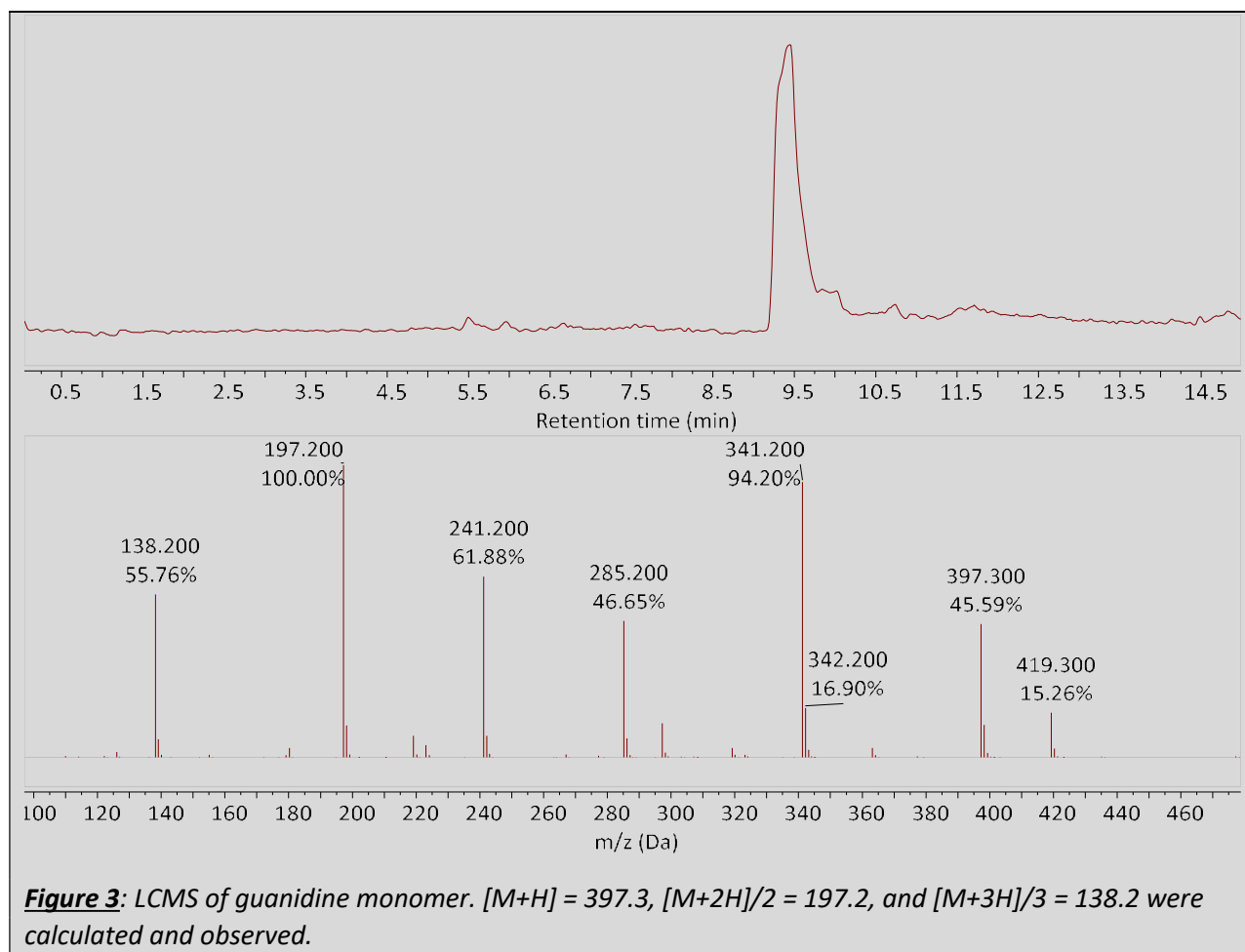


Figure 1: NMR of Fluorous BOC-Protected Allyl Amine.





Extraction after Thiol-ene Reaction

After five washes at a lower concentration of 10 mM NaOH, a distinguishable amount of PDT remained in the organic layer (**Figure 4[C]**). After two washes of 100 mM NaOH, thin layer chromatography showed that there was no remaining PDT in the organic layer (**Figure 4[D]**). For extractions performed onward, five washes with 100 mM NaOH were used to ensure the complete removal of PDT from the organic layer.

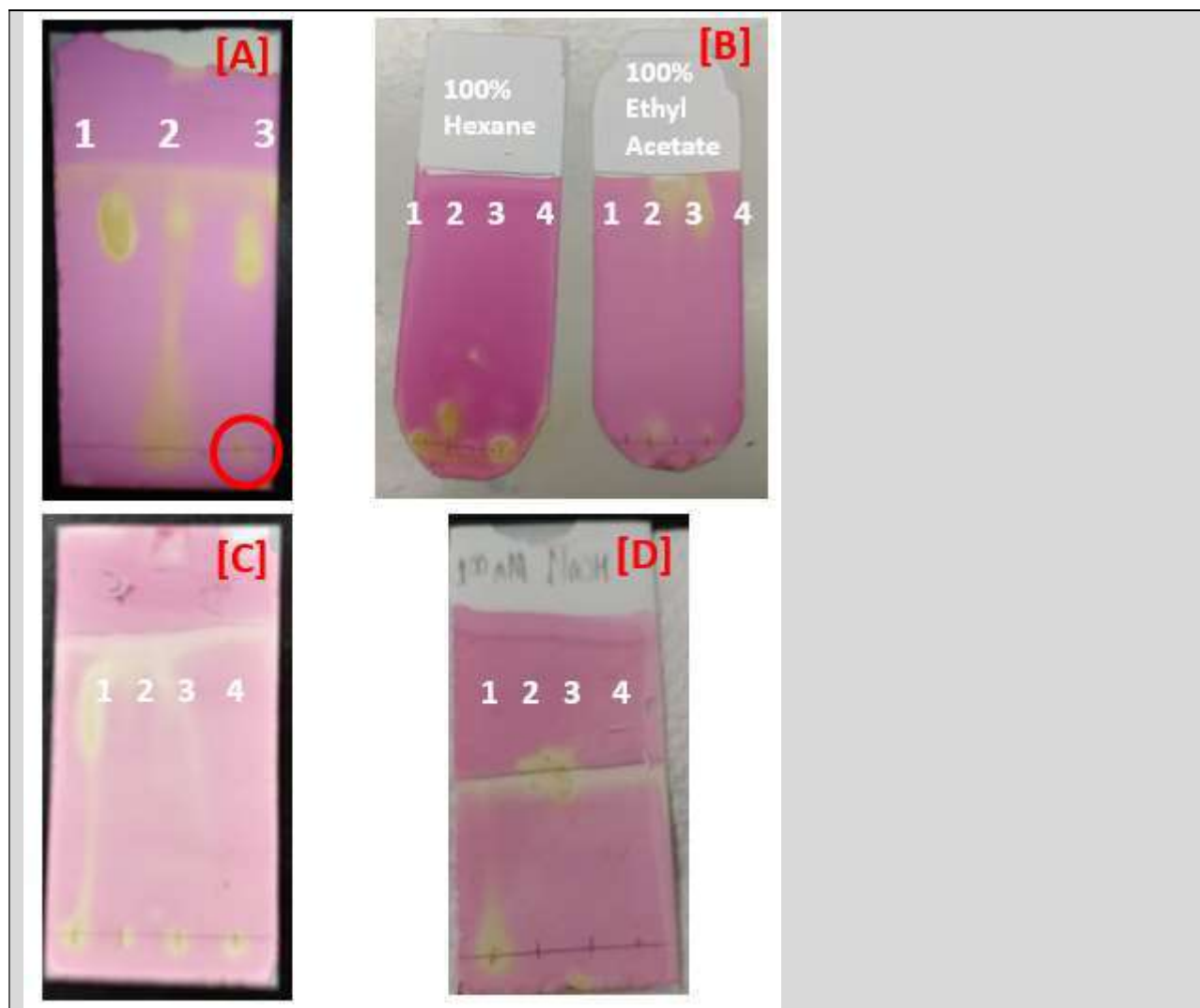


Figure 4: Fluororous tag spots were dabbed three times with a 10 mg per 10 mL stock solution. PDT spots were dabbed one time with a 0.1 mg per 10 mL stock solution. DMPA spots were dabbed three times with a 10 mg per 10 mL stock solution. FT-T1 spots, unless otherwise noted, were dabbed three times. **[A]:** TLC was performed on an organic layer after five washes of 100 mM NaOH. 1 is fluororous tag, 2 is PDT, and 3 is FT-T1. Excess PDT exhibits a conspicuously large streak that extends the length of the mobile phase, allowing for a straightforward identification of its presence. The FT-T1 dot on 3 was dabbed 10 times to see if there was any remaining PDT in the product, which can be observed at the beginning of the mobile phase as circled in red. **[B]:** TLC was performed on a purified thiol-ene reaction using fluororous solid phase extraction. 1 is fluororous tag, 2 is PDT, 3 is DMPA, and 4 is FT-T1. The left TLC plate was made using 100% hexane as the mobile phase, and the right TLC plate was made using 100% ethyl acetate as the mobile phase. In both cases, there was not enough vertical separation between each

dot when compared side-by-side. **[C]**: TLC was performed on an organic layer of a thiol-ene reaction with 10 mM NaOH. 1 is the product before any washes, 2 is the product after one wash, 3 is the product after three washes, and 4 is the product after five washes. Each dot was dabbed three times. PDT remained after five washes, so the aqueous layer was replaced with 100 mM NaOH. **[D]**: TLC was performed on an organic layer of a thiol-ene reaction with 100 mM NaOH. 1 is the product after one wash, 2 is the product after two washes, 3 is the product after three washes, and 4 is the product after four washes. Each dot was dabbed three times. There was no noticeable amount of PDT at the beginning of the mobile phase after two washes, but five washes were performed for the reactions to ensure that all PDT was removed.

Extraction after Michael Addition

A kinetics study was done using 1, 1.5, 2, and 4 equivalencies of MPA relative to unreacted guanidine monomer, and samples were analyzed using LCMS at timepoints 0, 15, 30, 45, 60, 75, and 90 minutes. This was performed to identify the ideal amount of MPA to react with all the unreacted guanidine monomer from the Michael addition.

There were two goals that this reaction needed to accomplish: [1] React all the excess guanidine monomer with MPA so that there is no remaining unreacted guanidine monomer in solution; and [2] ensure that the conditions of the reaction do not allow the MPA to react with FT-T1M1 so that the oligomer is “capped” with MPA on the product’s allyl group of the guanidine monomer – This would terminate the oligomer’s ability to grow.

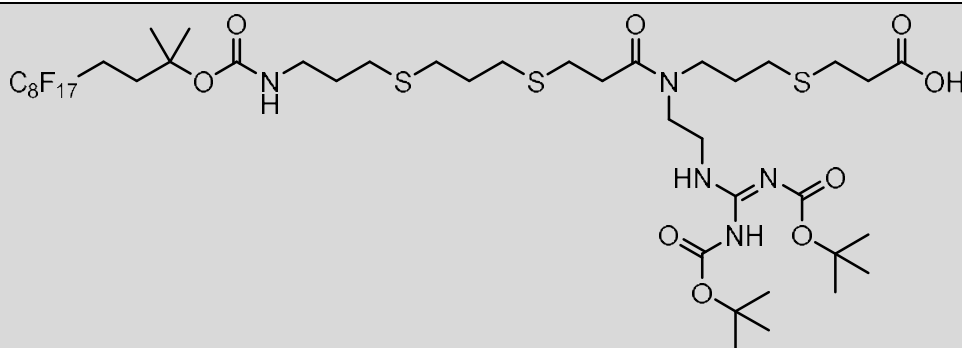
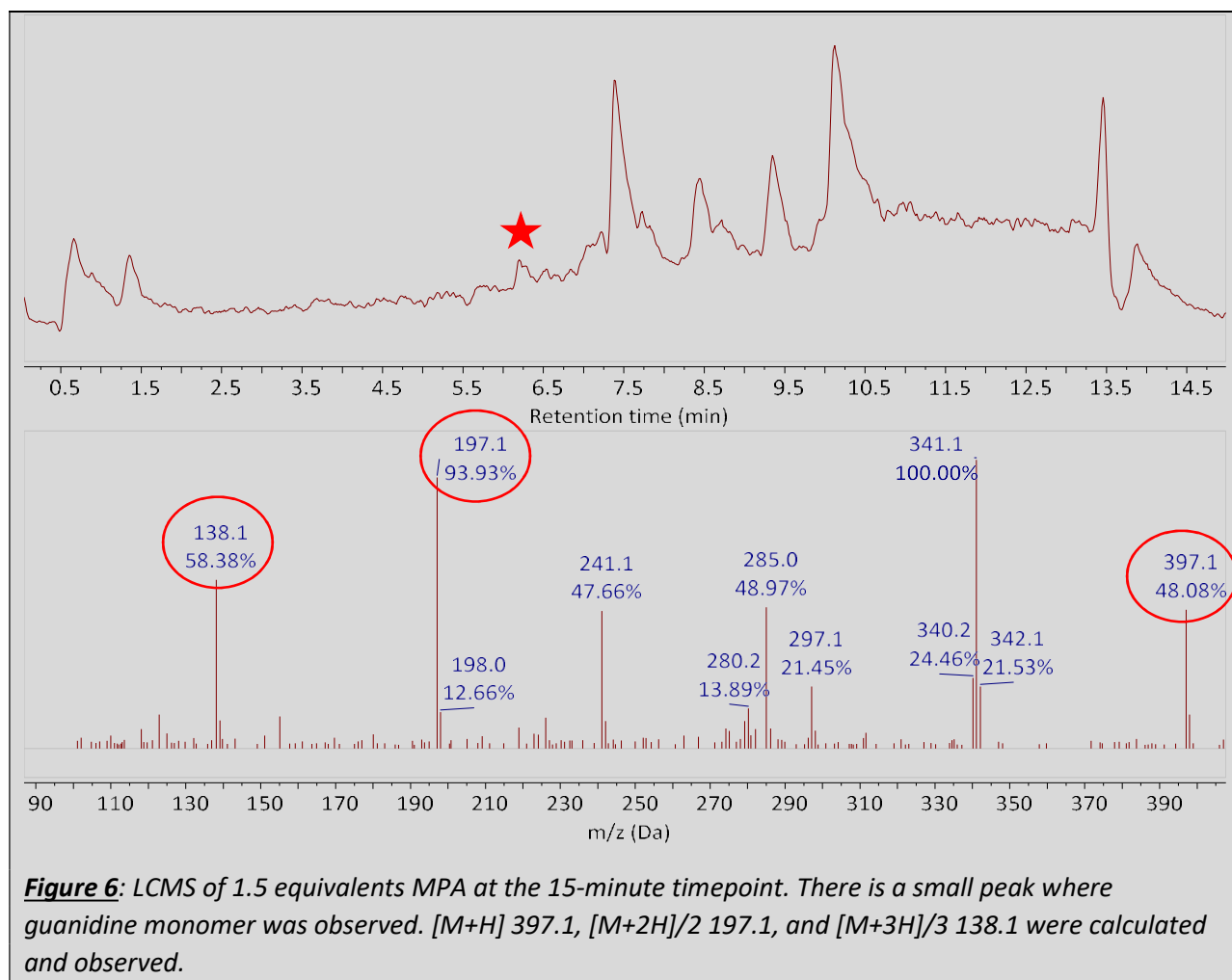
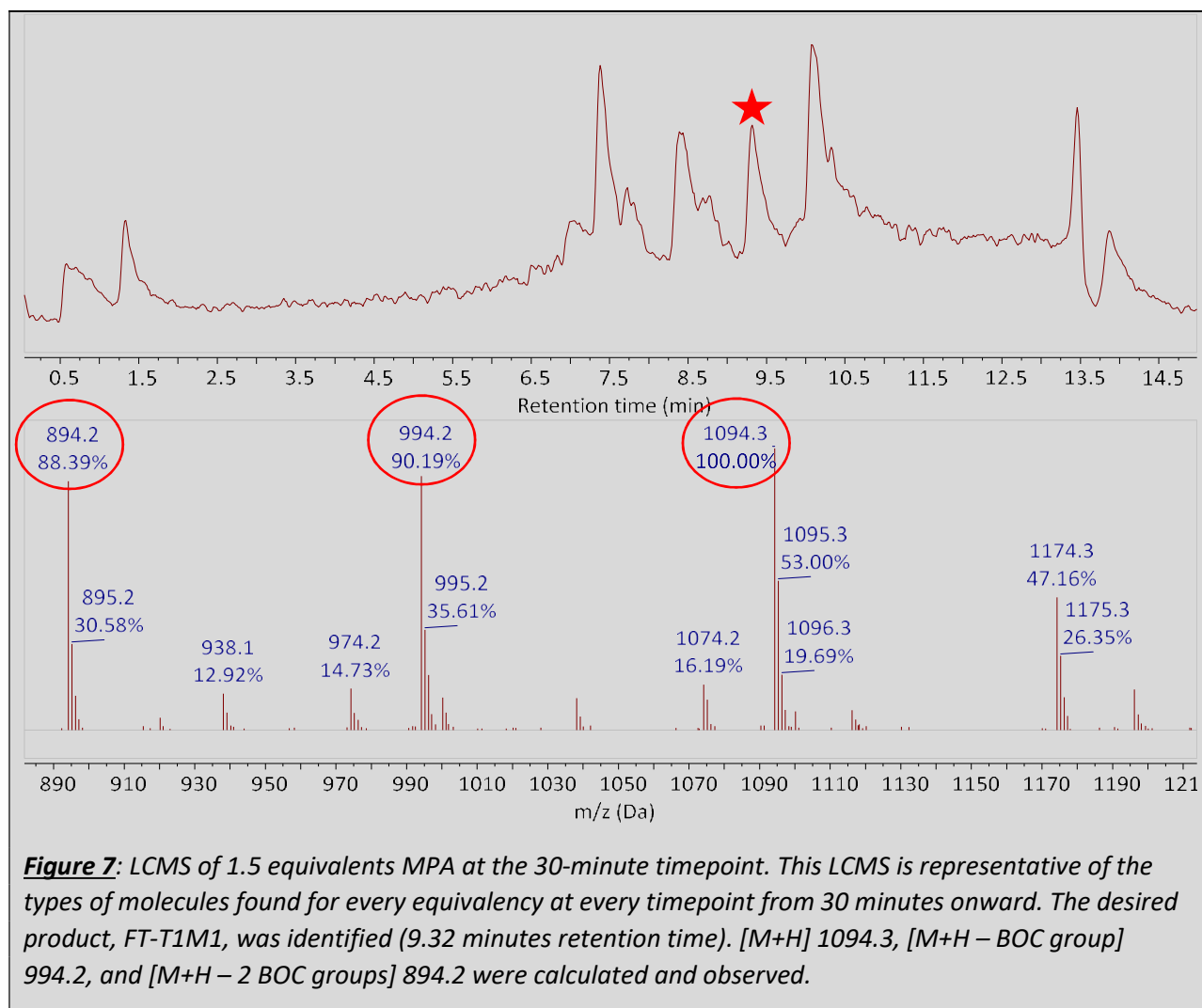
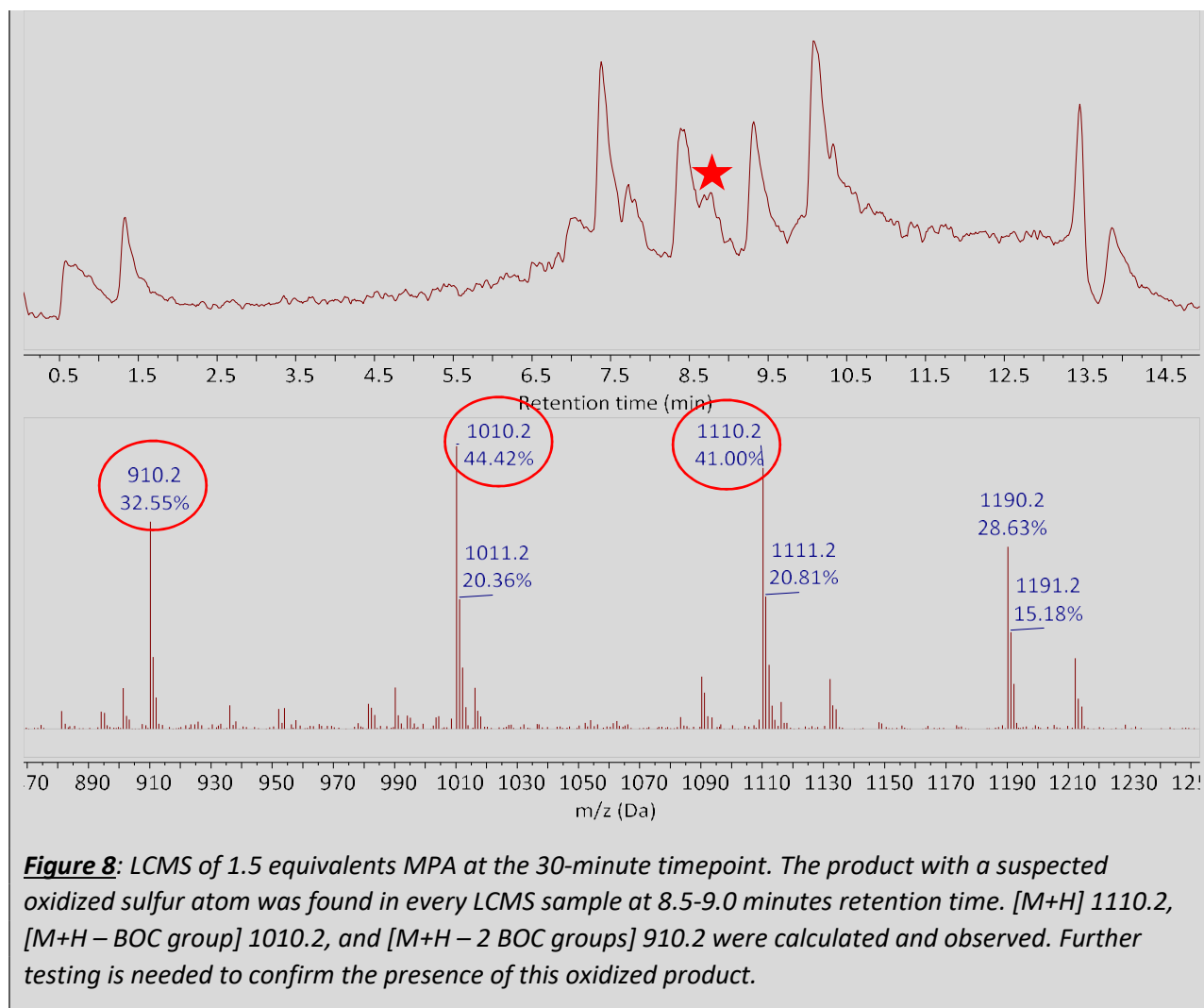


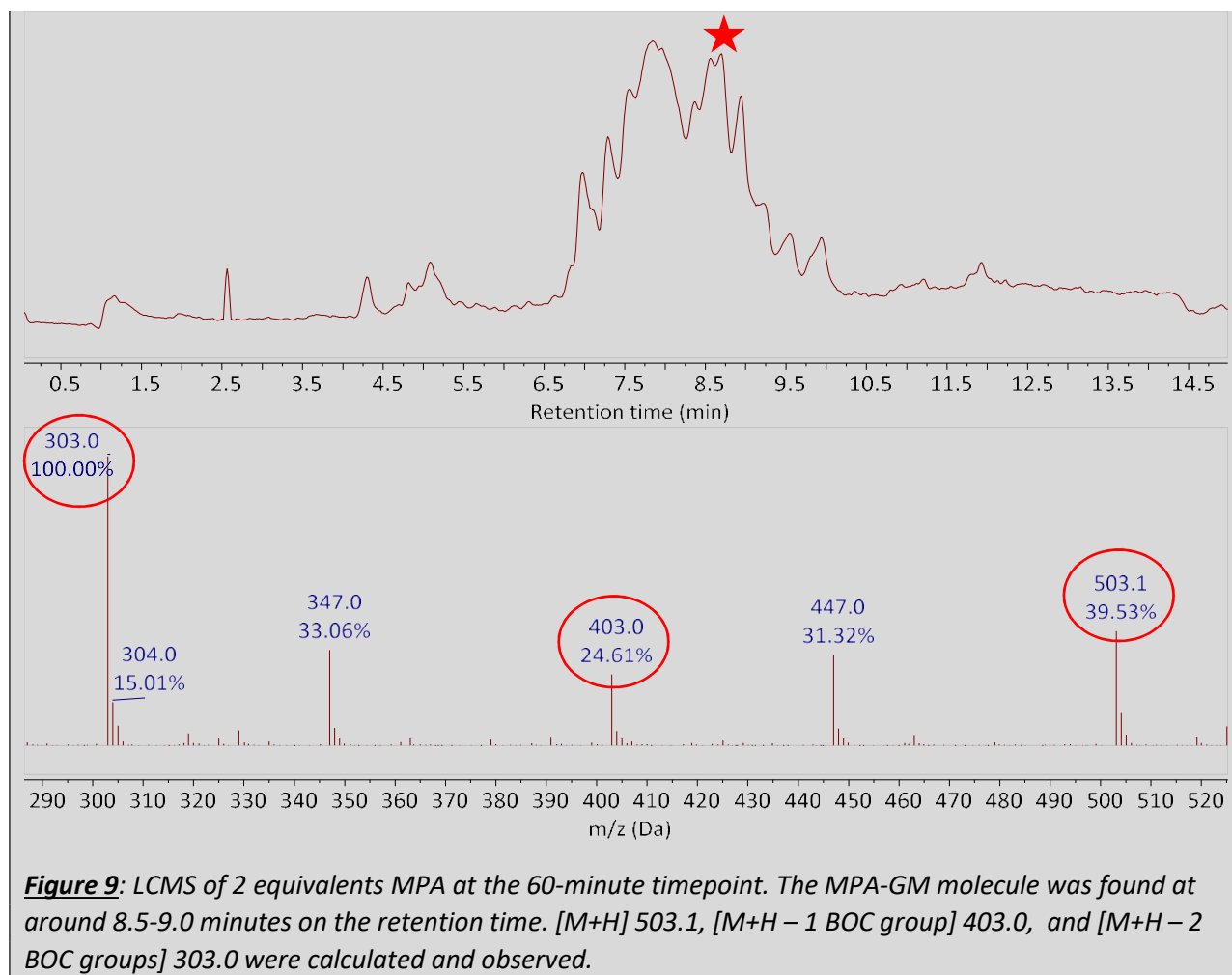
Illustration 4: The FT-T1M1 product that reacted with MPA, disabling its ability to grow.

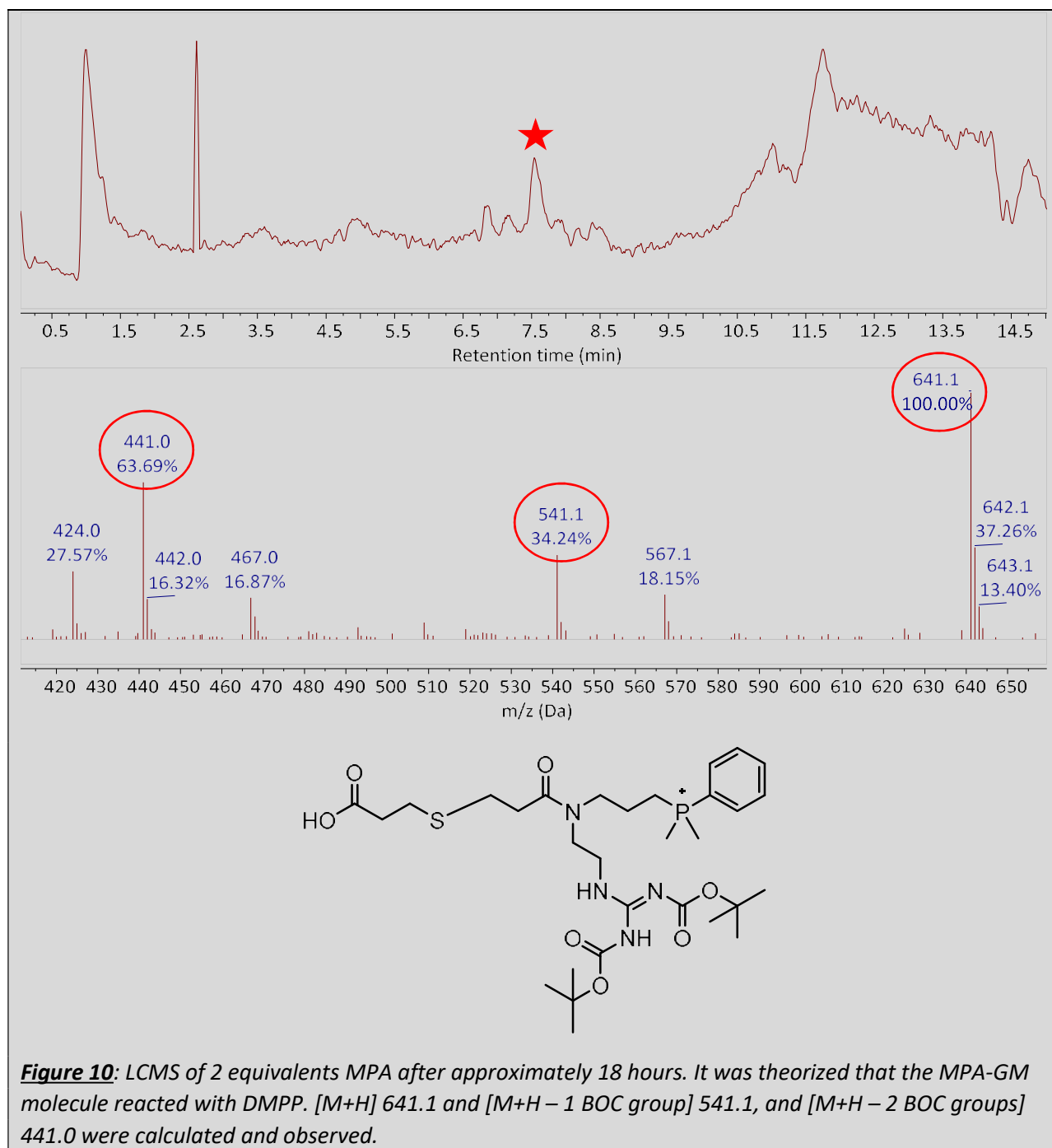
Guanidine monomer was not detected by LCMS analyses after the 30-minute time interval for all conditions tested. At the 15-minute mark for each equivalency, a small peak indicated the presence of guanidine monomer (**Figure 6**). None of the equivalencies at any timepoint yielded a “capped” FT-T1M1 product with MPA attached to the allyl group of the guanidine monomer at the end of the oligomer. The desired FT-T1M1 product was observed and confirmed with LCMS at all timepoints (**Figure 7**). However, there was another product created with a mass of 1100.3, which is suspected to be the FT-T1M1 product with one of its sulfur atom oxidized (**Figure 8**). The MPA-GM molecule was observed and identified as well (**Figure 9**). Additionally, it was noted that if the reaction went on for too long, DMPP would react with the MPA-GM molecule as well (**Figure 10**).











Based upon troubleshooting different equivalencies of MPA compared to unreacted guanidine monomer and different reaction times, the ideal conditions were 2 equivalents of MPA with a minimum reaction time of 30 minutes.

The FT-T1M1 product was reacted with 2 equivalents of MPA to unreacted guanidine monomer and heated to 40°C for 60 minutes. The product was dried down to remove MeOH, and resolubilized in 1mL DCM. Next, an equivalent volume of 100 mM NaOH was used to extract the MPA-GM molecule. Once the solution settled after being shaken, it formed an emulsion

(**Figure 11[A]**). Brine and sodium bicarbonate were added to remove the emulsion, but the emulsion remained (**Figure 11[B]**).

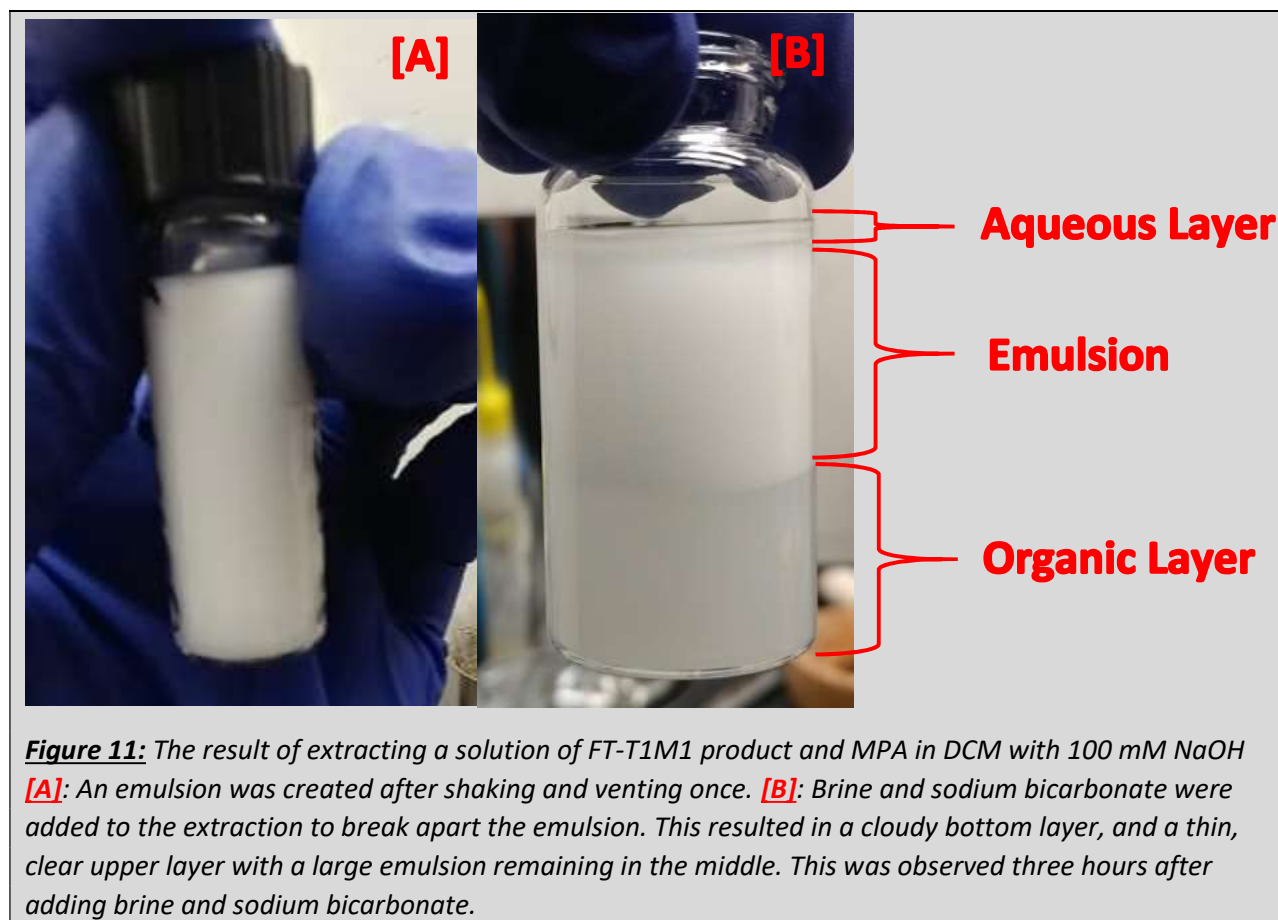


Figure 11: The result of extracting a solution of FT-T1M1 product and MPA in DCM with 100 mM NaOH **[A]**: An emulsion was created after shaking and venting once. **[B]**: Brine and sodium bicarbonate were added to the extraction to break apart the emulsion. This resulted in a cloudy bottom layer, and a thin, clear upper layer with a large emulsion remaining in the middle. This was observed three hours after adding brine and sodium bicarbonate.

MPA is well documented in literature as being a stabilizer for nanoparticles^[8], surfactants^[9], and colloids^[10]. Attempts to remove the emulsion have yielded modest results (**Figure 11[B]**).

Conclusion / Future Work

The extraction of excess PDT from the product after the thiol-ene reaction was a success. Even though it was documented that two washes of 100 mM NaOH removed a majority of the PDT, five washes were performed to ensure that all excess PDT was removed. Furthermore, TLC was successfully used to identify whether the product still contained PDT. It was a straightforward procedure that can be performed immediately after the extraction of a thiol-ene reaction, and can assist in qualitatively assessing the product after each extraction wash. There was notable time savings when using a liquid-liquid extraction method with TLC as compared to a traditionally lengthy FSPE. When PDT remained in the solution when the Michael addition was performed, the guanidine monomer would react with the excess PDT instead of the desired FT-T1 reagent – This would severely limit the growth of the oligomer, and additional amounts of guanidine monomer would need to be used.

The extraction of excess guanidine monomer from the product after the Michael addition needed further test work. LCMS was used to verify that the guanidine monomer would react with MPA, creating a molecule that could be extracted through an aqueous layer. Moreover, the desired product, FT-T1M1, was found in the solution with no remaining guanidine monomer. Also, at no point was a “capped” FT-T1M1 product with MPA found at any equivalency or at any time point. The only notable side product was DMPP reacting with the MPA-GM molecule.

Additional test work would need to be performed to see if the emulsion would be formed again following the same protocol. If the emulsion forms again, possible solutions include centrifuging the solution at a high enough speed to break apart the emulsion, use a less polar thiol molecule than MPA, gently shake the extraction, or try different solvents for the organic layer, such as diethyl ether or methanol.

The protocol for extraction after the Michael addition will need to be retested and resolved before continuing with the synthesis process of oligoTEAs. Questions remain as to how feasible the extraction will be once the oligomer is longer, and whether the growing amount of DMPA and DMPP in the solution will create any byproducts. Further advances in the extraction process may need to include more definitive ways of removing these catalysts as they could cause unforeseen reactions.

References

- [1] Piddock LJ. The crisis of no new antibiotics—what is the way forward? *Lancet Infect Dis.* 2012;12(3):249–253. <https://www.ncbi.nlm.nih.gov/pubmed/22101066>
- [2] The antibiotic alarm. *Nature.* 2013;495(7440):141. <https://www.ncbi.nlm.nih.gov/pubmed/23495392>
- [3] Centers for Disease Control and Prevention, Office of Infectious Disease Antibiotic resistance threats in the United States, 2013. Apr, 2013. Available at: <http://www.cdc.gov/drugresistance/threat-report-2013>. Accessed August 3, 2018.
- [4] Van't Hof, W., Veerman, E. C., Helmerhorst, E. J., and Amerongen, A. V. (2001) Antimicrobial peptides: properties and applicability. *Biol. Chem.* 382, 597– 619. <https://www.degruyter.com/view/j/bchm.2001.382.issue-4/bc.2001.072/bc.2001.072.xml>
- [5] Hancock, R. E. W. and Sahl, H.-G. (2006) Antimicrobial and host-defense peptides as new anti-infective therapeutic strategies. *Nat. Biotechnol.* 24, 1551– 1557. <https://www.nature.com/articles/nbt1267>
- [6] Matsugi, M.; Curran, D. P. (2004) Reverse Fluorous Solid-Phase Extraction: A New Technique for Rapid Separation of Fluorous Compounds. *Org. Lett.*, 6, 2717. <https://pubs.acs.org/doi/10.1021/ol049040o>
- [7] Porel, M. and Alabi, C. A. (2014) Sequence-Defined Polymers via Orthogonal Allyl Acrylamide Building Blocks. *J. Am. Chem. Soc.* 136, 13162– 13165. <https://pubs.acs.org/doi/10.1021/ja507262t>
- [8] H. Kaczmarek, M. Metzler, K. Wegrzynowska-Drzymalska. (2016) Effect of stabilizer type on the physicochemical properties of poly(acrylic acid)/silver nanocomposites for biomedical applications. *Polym. Bull.*, 73, pp. 2927-2945. <https://link.springer.com/article/10.1007%2Fs00289-016-1617-3>
- [9] Jiménez-Hernández, L & Estévez Hernández, Osvaldo & Hernández, Mayra & Diaz, Jesus & Farías- Sánchez, M & Reguera, E. (2015). 3-mercaptopropionic acid surface modification of Cu-doped ZnO nanoparticles: Their properties and peroxidase conjugation. *Colloids and Surfaces A: Physicochemical and Engineering Aspects.* 489. <https://www.sciencedirect.com/science/article/pii/S0927775715303332?via%3Dihub>
- [10] Marcos Marques da Silva Paula, Helton Jeremias de Souza, Carina Búrigo, Jamile Thön Langbehn, Alice Scarabelot Baesso, Luciano da Silva, Paulo Roberto Paes da Silva, Roberto Benavides, Gabriel Alonso-Núñez, Virginia Collins. (2017) Evaluation of the permeability of silver nanoparticles in polymer films of sulfonated polystyrene-co-acrylic acid. *Colloids and Surfaces A: Physicochemical and Engineering Aspects*, Volume 520, Pages 78-84. <http://www.sciencedirect.com/science/article/pii/S0927775717300961>

Acknowledgements

Thank you to Professor Alabi, Christine, Jake, Chris, Nana, the Alabi Lab group, and the Cornell Center for Materials Research for their guidance, support, and patience.

Effects of Oxidation Time and Temperature on Supercapacitor Performance of Spinel $\text{Ni}_{1.5}\text{Co}_{1.5}\text{O}_4$ Monodisperse Nanoparticles

Whitney Tso¹, Cindy Chen², Anuj Bhargava², and Richard Robinson²

¹Department of Materials Science and Engineering, University of Illinois Urbana-Champaign, Champaign, IL 61820

²Department of Materials Science and Engineering, Cornell University, Ithaca, NY 14853

Abstract: Recently, there has been a rising interest in the research of supercapacitors due to their rapid charge and discharge speed and their long discharge cycle life. Nanotechnology has been one of the ways to resolve the increase in demand for better electronics, such as using nanoparticles in a supercapacitor. Ni-Co nanoparticles are synthesized first, then coated on a copper electrode through EPD, then oxidized at various temperatures and durations in the furnace. The supercapacitor performance of the samples are determined by running CV and CD tests on a coin cells with a two-electrode system. The samples are characterized with ICP-MS and TEM to determine the particle shape and stoichiometry. It was observed that samples oxidized at a lower temperature and longer durations are able to retain the size and shape of nanoparticles, and has better supercapacitor performance.

Introduction

In recent years, there has been a growing interest in the research of supercapacitors. The idea is that a supercapacitor has the ability to store much higher energy density than a normal capacitor and has greater power density than a normal rechargeable battery. Other than the ability to charge and discharge at an amazing rate, it also has a much longer discharge cycle life. There are many applications and potential for supercapacitors in industry. Companies have started to incorporate supercapacitors in their hybrid or electric automobiles for its rapid charging and discharging capabilities.

A supercapacitor has a similar structure compared to a normal capacitor, but works in a very different manner. Normal capacitors are composed of two plates separated by a thick dielectric material that polarizes under an electric field. In a supercapacitor, there are two plates that are separated by a much smaller distance. The two plates are soaked in electrolyte and separated by a thin

separator made from an insulating material. The ions in the electrolyte move towards the plates when charging and away when discharging. Therefore, the capacitance of a supercapacitor is proportional to the effective surface area of the plates.

As the demand for better electronics increases, people started to turn to nanotechnology for answers. Nanoparticles are generally at the scale of 1-100 nm, which means they have a small volume but large surface area relatively. This characteristic of nanoparticles presents a lot of potential in supercapacitors.

Many researches have been done to analyze the supercapacitor performance of metal oxides, especially base transition metal oxides [1]. Study has also shown that binary metal oxides with spinel structure has better performance as it amalgamates the supercapacitor properties of two monometallic oxides, such as $\text{Co}_{3-x}\text{Mn}_x\text{O}_4$ that combines the properties of Co_3O_4 and MnO_2 [2]. NiO has shown to have better

electrochemical performance compared to MnO_2 , therefore the binary metal oxide $\text{Ni}_x\text{Co}_{3-x}\text{O}_4$ shows great potential in the application of supercapacitors [1]. In this report, we studied the spinel material, $\text{Ni}_{1.5}\text{Co}_{1.5}\text{O}_4$, as the performance was found to be the best at near equal ratio of the two metal cations [2].

Experimental Section

Synthesis of monodisperse Ni-Co nanoparticles

The synthesis method used is modified from a previous experiment [3]. 0.25g of nickel acetate tetrahydrate, 0.25g of cobalt acetate tetrahydrate, 0.64mL of 99.9% oleic acid, and 40mL of diphenylether (DPE) is placed in a 250mL three-neck flask with a glass stir bar. The flask is placed under vacuum first, and then heated to 200°C under nitrogen. 3.5mL of trioctylamine (TOA) and 0.45mL of trioctylphosphine (TOP) is then added into the flask. The temperature of the flask is then increased to 250°C.

In another three-neck flask, 2.12 g of 1,2-dodecanediol and 10mL of DPE is heated to 80°C for 15 minutes under vacuum. The solution is taken out and rapidly injected into the first flask. The solution is allowed 20 minutes to react and nucleate before it is quenched to room temperature in a water bath.

The solution is poured into tubes and centrifuged, causing the nanoparticles to sink to the bottom of the tubes. The liquid is then poured out and hexane is added to suspend the nanoparticles.

Electrophoretic deposition (EPD)

EPD is used to deposit a thin and even layer of Co-Ni nanoparticles on top of the copper plates. Two stainless steel plates are placed at

a small distance apart, parallel to each other. Those are connected to a voltage source at the positive and negative side respectively. A circular copper plate is weighed first, then stuck to the inner side of the positive steel plate.

0.5mL of the nanoparticles in solution is further diluted with 9.5mL of hexane and sonicated in a water bath for at least 2 minutes. The stainless steel plates are placed in the diluted solution. The DC voltage source is set to 600 V. Generally, the process is about 30 seconds to 5 minutes. The target active mass is around 0.1 mg.

The copper plates with metal nanoparticles coated are calcined in the furnace at various durations and temperatures. The heating rate is 10°C/min to ensure all nanoparticles are at the same temperature.

Sample Characterization

The cobalt-to-nickel ratio is analyzed using inductively coupled plasma mass spectrometry (ICP-MS) to ensure that we are synthesizing a material close to equal ratio of the metal cations. The shape and size of metal nanoparticles are analyzed using transmission electron microscopy (TEM). This technique is also used to characterize the metal oxide, such as the state of oxidation and shape of particles, after undergoing various oxidation parameters.

Electrochemical measurements

The electrochemical properties of the samples were studied by cyclic voltammetry (CV) and cyclic charge discharge (CD) on a two-electrode system with the sample as the anode, a carbon cloth as the cathode, and lithium bis(trifluoromethanesulfonyl)imide (LiTFSI) as the electrolyte. The scan rate for CV tests are 50 mV/s, and the scan rate for

CD tests are 0.1 A/g. The energy density (E), power density (P), and specific capacitance (C) were calculated using Eqn. 1, 2, and 3 [2].

$$E = \int \frac{VI}{m} dt \quad [\text{Eqn. 1}]$$

$$P = \frac{E}{\Delta t} \quad [\text{Eqn. 2}]$$

$$C = \frac{I \Delta t}{m \Delta V} \quad [\text{Eqn. 3}]$$

V is the voltage, I is the discharge current density, m is the active mass of the material on the copper electrode, and Δt is the discharge time.

Results and Discussion

Before oxidizing any samples, the particles are characterized with ICP-MS and TEM. We analyzed the Ni to Co ratio to be 1.48 to 1.52. Fig. 1 shows the Co-Ni particles before oxidation. The average diameter measured is $20.8 \text{ nm} \pm 1.8 \text{ nm}$. The relatively low dispersity is another evidence that the synthesized particles are good for testing.

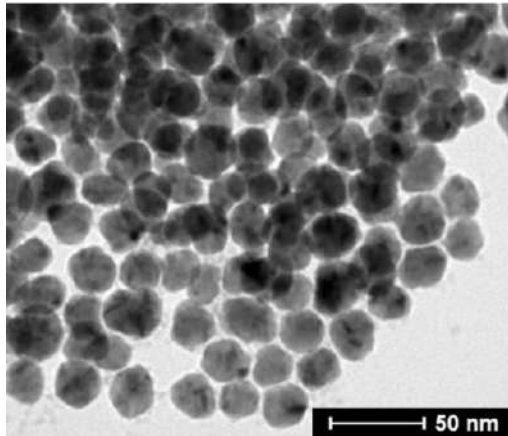
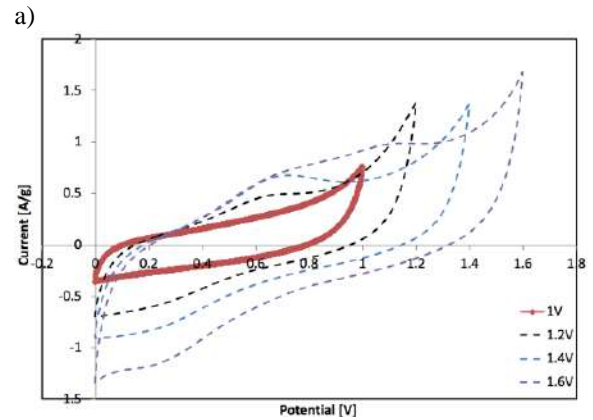


Fig. 1 TEM images of Co-Ni nanoparticles.

In order to conduct CD tests on the coin cells, the voltage range needs to be optimized. As our goal is to analyze the supercapacitor performance of the samples, we want to

maximize the voltage range, but without having the cell go through irreversible redox reactions. This can be determined by conducting CV tests on the samples. Fig. 2 shows the CV tests conducted on two different coin cells. An irreversible redox reaction can be observed through a peak in the CV curve. As we increase or decrease the voltage limits, a peak at around 0.6 V would appear. This is indicative that we have pass the optimal voltage range. It is determined that the voltage range for further CD tests are from -0.4 V to 1 V. Furthermore, the rectangular CV curve shape that can be seen from Fig. 2 is another sign that the sample exhibits supercapacitor characteristics. The curves are dependent on the change in voltage and capacitance. Since we are keeping the rate constant, the larger area under the curve represents the material having a better capacitance.



b)

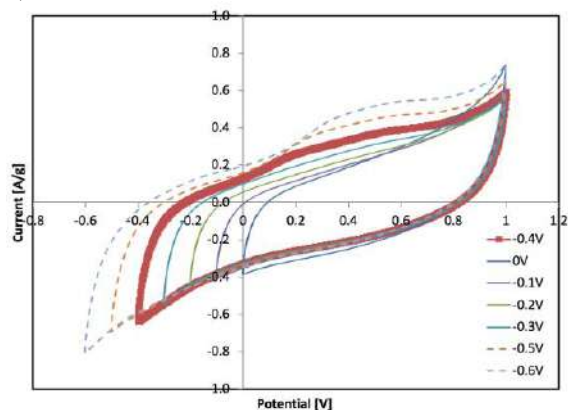


Fig. 2 CV curves of coin cells to optimize voltage range. The red curve shows the optimal voltage limit. a) testing the upper voltage limit by holding the lower limit at 0 V and changing the upper limit. b) testing the lower voltage limit by holding the upper limit at 1 V.

Fig. 3 shows the different oxidation parameters we have tested. The samples are imaged under TEM to observe the shape of the oxidized particles. Based on other studies, it has been observed that we can oxidize the metal particles into spinel phase at around 200 – 300 °C. We decided to set the temperature at 250 °C as a starting point, and vary the oxidation time.

Sample	Time [hrs]	Temperature [°C]
1	2	250
2	4	250
3	8	250
4	12	225

Fig. 3 Oxidation parameters of various samples and their respective labelling.

From the TEM image of Sample 1 (Fig. 4a), we observe that the metal oxide particles are nanosized, but has a core-shell structure with a center that is half filled. This is indicative that this sample is partially oxidized. The darker region in the core is the unoxidized Ni-Co, the lighter region in the core is a hole where the metal particles moved outwards to form the metal oxide shell.

The TEM image of Sample 2 (Fig. 4b) also show signs of partial oxidation, but there is an observable increase in the number of particles that are fully oxidized. Then we decided to increase the oxidation time more in order to fully oxidize all the particles.

However, based on the TEM image of Sample 3 (Fig. 4c), we can observe signs of sintering. The nanoparticles have started to fuse together to form one big particle. Even though at this oxidation parameter, we can obtain a more complete spinel material, it has lost the characteristics of a nanoparticle that could potentially make it a better supercapacitor. We then tested another sample at a lower temperature and a longer duration.

From the TEM image of Sample 4 (Fig. 4d), we can see that, while it has more partially oxidized particles compared to Sample 3, it has a lower amount of sintering. This sample has better particle structure as it retains more of the nanoparticle characteristics, allowing the sample to have greater surface area.

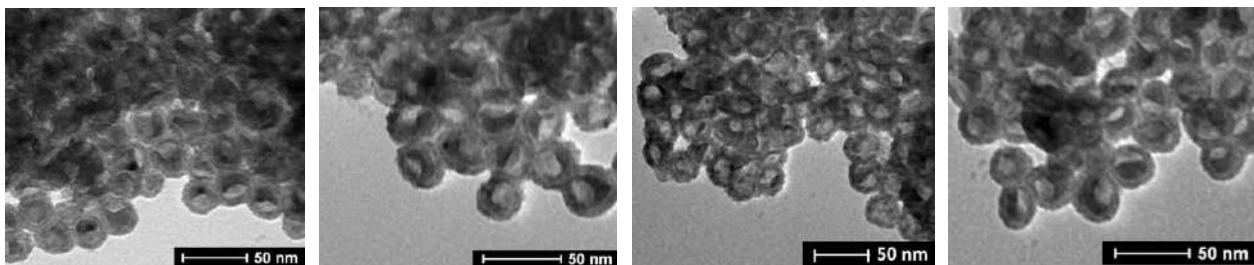


Fig. 4 TEM images of oxidized Co-Ni nanoparticles. From left to right: Sample 1 (oxidized at 250 °C for 2 hours), Sample 2 (oxidized at 250 °C for 4 hours), Sample 3 (oxidized at 250 °C for 8 hours), and Sample 4 (oxidized at 225 °C for 12 hours).

Fig. S1 in supplementary information shows the CV data collected from the coin cells assembled with the various samples as the cathode material. By increasing the oxidation time, it can be observed that the cells better resemble the rectangular shape, which is an indication that the material performs like a supercapacitor. Sample 4 (Fig. 5) has the largest area under the CV curve, which is a sign that it has the best supercapacitor performance compared to other samples.

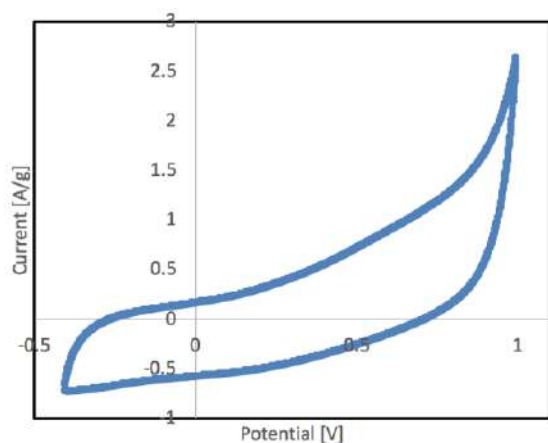


Fig. 5 CV curve of Sample 4.

In order to quantitatively calculate the supercapacitor performance, we conducted the CD test on Sample 4 (Fig. 6). Fig. S2 plots the data of a CD test of Sample 2 that has worse supercapacitor performance in comparison. Using this data, we are able to calculate the energy density, power density, and specific capacitance using Eqn 1, 2, and 3. We only consider the discharge portion of the CD curve for calculation. Fig. 7 tabulates the average energy density, power density, and specific capacitance of all four samples. Based on the calculated values, we can see that Sample 4 has the best supercapacitor performance compared to the other samples.

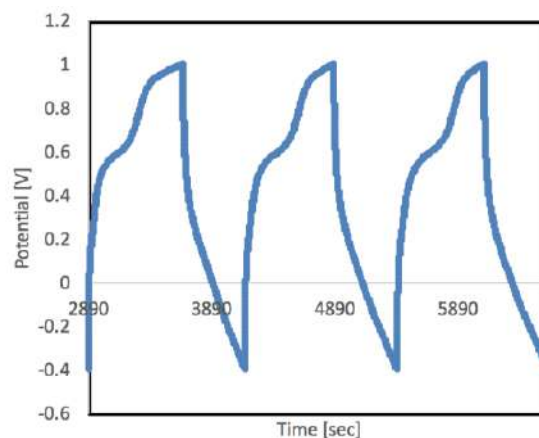


Fig. 6 CD curve of Sample 4 with scan rate of 0.1A/g from -0.4 V to 1 V. This is a cropped plot of cycle 2 to 4 only.

Sample	Energy Density [W h/kg]	Power Density [W/kg]	Specific Capacitance [F/g]
1	3.88e-5	0.139	1.05e-3
2	6.99e-6	0.0251	2.15e-6
3	9.25e-6	0.0333	1.58e-6
4	0.142	1.00	37.9

Fig. 7 Average calculated energy density, power density, and specific capacitance of all the samples.

Conclusion

In summary, oxidizing monodisperse Co-Ni nanoparticles at lower temperatures and longer durations yield better supercapacitor performances. This could be contributed to the particles being fully oxidized without sintering. However, the supercapacitor performance is still lower than what is expected. Therefore, while this material shows promising results, further studies will be conducted on refining the oxidation parameters and decrease particle size to fabricate better supercapacitor material.

Acknowledgements

I would like to thank the whole Robinson research group, especially Dr. Richard Robinson and Anuj Bhargava, for their support on this project. I would also like to thank the CCMR REU program funded by NSF for giving me this opportunity to participate in the summer program.

References

[1] Wu, Zhibin et al. "Transition Metal Oxides As Supercapacitor Materials." *Nanomaterials in Advanced Batteries and Supercapacitors* (2016): 317-344. Web. 31 July 2018.

[2] Perera, Sanjaya D. et al. "Enhanced Supercapacitor Performance For Equal Co-Mn Stoichiometry In Colloidal Co₃-XmnxO₄ Nanoparticles, In Additive-Free Electrodes." *Chemistry of Materials* 27.23 (2015): 7861-7873. Web.

[3] Murray, C.B. et al. "Monodisperse 3D Transition-Metal (Co,Ni,Fe) Nanoparticles And Their Assembly Into Nanoparticle Superlattices." *MRS Bulletin* 26.12 (2001): 985-991. Web.

Supplementary Information

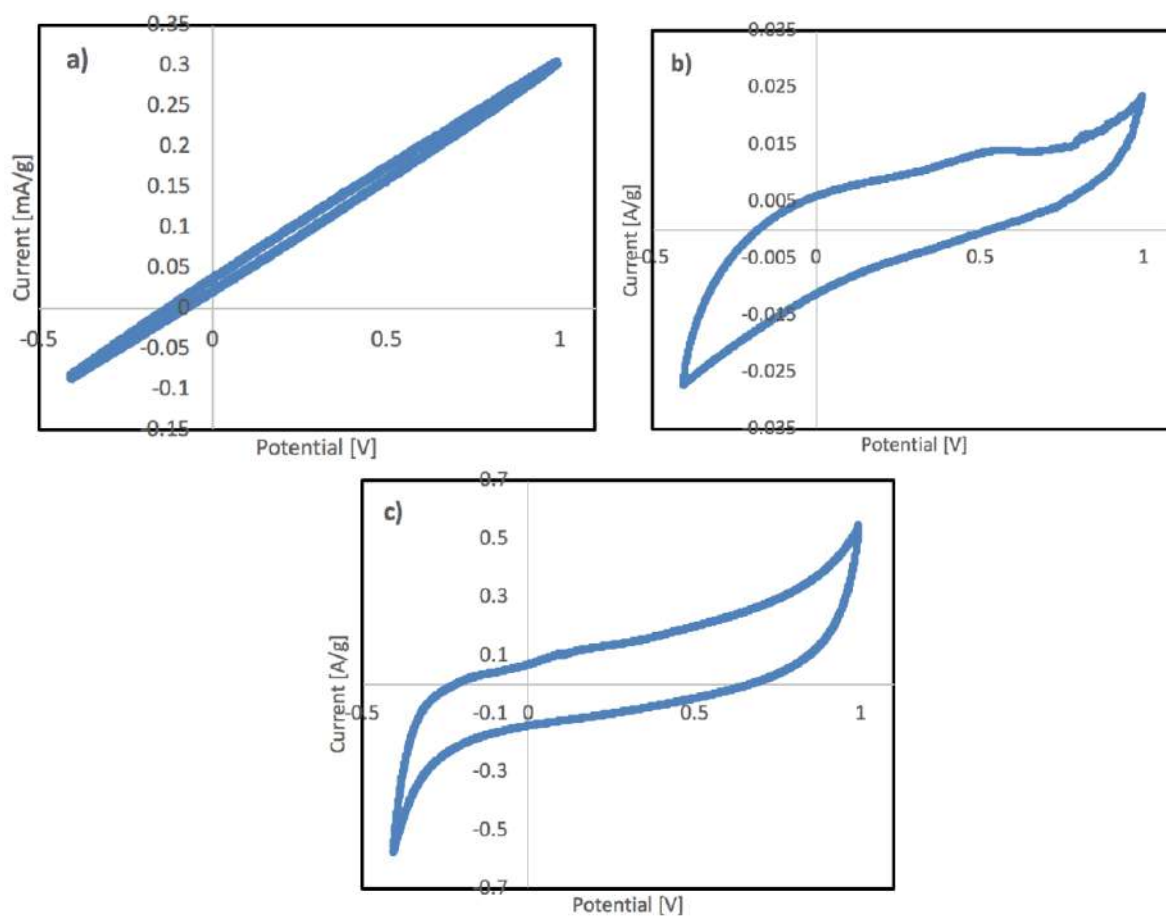


Fig. S1 CV curves of coin cells with the cathode coated with a) Sample 1, 250 °C for 2 hours, b) Sample 2, 250 °C for 4 hours, and c) Sample 3, 250 °C for 8 hours.

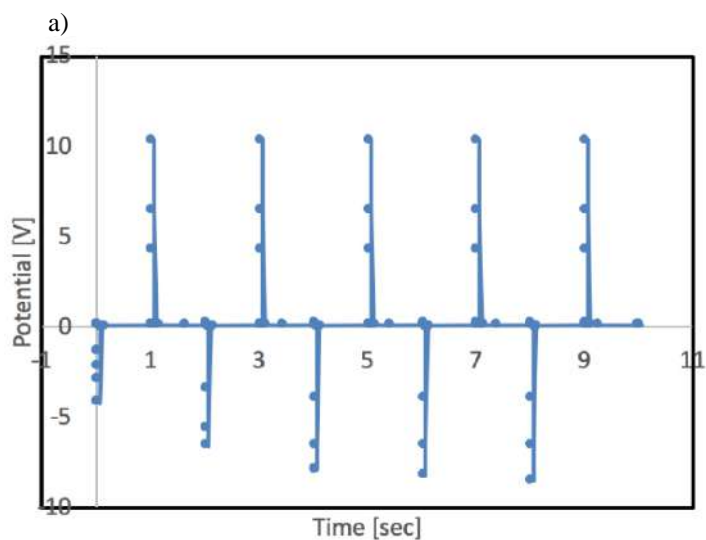


Fig. S2 a) CD plot of Sample 2 with scan rate of 0.1 A/g from -0.4 V to 1 V.

Lactase CLEAs for the Valorization of Lactose Waste Streams

Deidra Ward¹, Julie Goddard²

¹Department of Chemical and Biomolecular Engineering, Clemson University, Clemson, SC 29631

²Department of Food Science, Cornell University, Ithaca, NY 14853

Abstract

The formation of cross-linked enzyme aggregates [CLEAs] are a well-studied method of immobilizing enzymes. Immobilizing enzymes have many industrially relevant applications, particularly in the context of dairy processing. One of the byproducts during Greek yogurt production is acid whey. Acid whey is of particular interest since it has been shown by researchers at Corning, Inc. that treating the whey with immobilized lactase can convert this waste product into sweeteners. This treatment would add more value to this waste stream. In this study, we investigated lactase CLEAs for its potential use in the valorization of acid whey waste streams.

Introduction

The dairy processing industry is a very lucrative and well-established industry. However, it is currently plagued with waste streams that do not have much current value. For example, during the production of Greek yogurt, acid whey is produced. Acid whey currently has no industrial use so it is mainly discarded. This presents both an environmental and economic problem.

However, researchers at Corning, Inc.¹ have discovered a method of treating acid whey with immobilized lactase in order to convert it into a sweetener. This process would add value to this waste stream, allowing the economic and environmental impact to be decreased. The method that these researchers discovered involves immobilizing the lactase onto a porous, inorganic carrier to treat the whey. This process, while successful, presents some issues since it has been shown that immobilization methods that involve

binding to a carrier results in a decrease in catalytic activity due to the introduction of a non-catalytic mass.

In order to overcome this limitation, we want to investigate cross-linked enzyme aggregates [CLEAs] for their potential use in the valorization of waste streams. CLEAs are a carrier-free method of immobilizing enzymes that combines both enzyme purification and immobilization into a single step². This method of immobilizing enzymes is of industrial relevance due to its lower cost, recyclability, quick time-to-market, and its optimizable nature³. It has been shown that CLEAs have increased stability to changes in temperature and pH compared to the free enzyme⁴. This is of particular interest since in industrial settings, many streams are at extreme temperature and pH values.

Thus, we are developing a method of producing lactase CLEAs that can be used for the treatment of acid whey streams.

This work can then be expanded to other enzymes, such as glucose isomerase, to valorize waste streams.

Materials and Methods

Lactase Purification

Before being able to immobilize the enzyme, the lactase must be purified. The lactase was prepared in potassium phosphate buffer (0.1M, pH 6.8) and filtered through a 0.22µm PES syringe filter before centrifugal filtration was performed using the Amicon Ultra – 0.5 Centrifugal Filter Devices (MWCO 10k). Centrifugal filtration was performed for 15 minutes at 14000*g and then flushed with 135µL of the potassium phosphate buffer twice. The resulting purified free enzyme lactase solution was then tested for its protein content or stored at 4°C.

CLEA formation

Protein content determination of purified lactase. The protein content of the purified lactase solution was determined using a microplate BCA protein assay. Absorbance measurements were taken at 562nm and compared against a standard curve created from known concentrations of BSA. We assumed that the concentration of BSA was equal to that of the lactase.

Production of lactase CLEAs. After determining the protein content of the purified lactase, the free lactase solution was diluted to a concentration of 7mg lactase/mL potassium phosphate buffer. After diluting, the 320µL of the lactase was separated into 2mL centrifugal tubes and mixed with 1280µL of acetone using a rotator set to 40rpm for 30 minutes. After

mixing, 28.8µL of glutaraldehyde (50%) was added to each lactase-acetone mixture. This mixture was then vortexed for 15 seconds before sitting at room temperature for 22 hours in order to allow cross-linking to occur. After cross-linking, samples were centrifuged for 1 minute at 10 000*g. The supernatant that resulted from centrifugation was decanted. This resulting CLEA was washed thrice by adding 1 mL of potassium phosphate buffer (0.1M, pH 6.8) and centrifuging for 1 minute at 10 000*g. CLEAs were then stored in 640µL of the potassium phosphate buffer (0.1M, pH 6.8) at 4°C or characterized using the following methods. CLEAs with varying amounts of glutaraldehyde were made by adding 28.8µL of glutaraldehyde to 640µL of the diluted lactase or adding 14.4µL of glutaraldehyde to 640µL of the diluted lactase.

CLEA characterization

Scanning Electron Microscopy [SEM]. In order to observe the surface morphology of the CLEAs, SEM was performed. Samples were prepared by placing the CLEA onto aluminum foil and allowing the sample to air dry in a fume hood overnight. The air-dried samples were then sputter coated via gas flow sputtering before analyzing their surface structure.

Protein content determination of CLEAs. The protein content of the CLEAs were determined using a microplate BCA protein assay. To prepare the samples, CLEAs were vortexed until they began to break apart in the phosphate buffer. In order to increase this dispersion, CLEAs were physically separated using a syringe tip. Absorbance measurements were taken at 562nm and compared against a standard curve created

from known concentrations of BSA. We assumed that the concentration of the BSA was equal to that of the lactase CLEA.

Results and Discussion

BCA protein assays for the CLEAs resulted in inconsistent concentration values. We would have expected the concentrations determined based on the BSA standard to all have been consistent. However, we found that concentrations varied greatly within samples, as well as across samples. Figure 1 highlights the inconsistent nature of these samples.

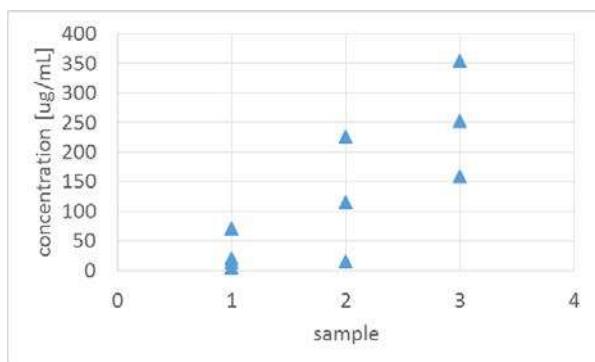


Figure 1. BCA protein analysis results for CLEAs

Because of the inconsistencies in the BCA protein assay, we began to investigate reasons for this discrepancy. Figure 2 showcases the standard curves that were produced from the BCA protein assays. These curves are quite consistent, leading us to determine that protein concentrations calculated via this method should be consistent.

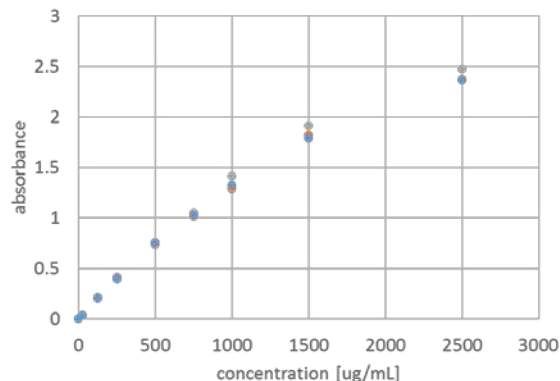


Figure 2. BCA protein assay standard curves used to determine concentrations of unknown samples

One possible reason for this discrepancy could be in the preparation of samples for the BCA protein assay. As described earlier, samples were prepared by vortexing the CLEA in the potassium phosphate buffer and trying to get it to disperse in the buffer by breaking it apart with a syringe tip. Seeing as this is a very crude way of trying to disperse the CLEA, it is highly probable that there was no uniformity across samples. Perhaps another method for dispersion, such as sonication, should be investigated further in the future.

Another possible reason for the inconsistent BCA protein assays could be the CLEA, itself. When cross-linking an enzyme, it is important to prevent excessive cross-linking. When there is excessive cross-linking, the structure of the enzyme changes and the activity is decreased. In order to determine if there was excessive cross-linking, we examined the SEM images of the CLEAs and found that the CLEAs had a smooth surface structure. This led us to hypothesize that the CLEAs were excessively cross-linked and if we decrease the amount of glutaraldehyde added to each sample, we can decrease the cross-linking and have CLEAs that are more easily

dispersed in potassium phosphate buffer. This would then allow us to test for its protein content more consistently.

When we investigated the effect of decreasing glutaraldehyde content on the surface roughness of the CLEAs, we found that as the amount of glutaraldehyde decreased, the roughness increased. We associated this increase in roughness with a decrease in cross-linking. This matched our hypothesis of less glutaraldehyde resulting in less cross-linking. We will investigate whether this results in more consistent characterization in the future.

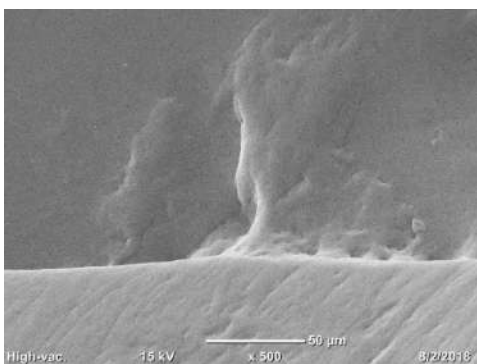


Figure 3. SEM image of CLEA with x amount of glutaraldehyde

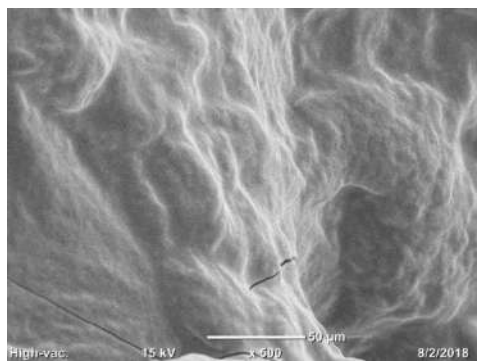


Figure 4. SEM image of CLEA with 0.5x amount of glutaraldehyde

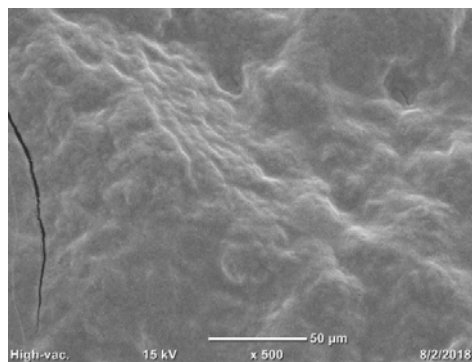


Figure 5. SEM image of CLEA with 0.25x amount of glutaraldehyde

Conclusions

The initial method that was used to produce lactase CLEAs resulted in CLEAs that were excessively cross-linked. This would have a negative impact on the activity of these enzymes, rendering them useless for our industrial application. However, by decreasing the amount of glutaraldehyde present during the cross-linking process, the degree of cross-linking can be reduced. This can then result in CLEAs that can be tested consistently for their protein content and catalytic activity.

In the future, we hope to develop a means of producing these CLEAs that result in an aggregate that retains enough activity to be used in our industrial application, along with being stable enough to be used at various temperatures and pH values.

Acknowledgements

Thank you to Dr. Julie Goddard and the Goddard Lab Group for your mentorship and support. Thank you to the CCMR REU program funded by the NSF for this opportunity.

References

1. Weetall, H., Yaverbaum, S.; (1973); *Patent No. 3,852,496*; Corning, NY; United States Patent Office
2. Sheldon, R. A.; *Biochemical Society Transactions* **2007**, 35 (06), 1583-1587
3. Sheldon, R. A.; *Organic Process Research & Development* **2011**, 15, 213-223
4. Li, L., Li, G., Coa, L., Ren, G., Kong, W., Wang, S., Guo, G., Liu, Y.; *Journal of Agricultural and Food Chemistry* **2015**, 63, 894-901